Optimization of Complex Thermal-Fluid Processes

by

Joon Young Lee

A Dissertation Presented in Partial Fulfillment
of the Requirements for the Degree
Doctor of Philosophy

Approved April 2015 by the
Graduate Supervisory Committee:

Taewoo Lee, Chair
Huei-Ping Huang
Juan Lopez
Patrick Phelan
Kangping Chen

ARIZONA STATE UNIVERSITY

August 2015

ABSTRACT

First, in a large-scale structure, a 3-D CFD model was built to simulate flow and temperature distributions. The flow patterns and temperature distributions are characterized and validated through spot measurements. The detailed understanding of them then allows for optimization of the HVAC configuration because identification of the problematic flow patterns and temperature mis-distributions leads to some corrective measures. Second, an appropriate form of the viscous dissipation term in the integral form of the conservation equation was considered, and the effects of momentum terms on the computed drop size in pressure-atomized sprays were examined. The Sauter mean diameter (SMD) calculated in this manner agrees well with experimental data of the drop velocities and sizes. Using the suggested equation with the revised treatment of liquid momentum setup, injection parameters can be directly input to the system of equations. Thus, this approach is capable of incorporating the effects of injection parameters for further considerations of the drop and velocity distributions under a wide range of spray geometry and injection conditions. Lastly, groundwater level estimation was investigated using compressed sensing (CS). To satisfy a general property of CS, a random measurement matrix was used, the groundwater network was constructed, and finally the l-1 optimization was run. Through several validation tests, correct estimation of groundwater level by CS was shown. Using this setup, decreasing trends in groundwater level in the southwestern US was shown. The suggested method is effective in that the total measurements of registered wells can be reduced down by approximately 42 %, sparse data can be visualized and a possible approach for groundwater management during extreme weather changes, e.g. in California, was demonstrated.

DEDICATION

To my parents, Youn Hyun Lee and Myung Ja Lee,

my wife, Joo Young Kim,

my children, Sarah and Abigail,

my family members, Eun-Ha, Jung-Ha and Young-Ha,

and God, my stronghold in the day of trouble. He knows those who trust in Him.

ACKNOWLEDGMENTS

TABLE OF CONTENTS

LIST OF TABLES

LIST OF FIGURES

x

**CHAPTER 1**

**INTRODUCTION**

Large scale buildings consume an enormous amount of energy to maintain its critical temperature. Heating, Ventilation, and Air Conditioning (HVAC) is main factor in energy consumption. Energy saving directly or indirectly comes from efficient use of HVAC if the main goal is to maintain its pre-set temperature values in different seasons. Saving can be maximized when the consumption of HVAC system is correctly analyzed with respect to temperature distribution and airflow distribution. Corrective measures can be implemented according to results from system analysis. 3 dimensional (3-D) CFD model was built and simulated with commercial CFD software called ANSYS Fluent. The model validation was done by comparison of spot measurements of temperature with temperature distribution of CFD results. Various combinatorial cases were run and compared in different boundary conditions for optimal flow and temperature distribution. Based on the fundamental understanding of fluid dynamics, the implementation of the suggested corrective measures was guided.

Pressure atomized spray droplet estimation is very useful for combustion engineers and rocket scientists. This estimation starts from the derivation of the integral form of the conservation equations (Lee and Robinson 2011). The important step is to relate the input variables directly to the output variables of the integral form without mandatorily resolving the complex details of the atomization process. The closed form, with the help of an efficient algorithm by the assumption of lognormal distribution and its algebraic simplification of moment generating functions, results in various types of successful estimations on the Sauter mean diameter (SMD), the spray droplet size distribution and

1

the phase velocities. The closed form's fundamentally sound basis (Lee and Robinson 2011) is utilized with the appropriate form of the viscous dissipation as well as the momentum treatments (Rothe and Block 1977). To compute the drop size, the revised treatment of liquid momentum enables stable calculations for a wide range of density ratios and injection parameters such as the spray cone angle and the atomization length are directly related to the system of equations. The calculated SMD agrees well with experimental data including the measurements of both drop velocities and sizes. This method can incorporate the effects of injection parameters and can be further used for a wide range of spray geometry and injection conditions.

Groundwater level estimation was investigated using compressed sensing (CS). To satisfy a general property of CS, a random measurement matrix was used. Relying on the US Geological Survey and the State Department of Water Resources for important data, the groundwater network was constructed. The mathematical formulation is shown, l1-optimization is formulated for the proposed method, and finally the optimization algorithm was run. Through several validation tests, correct estimation of groundwater level by CS was shown. Using this setup, decreasing trends in groundwater level in the southwestern US was shown. The suggested method is effective in that the total measurements of registered wells can be reduced down by approximately 42 %, sparse discrete data such as groundwater measurements in wide areas can be visualized and a possible approach for groundwater management during extreme weather changes, for example, agricultural areas such as Fresno in California, was demonstrated.

Large scale building energy simulation and optimization is in Chapter 2. Spray drop size estimation is described in Chapter 3. Estimation of groundwater level is explained in

Chapter 4. In Chapter 5, and trend in the southwestern US is investigated. Finally, in

Chapter 6, conclusions are drawn and future research topics are provided.

**CHAPTER 2**

**COMPUTATIONAL SIMULATION AND OPTIMIZATION IN A BUILDING**

### 1. Introduction

Energy conservation on the consumption side is as important as energy generation development for reducing carbon dioxide emissions. One third of the energy produced in the United States is consumed in residential and commercial buildings with most of that going to Heating Ventilating and Air Conditioning (HVAC) (United States Global Change Research Program 2009). Nearly all of this energy consumption is in electrical power. Due to a number of reasons, such as age and degradation, off-design operations, and poor insulation, HVAC operations in many instances are less than optimal. In some large-scale buildings, the internal electrical energy use can add up to a significant amount, frequently occupying a large fraction of the operational cost.

For the Coronado Generating Station (located in St. Johns, Arizona, USA) under consideration in this study, the internal electrical energy use is 11% out of the 435MW gross generation capacity. During operational planning, optimization of the HVAC is often overlooked, adding to the overall system inefficiency. In this work, we use a full three-dimensional model of the power plant building by reproducing its internal and external geometries, in order to computationally simulate the flow and temperature distributions under a wide range of ambient and HVAC operating conditions. The detailed understanding of the flow patterns and temperature distributions then allows for optimization of the HVAC configurations (vent location, flow direction and vent airflow rates and temperatures).

In modern design and management of buildings, analytical methods for identifying the details of the fluid motion and heat transfer are frequently used to minimize building energy consumption. Space discretization method, i.e. dividing the building interior into major representative zones, has been in use for quite some time, and software with considerable details of the zone geometry and HVAC units are commercially available (Clarke 2001). Recently, computational fluid dynamics (CFD) models have been used in many studies (Gan 1995; Chami and Zoughaib 2010; Lin and Zmeureaunu 2008; Gosselin and Chen 2008; Kuznik et al. 2006; Cheng and Hung 2005; Sinha et al. 2000; Ng et al. 2008), as they can provide much more insight into the flow patterns and therefore can be used to identify the causes of inefficiencies and remedies thereof. The level of sophistication in CFD analyses has grown markedly with available numerical methods and commercial CFD software, ranging from an early study of relatively simple geometries by Gan (1995) to a detailed study including natural convection effects (Chami and Zoughaib 2010). The latter CFD work also involved experimental validation using particle image velocimetry (Chami and Zoughaib 2010). In recent years, additional effects such as internal heat sources, buoyancy effects and other optimization devices have been investigated using CFD methods (Lin and Zmeureaunu 2008; Gosselin and Chen 2008; Kuznik et al. 2006; Cheng and Hung 2005; Sinha et al. 2000; Ng et al. 2008; Ren and Stewart 2003).

In this study, flow patterns and temperature distributions in a large building structure (a power plant building), measuring 80 m in width, 120 m in length and 60 m in height, are computationally simulated in some details. In addition to the relatively large dimensions, some of the interior structures, such as boilers, turbines and operational

5

equipment along with hard partitions and compartments, present unique challenges for HVAC optimization, as these interior components generate heat, impede or affect the flow patterns. For the boiler housed in the building, the heat gain is quite substantial, raising the temperature in the vicinity but also providing excess heat for possible use elsewhere. The CFD method applied for a full three-dimensional geometrical model of this building structure then allows identification of the problematic flow patterns and temperature mis-distributions. This in turn leads to some corrective measures, or optimization of the temperature distributions. As in all buildings, optimization of the HVAC can lead to a substantial reduction in the total electrical cost for maintaining target interior environments. In spite of the complexities, the interior building flow motion and temperature distributions are still subject to the basic laws of fluid mechanics and heat transfer, and utilization of these principles can lead to systematic improvements in the building HVAC performance. By identifying regions where these basic knowledge and principles can be applied, with the detailed knowledge of the flow and temperature provided by the CFD analyses, we can arrive at much improved temperature distributions through modifications that are often relatively simple and cost-effective to implement.

## 2. Computational Methods

The CFD simulation method is applied to a large-structure building, housing the boilers and turbines in a power generating station (Coronado Generating Station operated by the Salt River Project in St. Johns, Arizona, USA). Figs.2.1(a) and (b) shows the geometry and layout of the building, which has a large interior to house the boilers (two domed cylinders lined up along the z-axis), along with internal structures for equipment

and several hard floors. The two outer towers in Fig. 2.1(a) are the coal silos and do not emit heat. There are three rows of inlet vents along the z-axis at x=0, that can either supply outside air under warm weather or heated air under cold weather conditions. Two rows of exhaust vents are found on the ceilings above the turbines and the boiler section. As shown in Fig 2.1(b), there are three levels of floors on the boiler section, and a hard floor called the "turbine deck" separates the turbine and the section below that houses water circulation and other heavy equipment. This hard floor is not shown in Fig. 2.1(a), to allow visualization of the components behind this hard floor. Since it was not feasible to create geometrical representation of all the heavy equipment below the turbine deck, they were modeled as pressure losses, $\Delta P_1$, and $\Delta P_2$, impeding the vent flow, while hard floors could be directly inserted in the domain, as shown in Fig. 2.1 (b). Flow obstacles will impede the flow, and for complex shapes one way to model this flow impedance is through pressure losses terms. Since the flow obstacles were distributed in space, we opted to use two pressure losses. Using initial estimates of the pressure loss terms, based on the equipment height and density, final $\Delta P_1$, and $\Delta P_2$ were found after calibrating with the measured temperatures in that section. Since the boiler and turbine heat fluxes affected this section temperature little, calibration could proceed independent of the heat flux calibrations. Three temperatures are specified for the ambient, the bottom floor and the inlet vent air. The difference between the wall and the ambient temperature then specifies the heat loss or gain through all of the walls, at heat transfer coefficient, $h$. This heat coefficient, $h$, is first estimated based on average outside wind speed, and then optimized using the measured temperatures. For calibration purposes, two sets of temperature measurements were made, one at an ambient temperature of 6.7 ℃ and

another at 18.3 ºC. The measurements were done with a hand-held temperature sensor unit using a sheathed thermocouple, with a detachable sensor head. The sensor required approximately 1 minute to stabilize, and 2-3 minutes of wait times were used prior to taking the readings.

In spite of the complexity in the geometry and large scales involved, the internal flow and temperature distributions are amenable to fluid dynamics analysis through CFD methods. Here, we have constructed a three-dimensional model along with the boundary conditions, as shown in Figs. 2.1 (a) and (b), and imported this model into a CFD analysis package called FLUENT for simulating the flow and temperatures. FLUENT (2006) runs highly optimized finite-different algorithms to solve the fundamental conservation equations of mass, momentum and energy, based on a geometrical mesh laid on the input geometry and boundary conditions. Conservation equations of mass, momentum give flow velocities, which are coupled with the air density and temperature with the conservation equation for energy (Clarke 2001). Outside air temperature is used as the boundary condition between the building walls and the outside, where a convection heat transfer condition exists and is modeled according to the Newton's law of cooling, $Q_{wall} = hA(T_{wall} - T_{out})$. The effective heat transfer coefficient (h) for the wall heat loss typically was found to be 30 W/(K·m²). $T_{out}$ is the outside ambient temperature, while $T_{wall}$ is the temperature achieved at a given point due to internal circulations and heat transfer. Therefore, the effective heat transfer coefficient represents the effects of both the wall heat conduction, internal and external heat convection at that physical location. The vent air flow rate and temperature can also easily be adjusted, according to the HVAC operational settings, while the exhaust vent flow rates are set equal to the

8

incoming vent airflow rates so that a steady-state condition is maintained. Boilers and turbines emit heat due to high-temperature conditions that exist within these units, particularly for the boilers. The heat output of these units (boiler heat flux=100 W/m$^2$, turbine heat flux=5W/m$^2$) is also input into the CFD modeling, after calibration with measured temperatures. Boiler generates heat through combustion with coal and air, and the maximum temperature achieved is close to 2000 K, while the turbine runs steam which is rapidly expanding and cooling. The turbines are sealed for high-pressure operations, which also act to insulate heat losses. Since only the temperature measurements were available, the simulations were run at varying heat fluxes, until the best match with the measured temperatures were achieved then these heat fluxes were used as fixed boundary conditions at these surfaces. As noted above, the equipment beneath the turbine deck are lumped as two pressure drops impeding the vent flow; however, other major internal structures are directly modeled as shown in Figs 2.1 (a) and (b).

For the vent flow rates and dimensions, the flow has a large Reynolds number, and the flow is therefore turbulent. The vent flow speed is 1.64 m/s and the rectangular vents have a hydraulic diameter of 3 m, resulting in a Reynolds number of $6.6 \times 10^6$. The turbulence in the flow is handled by the so-called RNG κ-ε model in the simulations, which is similar to the standard κ-ε model. In the RNG κ-ε model, the low-Reynolds number effects at the walls are accounted for, so that wall functions are no longer needed (FLUENT 2006). The turbulence input data and agreements with the measured temperatures were easiest to achieve with the RNG κ-ε model. The number of operating vents and also the vent flow temperatures have been varied in the simulations. Also, for

optimization studies, additional vents have been created to find improved circulation and temperature distributions. In addition, all other variables such as the boiler heat output, outside temperature, the number and locations of exhaust vents can also be varied, making this kind of CFD model ideal for optimizing the flow and temperature distributions at minimum HVAC electrical energy use. The total number of nodes created for the computational model is 812,670 in adaptive tetrahedral grids, which requires approximately 50 hours of CPU time to complete a simulation on a PC with dual-core Intel processor running at 2.7GHz. Both steady-state and unsteady flows can be simulated, although in this study we are mostly interested in the steady-state flow and temperature distributions.
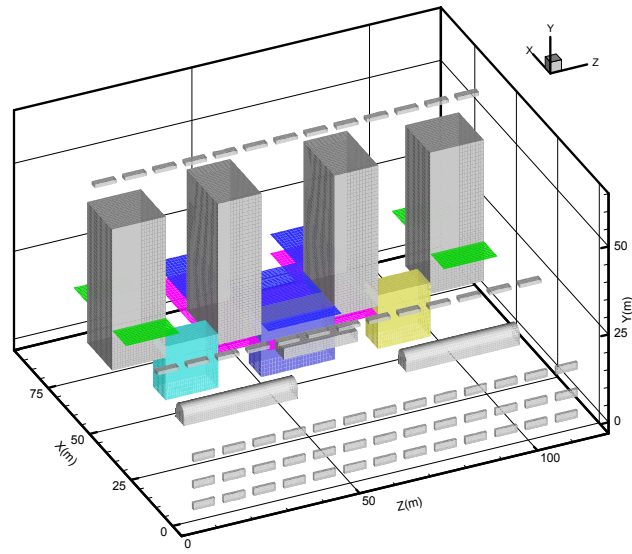
(a)
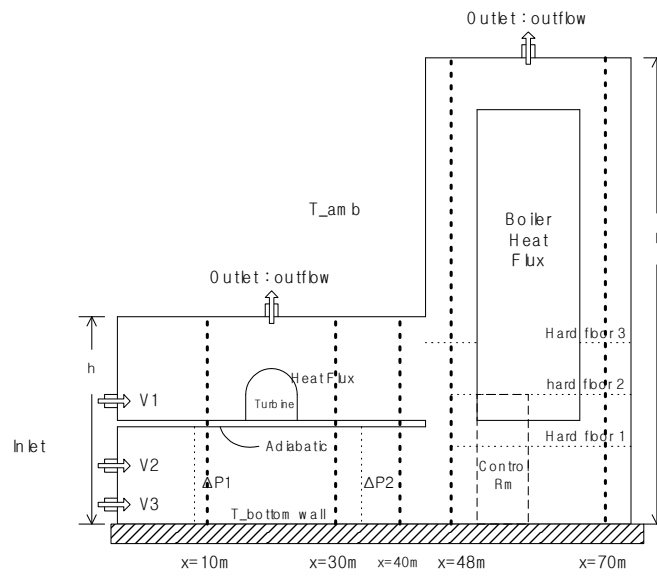


(b)

Fig. 2.1 (a) A perspective view of the building components and geometry; (b) a schematic of the basic configuration

11

### 3. Results and Discussions

Figures 2.2 and 2.3 show typical temperature contours and flow velocity vector plots obtained from the CFD simulations, respectively. The outside temperature is 6.7 °C (44 °F), and three of the vents are operating to supply heated air at 35 °C (95 °F). The volumetric (mass) flow rate for each vent is 11.2 $m^3$/s (12.79 kg/s), for a total of 33.6 $m^3$/s (38.36kg/s) for this operating condition. One of the main features of the building internal flow, as shown in Fig. 2.2, is that in the current HVAC geometry the vent air tends to rise due to buoyancy effects before penetrating very far into the building interior. The heated air simply then travels towards the ceiling and out through the exhaust vents, without a chance to heat the target area. The flow through the bottom two rows of vents fares a similar fate, only reaching the bottom side of the turbine deck and not being able to heat the interior where much heating is needed. This loss of heating effectiveness is potentially critical under cold-weather conditions, where the lower deck temperatures must remain above freezing point due to all the water circulation equipment that resides in that section. The buoyancy-driven upward movement of air is also seen close to the boiler, where the boiler heat raises the temperature in the vicinity.
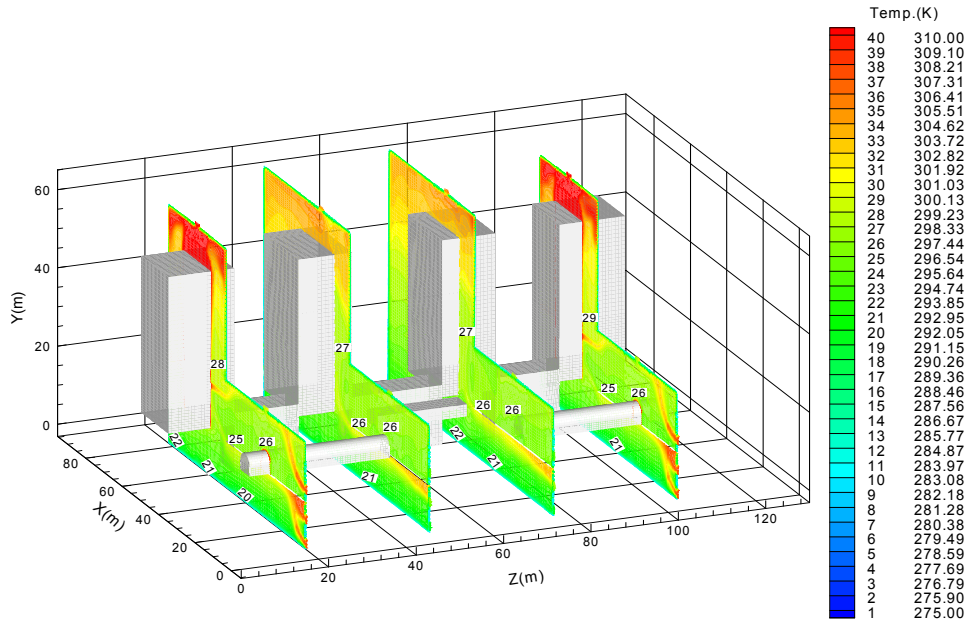
Fig. 2.2 Contour plot of temperature. The outside temperature is 6.7 °C (44°F), and three vents are supplying heated air at 35°C (95°F)

The flow paths area better visualized in the velocity vector plots in Fig. 2.3. The three insets, in addition to the overall cross-sectional view, are magnified views of the junction between the turbine deck and the boiler, exhaust vent above the boiler, and the turbine section, in a clockwise order from the top-left inset. Figure 2.3 again shows the rise of the heated vent air as it enters the turbine deck. The turbines themselves are additional obstacles in further penetration of the vent air, as recirculation pattern occurs on both sides of the turbine, as shown in the inset. The boilers generate heat, and thus are a heat source. Again due to buoyancy effect, this heated air from the boiler outside walls also rises and is vented out through the exhaust vents. As we shall see later in this paper, one method for optimizing the building HVAC is to make use of this kind of excess heat, to

13

supply warm air to cold regions. Without any active measures, this heated air from the boiler is wasted and sent out to the outside as shown in Fig. 2.3.
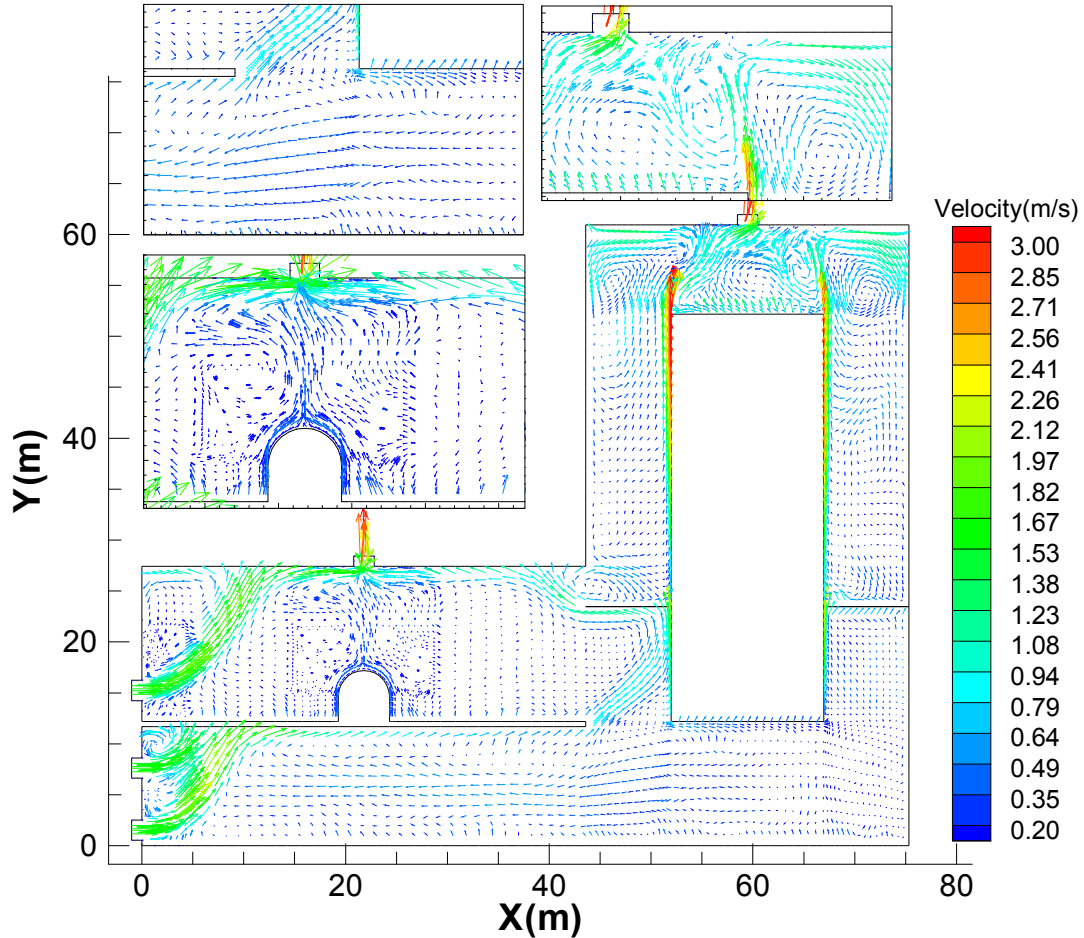


Fig. 2.3 Vector plot of the flow patterns under identical conditions as in Fig. 2.2

The heat fluxes from the boilers and turbines are initially estimated, and then adjusted to match the measured temperatures. This in turn serves as the validation of the computational simulations, once the heat fluxes are set to match the measured temperatures at several spots at two ambient temperatures, 6.7 ℃ (44 ℉) and 18.3 ℃ (65 ℉). For the latter temperature condition, the boiler was fitted with low-$NO_x$ burners, which resulted in substantially larger heat flux from the boiler surfaces. In fact, one of the

14

goals of this study was to alleviate the high temperatures in the boiler section under such operating conditions. The low-NO$_x$ burners operate by concentrating air close to the coal injector, and therefore minimizing contact with nitrogen in the air. The resulting flame is compact and close to the wall, increasing the wall heat flux. It can be observed in Figs. 2.4 and 2.5 that the simulation results match the measured temperatures quite well, except at the turbine deck (s=48, y=15.2, z=60 m) at ambient temperature of 6.7 ℃, where the discrepancy is just approximately 2 ℃. This is attributable to the recirculation pattern around the turbine (shown in Fig. 2.3), which causes fluctuations in the temperatures thus hampering both accurate measurements and simulations. At other temperatures and locations, the agreement between the computed and measured temperatures is quite good. It can be noticed in Fig. 2.5 that even though the outside temperature is moderate (18.3 ℃) the excess heat generated from the low-NO$_x$ burner and the boilers raises the temperature in the boiler section (x=60, y=35, z=30 m) to close to 50 ℃. The original HVAC design evidently did not include such considerations of additional heat from the low-NO$_x$ burner, and the current configuration results in unacceptably high temperatures for the operator particularly during summer days.
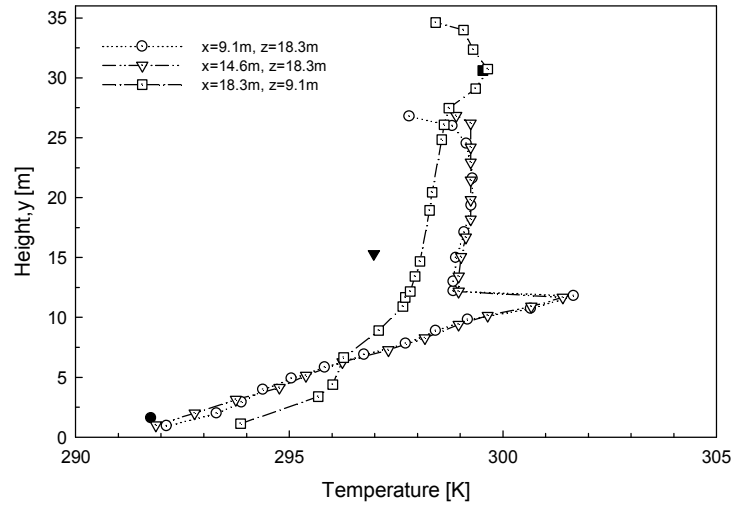
Fig. 2.4 Validation of the computational simulations with measured temperatures
($T_{ambient}$=6.7°C). Dark symbols represent the measured temperatures
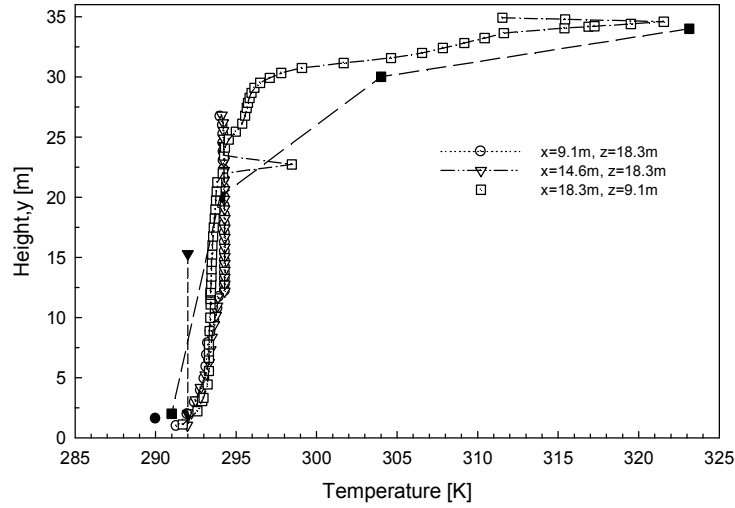


Fig. 2.5 Validation of the computational simulations with measured temperatures
($T_{ambient}$=18.3°C). Dark symbols represent the measured temperatures

Figure 2.6 shows the effect of increasing the number of vents which are supplying

heated air. The temperatures along a vertical line at (x=30 m, z=60 m) are plotted. The

volumetric flow rate and the temperatures of the heated air through each vent is the same,

at 11.2 m³/s and 35 ºC (95 ºF), respectively. During cold weather, additional vents up to

13 are sequentially turned on to maintain operating temperatures in the building, all this

16

in spite of the heat available from the boiler section. While this scheme certainly works, as shown by the increase in the temperatures in Fig. 2.6, the cost of vent operation with heated air increases due to the electrical power to run the vent fans and the unit heaters to raise the vent air temperature to 35 ºC. In addition, sending more heated air requires the additional exhaust vents to operate. The vent fan, electrical unit heater, and the exhaust fan are rated at 93.3, 12.5 and 5.6 kW, respectively, for a total of 111 kW. The main heat is generated from the heat exchange with the steam lines, and the unit heaters only augment this heat input. Assuming a typical electrical cost of $0.12/(kWh), each additional fan operation with heating will cost $320/day, $9590/month or $115,085/year. In the extreme event of all the 13 vents operating with heating, the electrical cost would amount to $124,670 for just one month. The current geometry is for a power generating plant, and thus any internal electrical energy use represents less power that can be sold to the public. It can be seen here that there are significant economic gains to be made through optimizations of the building HVAC configurations.
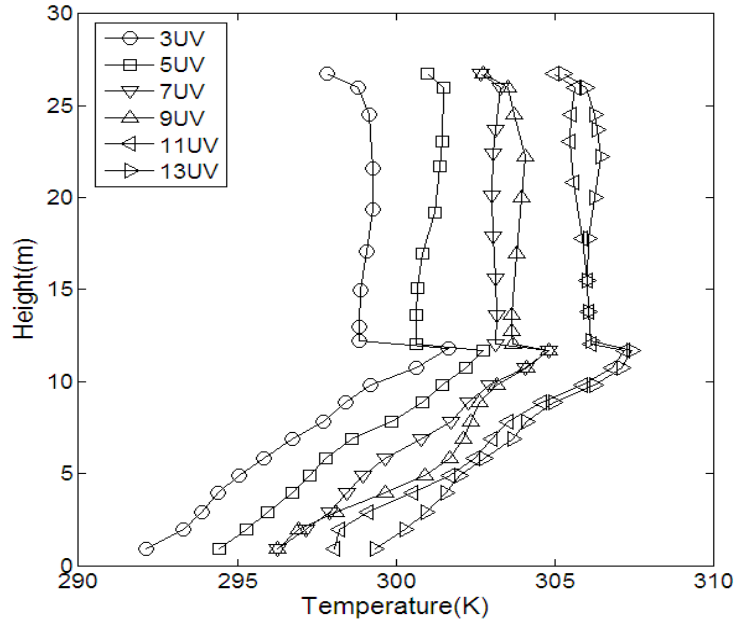
Fig. 2.6 Effect of the number of vents, $T_{ambient}$=6.7°C

The effect of the ambient temperature is shown in Fig. 2.7. A range of temperatures during the winter months at the current building location are considered:-20 to 43 °F (-28 to 7 °C or 244 to 280 K in Fig.2.7). Heating air is supplied through three of vents. The trends in the interior temperatures follow those of the outside ambient temperatures, except that they are higher than the outside temperatures due to the effect of heated vent air and the boiler heat. Lower elevation is at the lowest temperature, due to the natural convection effects which moves the air upward as shown earlier. The highest temperatures, under heating conditions, are found just underneath the turbine deck where the heated air gathers due to the buoyancy effects shown in Figs. 2.2 and 2.3. Thus, sending large volumes of heated air is not very effective if buoyancy causes the flow motion away from the target area. Again, at higher elevations the boiler heat is sufficient to maintain air temperatures in the range of 15 to 25 °.

18
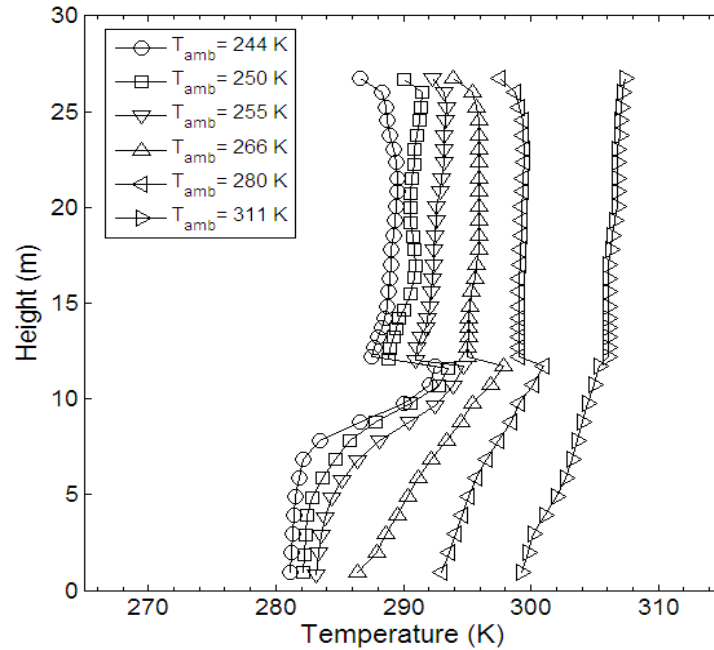
Fig. 2.7 Effect of the ambient temperature with three vents supplying heated air at 35°C

For optimization, we first consider the target area at lower deck (y<12 m) under low-temperature conditions. As noted above, the water circulation equipment in this area needs to be maintained at above freezing temperatures for normal operations. Although the temperature in this section is above 7 ºC (45 ºF) when the outside ambient temperature is -28 ºC (-20 ºF) as shown in Fig. 2.7, there are instances where the temperature can drop much lower. For example, the gates adjacent to this section are used to load or unload supplies; one or both the boilers may be shut down for scheduled maintenance; or some of the unit heaters may require service and not be available. In any event, it is of interest to optimize the vent configurations to see if less amount of power can be used to maintain the lower deck temperatures. One method is to direct all of the vent heat into this lower section since the turbine and boiler decks are already at relatively high temperatures. Figure 2.8 shows the effect of shutting down the top row of vents and diverting this flow all into the lower deck. This contour plot of temperature can

be compared with Fig. 2.2, where all the three rows of vents are operating. It can be seen

that due to higher flow rates there is a better penetration of the heated vent air into the

lower deck, but not enough to overcome the buoyancy effect. Overall, the temperature in

the lower deck tends to increase with this strategy, but by an average of about 2 ºC (5 ºF)

for the ambient temperature of 6.7 ºC (44 ºF). Thus, at least the heated vent air is not

directed into the turbine deck which does not require additional heating in this condition.

However, a more effective strategy is needed to make substantial gains in terms of energy

savings and better distribution of heat.
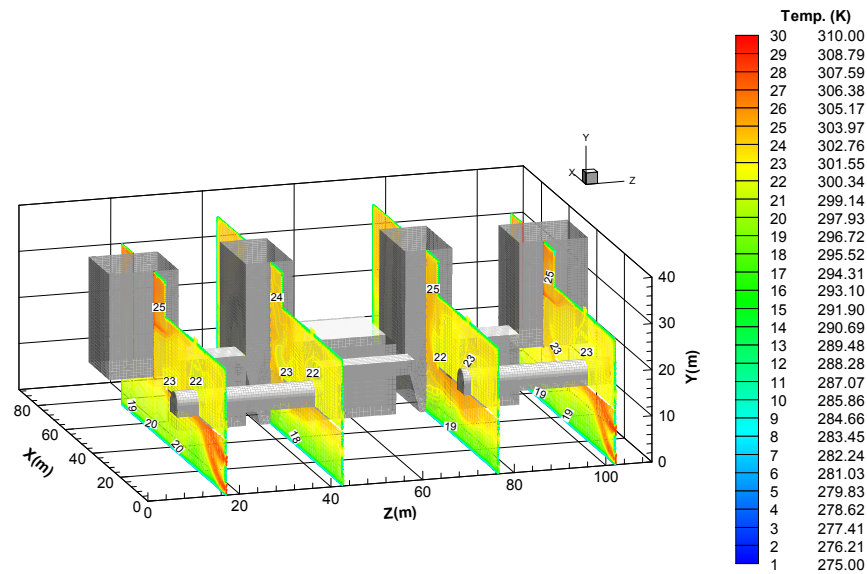


Fig. 2.8 Effect of directing the heated air to the lower deck, using the bottom two rows of vents, T$_{ambient}$=6.7°C

An alternative method to make use of the excess boiler heat is to force this heated air

down ward into the lower deck, instead of letting it escape through the exhaust vents.

Figure 2.9 show the effect of reversing the flow direction at the vents at the top of the boiler section. Instead of forcing the flow out, the vent flow is now reversed to let the outside air in. This would be achieved by reversing the polarity of the electrical motors, at no additional electrical usage. For comparison, the incoming heated air vent conditions are kept identical to those in Fig. 2.8, i.e., the bottom two vents are used to divert as much of the heated air into the lower deck. It can be seen that most of the gains are made in the boiler section, where the temperature increases about 2 to 3 ºC. The temperature increase does occur in the lower deck, due to the reversed flow, but is much less at about 1 ºC, as seen in Fig. 2.9. The reversal of the flow at the top vent is insufficient to overcome the tendency of the flow to rise due to buoyancy effect. Also, considering the distance from the top vent to the lower deck, the reversed flow at the top vent is not strong enough to force the heated air close to the boiler down into the lower deck.
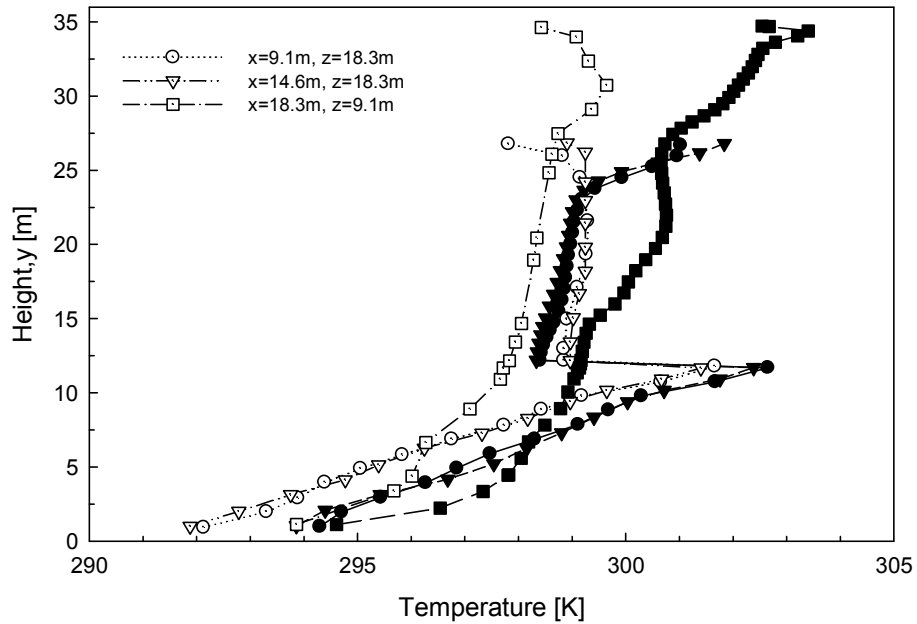


Fig. 2.9 Effect of reversing the flow at the exhaust vents above the boilers, $T_{ambient}$=6.7°C. Dark symbols represent the results of modification

Based on the examinations of the above permutations in the vent configurations, along with some insight from the basic principles of fluid mechanics and heat transfer, we can come up with a combined strategy of optimizing the temperature distributions during the low- and high-temperature conditions, as shown in Fig. 2.10. The logic is based upon the following basic behaviors of air flow in large buildings: (1) heated air tends to rise due to buoyancy; (2) obstacles represent pressure losses for the airflow, and sufficient pressure differential must be generated for the flow to overcome these pressure losses; and (3) optimum HVAC condition usually occurs when the temperature is uniformly distributed through complete circulation or removal of available heat. For a given fluid (air), the buoyancy effect essentially scales with the temperature difference between the heated and the surrounding. The pressure loss can occur from obstacles or friction with the walls and other components. The pressure differential can be created either by forcing the air with a fan, removing the flow obstruction or using open vents at the opposite end. These are elementary facts from fluid mechanics and heat transfer; however, when applied to large-scale structures as guided with CFD simulation results, they can be quite effective. The original building designers may have had other priorities and/or constraints aside from HVAC optimizations. Understanding of the flow patterns and temperature distributions, based on the computational simulations as done in this work, allows the plant operators to make relatively simple notifications, so that optimum vent configurations can be found for various ambient conditions.

Heating under Cold
Temperature Conditions

Cooling under High
Temperature Conditions
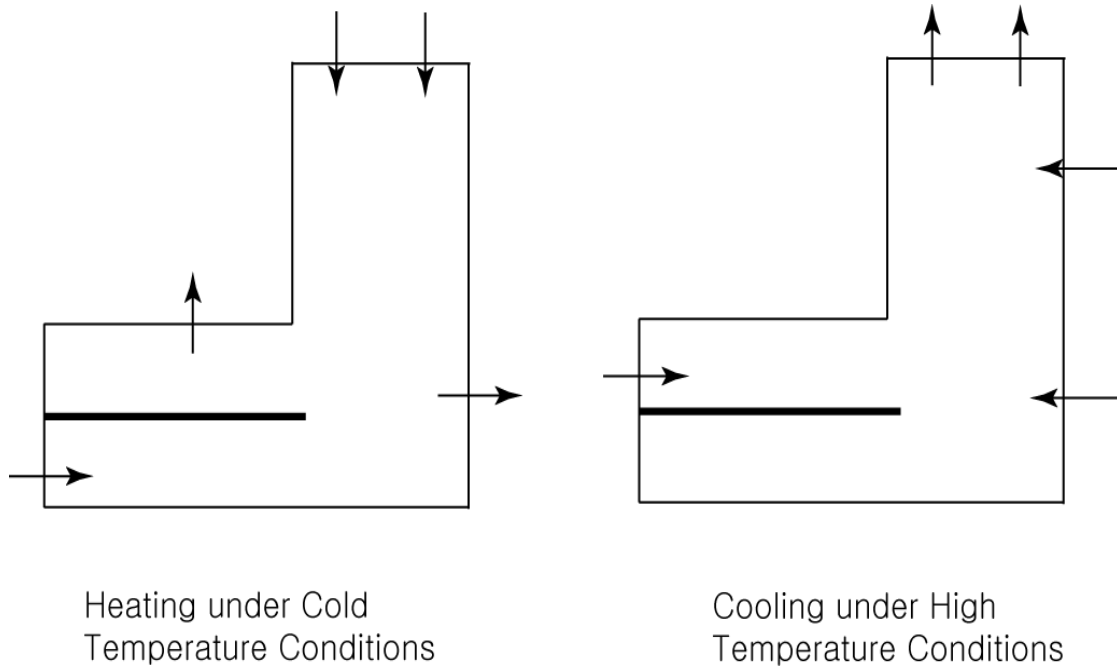
Fig. 2.10 Schematic of the two optimized configurations for low- and high-temperature conditions

First, we look at the optimized configuration for low-temperature conditions. For the low-temperature conditions, the most critical section is the lower deck with the water distribution equipment. Thus, the vent flow at the top of the boiler section is reversed to force as much of the high-temperature air downward. To draw the heating air further into the lower deck, i.e., to increase the pressure differential, the back vents now exhaust the air outward, as shown in Fig. 2.10. It can be seen in Fig. 2.11 that there are appreciable gains of 1 to 5 ºC increase through the reversal and opening of the back vents. However, most of the gains occur at high elevations close to the boiler, as it is relatively easy to trap the heat from the boiler through the vent flow reversals. The lower elevations are still difficult to control at low temperatures due to natural tendency for warm air to rise. The reversed flow at the top of the boiler section is not sufficient to overcome the buoyancy

effects. Intermediate fans located internally may be needed to make maximum use of the

boiler heat toward the lower sections.
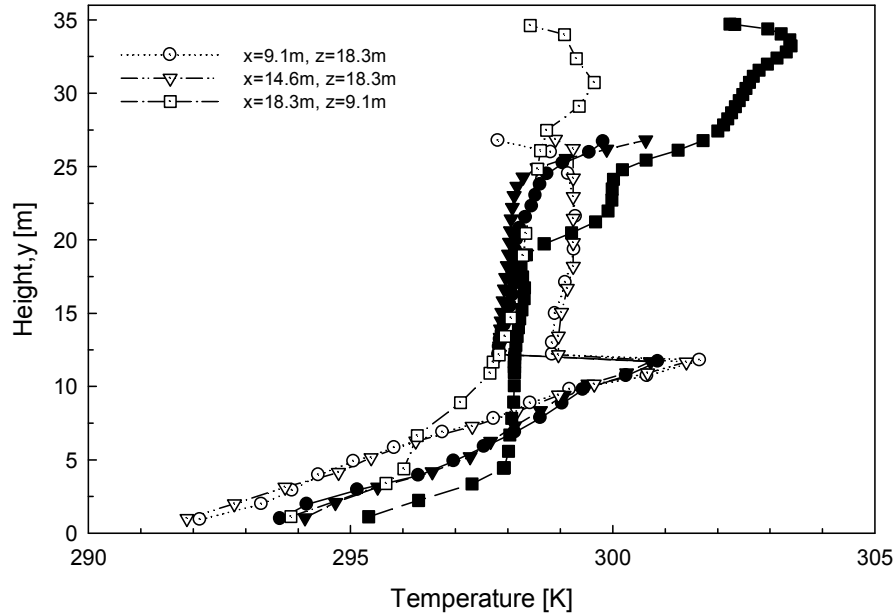


Fig. 2.11 Contour plot of temperature under optimized configuration for low-temperature
conditions. Dark symbols represent the results of modification

Figure 2.12 shows the total effect of the optimized configuration shown in Fig. 2.10

for the high-temperature conditions. The most critical region is the boiler section under

these conditions, where the heat tends to accumulate, particularly with the low-$NO_x$

burner operating. Thus, this hot air is allowed to escape through the exhaust vents at

maximum possible flow rates. To assist in this process, two set of back vents are added to

create a natural flow of air inward; i.e., the heated air will tend to exhaust rapidly through

the top vents due to buoyancy force, creating low-pressure to draw in outside air through

the back vents. The front inlet vents also blow the outside air to create additional pressure,

while the turbine exhaust vents operate normally. Here, the additional cooling effect due

to the optimized configuration is substantial with a 12 ℃ decrease in the maximum

24

temperature. Aside from the high elevations close to the boiler, the temperature profiles are more or less uniform reflecting the optimum distribution of vent air.
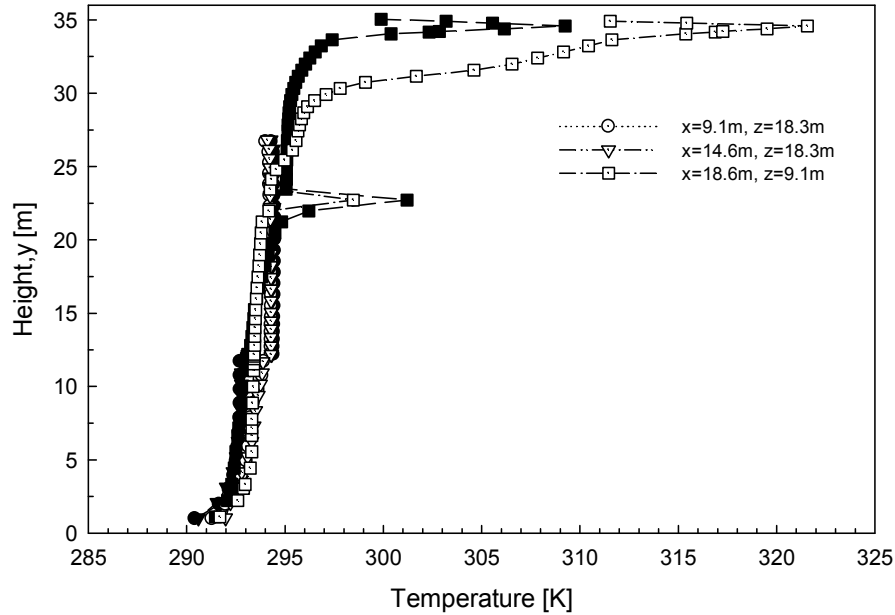


Fig. 2.12 Contour plot of temperature under optimized configuration during high-temperature conditions. Dark symbols represent the results of modification

## 4. Conclusions

For reduced carbon dioxide and pollutant emission, it is as important to minimize energy use on the consumption side, as maximizing the efficiency on the power supply side. In this paper, we have used CFD methods to characterize and optimize the HVAC operation in a large-scale building: a power-plant structure where the internal electrical energy use can be up to 11% of the out of 435MW gross generation capacity. We used a fully three-dimensional model of the power plant building replicating the complex internal and external geometries, in order to computationally simulate the flow and temperature distributions under a wide range of ambient and HVAC operating conditions. The flow patterns and temperature distributions in a large building structure, measuring

25

80 m in width, 120 m in length and 60 m in height, have been computationally simulated in some details, with the temperatures validated through spot measurements. Identification of the problematic flow patterns and temperature mis-distributions lead to some corrective measures, or optimization of the temperature distributions. When basic principles of fluid mechanics and heat transfer are applied, along with detailed understanding of the flow patterns and temperature distributions as provided by computational simulations, substantial improvements under both high- and low-temperature conditions can be achieved, in most cases with relatively simple, implementable modifications.

References

1. Chami, N. and Zoughaib, A. 2010. Modeling natural convection in a pitched thermosyphon system in building roofs and experimental validation using particle image velocimetry. *Energy and Buildings*, 42 (8): 209-216.

2. Cheng, C.-H. and Hung, K.-S. 2005. Experimental and numerical study of three-dimensional flow field in minienvironment. *Energy and Buildings*, 37 (6): 579-586.

3. Clark, J.A. 2001. *Energy simulation in building design.* London: Butterworth-Heinemann.

4. FLUENT. 2006. *Fluent 6.3 user's guide*. Lebanon: Fluent Incorporation.

5. Gan, G. 1995. Evaluation of room air distribution systems using computational fluid dynamics. *Energy and Buildings*, 23 (2): 83-93.

6. Gosselin, J.R. and Chen, Q. 2008. A computational method for calculating heat transfer and airflow through a dual-airflow window. *Energy and Buildings*, 40 (4): 452-458.

7. Kuznik, F., Rusaouën, G., Hohotă, R. 2006. Experimental and numerical study of a mechanically ventilated enclosure with thermal effects. *Energy and Buildings*, 38 (8): 931-938.

8. Lin, Y. and Zmeureaunu, R. 2008. Computer model of the air and thermal phenomena inside a large dome. *Energy and Buildings*, 40 (7): 1287-1296.

9. Ng, K.C., Kadirgama, K., and Ng, E.Y.K. 2008. Response surface models for CFD predictions of air diffusion performance index in a displacement ventilated office. *Energy and Buildings*, 40 (5): 774-781.

10. Ren, Z and Stewart, J. 2003. Simulating air flow and temperature distribution inside buildings using a modified version of COMIS with sub-zonal divisions. *Energy and Buildings*, 35 (3): 257-271.

11. Sinha, S.L., Arora, R.C., and Roy, S. 2000. Numerical simulation of two-dimensional room air flow with and without buoyancy. *Energy and Buildings*, 32 (1): 121-129.

12. United States Global Change Research Program. 2009. *Global climate change impact in the United States: Chapter on Energy Supply and Use.* New York: Cambridge University Press.

**CHAPTER 3**

**ESTIMATION OF SPRAY DROP SIZE AND VELOCITY DISTRIBUTIONS**

## 1. Introduction

Drop size and velocity distributions from sprays are important for the obvious reasons of influencing the subsequent vaporization and combustion processes. A vast number of works exist in empirical modeling, experimental measurements and detailed computational simulations of drop size and velocity distributions in various spray configurations (Ahmadi et al. 1993; Babinsky and Sojka 2002; Cousin et al. 1996; Dumouchel 2007; Dumouchel and Boyaval 1999; Herrmann 2010a; Herrmann 2010b, Herrmann and Gorokhovski 2009; Lee and Mitrovic 1996; Lee and Robinson 2011; Li et al. 1991; Li et al. 1988; Rothe and Block 1977; Ruff et al. 1991; Sellens and Brzustowski 1986; Sirignano and Mehring 2000). The references represent a very small subset of the existing body of work, and we have referenced only those that have direct relevance for this study. Recently, we presented a new, alternate framework for calculating the drop size distribution and velocities, based on the integral form of the conservation equations of mass, momentum and energy (Lee and Robinson 2011). In this approach, the conservation equations, after some algebraic work, render themselves solvable through iterative methods. The key is to use the integral form of the conservation equations so that the input injection parameters are related to the output spray parameters, without having to resolve the details of the atomization physics. Due to the drop size and velocity effects are present in the conservation equations, both the drop size and velocity distributions can in principle be calculated, although in this work we first focus on the effects of the momentum on the mean drop size.

28

Using an integral formulation of the conservation equations, direct calculations of the mean drop size and size distributions were possible, which agreed favorably with experimental results and correlations (Lee and Robinson 2011). However, the energy equation that did not include the viscous dissipation term led to large underestimation of the mean drop size. Also, the treatment of the momentum equation was, under some injection conditions, computationally not very stable. From that work (Lee and Robinson 2011), it was learned that viscous dissipation, or potentially some other mechanisms to balance the initial injection kinetic energy, is required for correct estimation of the drop size. This point has also been asserted by Sirignano and Mehring[16]. This alone may be a useful feature of this theoretical framework in the sense that we can examine which mechanisms need to be included in correctly balancing the spray energy equation.

In view of this, we consider an appropriate form of the viscous dissipation term in the integral form of the conservation equation, and examine the effects of momentum terms (such as the density ratio and injection angles) on the computed drop size. As will be discussed later, it is the conversion of the spray kinetic energy to other forms of energy that determines the drop size; and we would like to examine the effect of velocity, density ratio and atomization length, which are factors associated with the spray momentum. As noted above, the velocity or the momentum calculation was less than stable in our initial study (Lee and Robinson 2011), where the algorithm had difficulty converging at certain injection conditions. To remedy this weakness, we use a momentum treatment adopted from Rothe and Block[17]. Using this set of editions to the integral form of the spray conservation equations, we can further examine the effects of injection parameters on the resulting drop size.

29

## 2. Literature Review

Spray breakup mechanism is very complicated procedure so that it needs a careful modeling. Many models have been devised and used for explanation of complex breakups of spray droplets in the pressure-atomized spray. Among them, three important models are noteworthy. One is the Taylor-analogy break-up, another is the wave growth theory, and the other is the maximum entropy method.

Taylor-analogy breakup model is a classic and popular method for computing droplet breakup. It is based on Taylor's analogy between a distorting and oscillating droplet and a spring mass system. Three terms on the spring-mass system such as external force, spring force, and restoring force of spring is analogous to three terms on the droplet such as drag force of droplet, viscous force of droplet, and surface tension of droplet, respectively shown in Fig. 3.1. It makes an equation closure. Verbally, when the droplet oscillations grow to a critical value, the droplet will break up into a number of smaller subsequent droplets. As a droplet is distorted from the most frequent shape of a droplet, a spherical droplet, the drag coefficient will dynamically change accordingly. This model is known for getting the best result when low Weber number spray is analyzed.
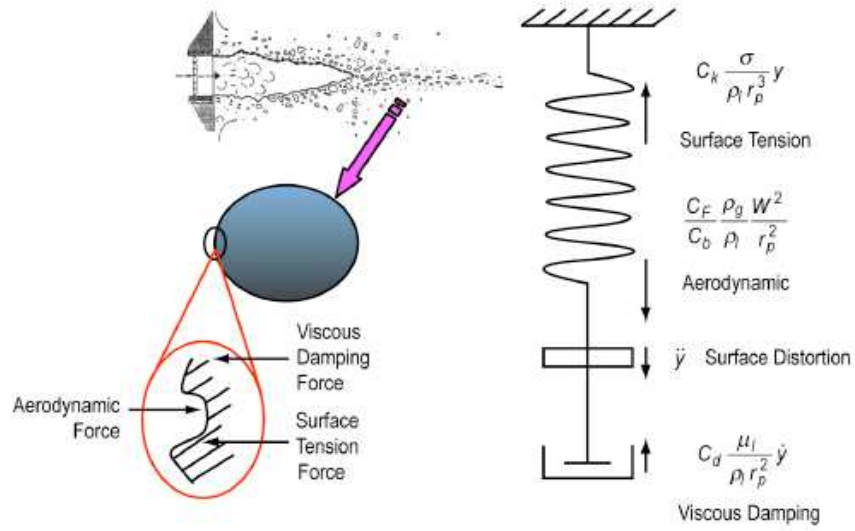
Fig 3.1. Schematic showing analogy of forces acting on a liquid droplet and spring-mass system

The governing equation above for a damped, forced oscillator is written below.

$$m\frac{d^2x}{dt^2} + d\frac{dx}{dt} + kx = F$$

By rearranging the second and the third term on the left hand side to the right,

$$m\frac{d^2x}{dt^2} = F - d\frac{dx}{dt} - kx$$

where x is the displacement of the droplet equator from its spherical position.

$$F = C_F m \frac{\rho_g u^2}{\rho_l r}$$

$$k = C_k m \frac{\sigma}{\rho_l r^3}$$

$$d = C_d m \frac{\mu_l}{\rho_l r^2}$$

31

where $\rho_l$ and $\rho_g$ are liquid density and gas density respectively, u is the relative velocity of the droplet, r is the spherical droplet radius, $\sigma$ is the droplet surface tension, $\mu_l$ is the droplet dynamic viscosity and $C_F, C_k,$ and $C_d$ are the dimensionless constants whose values are 1/3, 8, and 5 respectively according to experiments and theory (Lamb, 1945).

By equating the parent droplet energy and the subsequent droplet energy, the Sauter-Mean Diameter can be derived as written below.

$$4\pi r^2 \sigma + K\frac{\pi}{5}\rho_l r^5 \left[\left(\frac{dy}{dt}\right)^2 + \omega^2 y^2\right] = 4\pi r^2 \sigma \frac{r}{r_{32}} + \frac{\pi}{6}\rho_l r^5 \left(\frac{dy}{dt}\right)^2$$

By rearranging terms, SMD is written below by assumption that $y = {}^X\!/_{C_b r} = 1$, $C_b = 0.5$, $K \sim O(\frac{10}{3})$ and $\omega^2 = {}^{8\sigma}\!/_{\rho_l r^3}$.

$$r_{32} = \frac{r}{1 + \frac{8Ky^2}{20} + \frac{\rho_l r^3 \left(\frac{dy}{dt}\right)^2}{\sigma}\left(\frac{6K-5}{120}\right)}$$

Velocity of subsequent droplets is derived by normal velocity of the first time derivative of the displacement of the parent droplet which is $\frac{dx}{dt} = C_v C_b r \frac{dy}{dt}$, where $C_v \sim O(1)$.

Wave growth theory is an alternative to the Taylor analogy breakup model which is proper for high Weber number flows (Reitz 1987). It considers the breakup of droplets to be induced by the relative velocity between the gas and liquid phases. Its assumptions are that the time of breakup and the resultant droplet size are related to the fastest growing Kelvin-Helmholtz instability which is derived from the jet stability analysis. The wavelength and growth rate of Kelvin-Helmholtz instability are used for prediction of details of the subsequent droplets. This model is appropriate when high speed injections,

which the Kelvin-Helmholtz instability dominates droplet breakup, usually, We>100, are observed.

Maximum entropy method is classified as one of three models to predict spray drop-size distributions (Babinski and Sojka 2002). Among three models, the empirical method is made up of determination of a mathematical form that fits the experimental data from a number of operational variations. It has produced many empirical mathematical spray drop-size distributions such as the log-normal, upper-limit, root-normal, Rosin-Rammler, Nukiyam-Tanasawa, and log-hyperbolic distributions. In advance, it is not possible for us to know which of these distributions will be better to reproduce a given situation. The number of parameters that these distributions contain determines the ability to fit spray drop size distributions. The discrete probability method postulates that poly-dispersion in liquid sprays is due to initial condition fluctuations (Babinski and Sojka 2002). A deterministic model is used for prediction of a specific diameter to a given set of initial conditions. The poly-dispersion of the drop-size is obtained by description of the fluctuating initial conditions by a continuous probability density function. Essentially, the poly-dispersion methods define a transformation using the breakup model as a transform function from a continuous probability density function as an input PDF to PDF of the drop-size distribution. Its difficulty comes from the ambiguous determination of replacement of the initial condition fluctuation with the drop diameter distribution. This method has a known limitation because, for many atomization processes which have high energy, the origin of poly-dispersion is not solely connected to initial condition fluctuations.

Maximum Entropy Formalism (MEF) is a method of inference allowing the determination of a probability density function from a limited amount of information (Dumouchel 2009). This information specifies properties that the distribution must satisfy and comes from a partial knowledge of the distribution. Among the distributions that satisfy the available information, the MEF states the most likely and/or least biased solution is the one whose statistical entropy is a maximum. Motivations of the MEF method are that liquid atomization is not a deterministic process and may not be modeled by a deterministic method and spray drop size and velocity distribution can be represented by a probability distribution. Especially for a drop size distribution, the number-based and volume-based drop diameter distributions are commonly used in the literature. Assume that a spray containing $N_T$ droplets. Each droplet is assumed spherical and therefore fully characterized by a diameter D. The droplet diameter ranges in the interval from the minimal diameter to the maximal diameter denoted as $[D_{min}, D_{max}]$. This interval is divided into $n_c$ classes $[D_i - \Delta D_i/2, D_i + \Delta D_i/2]$ where $D_i$ and $\Delta D_i$ are the median diameter and the width of class i, respectively. The droplets are distributed in this class series. It is assumed that all droplets belonging to a given class i have the same diameter equal to the class median diameter $D_i$. The number of droplets in class i becomes $\sum_{i=1}^{n_c} N_i = N_T$. Similarly, the total volume of liquid $V_T$ contained in the spray and the liquid volume $V_i$ contained in each class are introduced and becomes $\sum_{i=1}^{n_c} V_i = V_T$. The spray drop size distribution is characterized by the number fraction distribution $P_{ni}$ and the volume fraction distribution $P_{vi}$ and defined by $P_{ni} = {N_i}/{N_T}, P_{vi} = {V_i}/{V_T}$.

Continuous number-based drop size distribution $f_n(D)$ and volume-based drop size distribution $f_v(D)$ are defined by $P_{ni} = \int_{D_i-\Delta D_i/2}^{D_i+\Delta D_i/2} f_n(D)dD$, $P_{vi} = \int_{D_i-\Delta D_i/2}^{D_i+\Delta D_i/2} f_v(D)dD$. Note that despite similarity of definitions of number-based drop size distribution and volume-based drop size distribution, only number-based drop size distribution is a probability distribution.

A mean drop-diameter series $D_{kl}$ by Mugele and Evans[15] in Table 3.1 is commonly used to characterize liquid spray drop-size distributions and defined by

$$D_{kl} = \left( \frac{\int_0^\infty f_n(D)D^k dD}{\int_0^\infty f_n(D)D^l dD} \right)^{\frac{1}{(k-l)}} = \left( \frac{\int_0^\infty f_v(D)D^{k-3} dD}{\int_0^\infty f_v(D)D^{l-3} dD} \right)^{\frac{1}{(k-l)}}$$

Table 3.1. Mean Drop Diameter Designation

| k | l | Designation | Relation |
|---|---|---|---|
| 1 | 0 | Number mean diameter | $N_T D_{10} = \sum_{i=1}^{n_c} N_i D_i$ |
| 2 | 0 | Surface mean diameter | $N_T \pi D_{20}{}^2 = \sum_{i=1}^{n_c} N_i \pi D_i{}^2$ |
| 3 | 0 | Mass mean diameter | $\dfrac{N_T \pi D_{30}{}^3}{6} = \sum_{i=1}^{n_c} \dfrac{N_i \pi D_i{}^3}{6}$ |
| 3 | 2 | Sauter mean diameter | $\dfrac{D_{32}}{6} = \dfrac{\sum_{i=1}^{n_c} \dfrac{N_i \pi D_i{}^3}{6}}{\sum_{i=1}^{n_c} N_i \pi D_i{}^2}$ |
| 4 | 3 | De Brouckere | $D_{43} = \int_0^\infty f_v(D)dD$ |

The mean diameter $D_{10}$ corresponds to the arithmetic mean of the number-based distribution $f_n$ and $D_{43}$ corresponds to the arithmetic mean of the volume-based

distribution $f_v$. The Sauter mean diameter $D_{32}$ corresponds to the diameter of the drop that has the same volume to surface area ratio as the entire spray. Explicit relation between number-based distribution $f_n$ and volume-based distribution $f_v$ can be derived using above equations such as $f_v(D) = \left(\frac{D}{D_{30}}\right)^3 f_n(D)$.

The distributions defined can be generalized by the characteristic length such as the diameter D or surface of each drop $\pi D^2$. Liquid spray drops might be also described by a joint size-velocity distribution, each droplet of a spray having their own velocity.

The MEF method states that the most likely and/or the least biased probability distribution $P_i$ that satisfies a set of constraints that expresses known characteristic of the target distribution is the one whose Shannon's entropy S, $S = -k \sum_i P_i \ln(P_i)$ where k is constant, is maximum. The constraints can be defined by $\sum_i P_i g_{r,i} = \langle g_r \rangle, r = 1, \dots, m$ where the quantities $\langle g_r \rangle$ are known moments of the distribution and constitute the available information as well as $\sum_i P_i = 1$. Numerous probability distributions can be satisfied by a given set of constraints, but there is only on whose entropy S is maximum. If Lagrange multipliers are used, it can be demonstrated that the probability distribution is given by $P_i = \exp\left(-\lambda_0 - \sum_{r=1}^{m} \lambda_r g_{r,i}\right)$ where the Lagrangian multipliers $\lambda_i, i = 0, 1, \dots, r$ must be determined. By using the properties of the probability density function above, the relation between the multipliers can be given by $\exp(\lambda_0) = \sum_i \exp\left(-\sum_{r=1}^{m} \lambda_r g_{r,i}\right)$ as well as $\langle g_r \rangle \exp(\lambda_0) = \sum_i g_{r,i} \exp\left(-\sum_{r=1}^{m} \lambda_r g_{r,i}\right)$. The m moments of $\langle g_r \rangle$ allows to determine the Lagrangian multipliers. Suppose that the solution state $\psi$ which is uniformly discretized and contains all permissible states is defined, a PDF f is defined by $P_i = \int_{\psi_i - \Delta\psi_i/2}^{\psi_i + \Delta\psi_i/2} f d\psi$ where $\int_\psi f d\psi = 1$ and $\int_\psi f g_r d\psi = \langle g_r \rangle \, r = 1, \dots, m$. Finally, the

statistical entropy of the PDF is $S = -k \int_\psi f \ln(f) d\psi = 1$. The PDF that maximizes the statistical entropy S subject to the set of constraints in the solution state $\psi$ is $f = \exp(-\lambda_0 - \sum_{r=1}^{m} \lambda_r g_r)$.

The first attempt of prediction of the liquid spray drop size distribution on the basis of the MEF method is to consider the breakup of a liquid sheet in the vicinity of the breakup region (Sellens and Brzustowski, 1986). The constraints are expected to be satisfied according to the conservation laws such as conservation of mass, momentum, and energy. These constraints required to be explained in detail by account of each drop, so the solution is defined by drop diameter D and velocity U in the solution space $\psi$ denoted as $d\psi = dDdU$. The liquid sheet thickness is t and liquid velocity $U_s$ is given and non-dimensionalized by the spray mass mean diameter $D_{30}$ and the liquid sheet velocity $U_s$. Non-dimensionalized parameters are denoted as $\delta = {}^D/_{D_{30}}$ for the diameter, $\tau = {}^t/_{D_{30}}$ for the sheet thickness, and $u = {}^U/_{U_s}$ for the velocity. They wrote two separate constraints for the kinetic energy and the surface energy in order to explain irreversibility of certain energy transformations. In an atomization process, kinetic energy is transformed into surface energy but the reverse transformation is not possible. The set of constraints is made up of the normalization, mass conservation, momentum conservation, kinetic energy conservation, and surface energy conservation, which are denoted as

$\iint_\psi f d\delta du = 1, \iint_\psi f\delta^3 d\delta du = 1 + S_m, \iint_\psi f\delta^3 u d\delta du = 1 + S_{mv}, \iint_\psi f\delta^3 u^2 d\delta du = 1 + S_{ke}$ and $\iint_\psi f\delta^2 d\delta du = \frac{1}{3\tau} + S_s$. Where the source terms $S_m, S_{mv}, S_{ke}$, and $S_s$ account for losses of mass, momentum, kinetic energy, and surface energy during breakup,

respectively. The joint diameter-velocity distribution is derived following the general form of the MEF method above (Sellens and Brzustowski, 1986), denoted as

$$f = \exp\left(-\lambda_0 - \lambda_1 \delta^2 - \lambda_2 \delta^3 - \lambda_3 \delta^3 u - \lambda_4 \delta^3 u^2\right)$$

By integrating this function over the velocity space, the number-based drop diameter distribution is derived and denoted as

$$f_n(\delta) = \sqrt{\frac{\pi}{4\lambda_4 \delta^3}} \times \left( \mathrm{erf}\left( u_m \sqrt{\lambda_4 \delta^3} + \frac{\lambda_3}{2} \sqrt{\frac{\delta^3}{\lambda_4}} \right) - \mathrm{erf}\left( \frac{\lambda_3}{2} \sqrt{\frac{\delta^3}{\lambda_4}} \right) \right)$$

$$\times \exp\left(-\lambda_0 - \lambda_1 \delta^2 - \lambda_2 \delta^3 - \lambda_3 \delta^3 u - \lambda_4 \delta^3 u^2\right)$$

The number-based drop diameter distribution derived above is shown to be very similar to the shape of the Rosin-Rammler distribution which is a two-parameter empirical drop-diameter distribution extensively used to represent spray drop size distribution. However, there is a drawback to this since the probability associated with the smaller drop sizes is much larger than expected. Then the left tail of the distribution does not agree with almost all experimental observations. Therefore, a non-zero momentum source term is needed to produce an initial velocity distribution. By coupling the initial droplet velocity distribution with a simple air drag model, the downstream velocity distribution was investigated and it shows that for all drop categories, the velocity variance decreases very fast towards zero whatever the initial velocity distribution is used, in other words, mean velocity should be used to characterize any drop category. There are a number of different models using the MEF method in order to make up for the deficit of the basic modeling of its own and refer to Dumouchel[5].

This paper is motivated by the MEF method which uses the optimization scheme for maximizing the entropy in order to find the appropriate PDF by a partial knowledge of a target distribution. The Lagrangian multipliers which are included in the number-based drop diameter distribution have been used for the well-known relaxation scheme in order to find the optimal values subject to hard constraints by changing hard constraints to the optimal objective functions with the help of multiplication of the constants λs by hard constraints. Based on the optimization method and the basic probability theory, derivations can be closed and utilized further.

### 3. Mathematical Formulation and Results

The basic integral form of the conservation equations for mass, momentum and energy has been shown in our previous work (Lee and Robinson 2011). We present the equations here for the purpose of placing the editions to this work in context. We consider a control volume that envelops the spray including all its complex break-up and atomization mechanisms. The underlying concept is to relate the mass, momentum and energy of the spray at the injector exit, to those at a downstream location where the spray is fully atomized. For this control volume, the conservation equations of mass and energy of the liquid phase are as follows:

$$\rho_L u_{inj} A_{inj} = \int_{u=0}^{u_{max}} \int_{D=0}^{D_{max}} n\overline{p}(D,u)\frac{\pi D^3}{6}\rho_L u A \, dD \, du \approx \frac{\pi}{6}n\rho_L \overline{u}A\sum_{i}^{N} p(D_i)D_i^{3}\Delta D_i$$

39

$$\rho_L \frac{u_{inj}{}^3}{2} A_{inj} = \frac{\pi}{12} n\rho_L\bar{u}^3 A \sum_i^N p(D_i)D_i{}^3\Delta D_i + n\bar{u}A\pi\sigma \sum_i^N p(D_i)D_i{}^2\Delta D_i$$

$$+ K\mu_L \frac{u_{inj}{}^2 - \bar{u}^2}{d_s{}^2} \frac{4}{3} Ax$$

The mass conservation is achieved by equating the injected mass flow rate with the mass of the droplets contained in a volume swept by the average drop velocity, $\bar{u}$, over a spray area, A. Again, the velocity distribution is simplified to an average drop velocity, to first focus on the drop size calculations. The calculation of the drop size distribution has been demonstrated in our previous work (Lee and Robinson 2011). The cross-sectional area, A, represents the physical extent of the spray at the plane where full atomization is achieved, which could also be determined by the spray cone angle and the atomization length. The drop number density is n, while $\rho_L$ and $D_i$ are the liquid density and droplet diameter, respectively. $p(D_i)$ is the normalized drop size distribution, and $D_i$ the drop size bin width.

In our previous treatment of the momentum equation, the algorithm at times led to non-convergent solutions. We find a method for robust computation of the spray momentum, based on the work of Rothe and Block[17]. In this treatment, combined liquid and entrained gas mass are used to satisfy the mass conservation. A standard liquid-phase dynamical model is then used, where the liquid momentum is attenuated by the aerodynamic drag force (due to the relative motion of the liquid phase with respect to the entrained gas). In this manner, the gas velocity is introduced in the mass conservation, and the two equations are used to solve for the gas and liquid gas velocities. The mass and momentum balances have the following basic form (Rothe and Block 1977):

$$\rho_L u_{inj} A_{inj} = \rho_L \bar{u} A + \rho_g u_g A$$

$$\frac{\pi}{6} D^3 \rho_L \bar{u} \frac{d\bar{u}}{dx} = -C_D \frac{\pi}{4} D^2 \rho_g \frac{\left(\bar{u} - u_g\right)^2}{2}$$

Using the above momentum balance, we can compute the liquid and gas velocities for a fixed droplet size, D, the results of which are shown in Fig. 3.2. The liquid and gas velocities normalized by the injection velocity, $u_{inj}$, are plotted as a function of the normalized distance from the injector, $x/d_{inj}$, for various density ratios. As can be seen in mass conservation equation above, the spray area is a parameter, which is determined by the spray cone angle and the atomization length. Here the atomization length is defined as the axial distance from the injector where all the liquid has been dispersed into geometrically-shaped (spherical) drops. This is a very useful feature in that the injection properties such as the spray cone angle and atomization length can be directly entered into the algorithm. The injection parameters will then affect the spray momentum and kinetic energy downstream, and therefore the drop size. Also, density ratio between liquid and gas is a parameter in momentum treatment equation. In Fig. 3.2, the spray cone angle of 25 degrees is used, while the plots for various density ratios are included. At all conditions, the liquid momentum decays as a function of the distance, with the decrease more pronounced at low density ratios (large gas density). The entrained gas velocity is typically small, in comparison to the liquid-phase velocity.
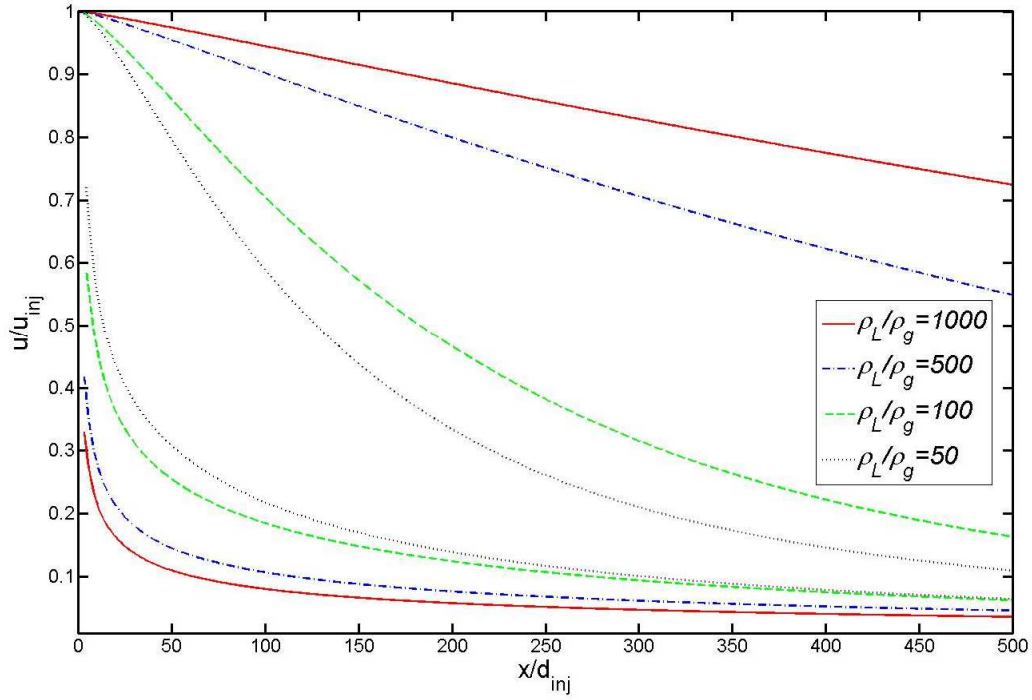
Fig. 3.2. Normalized liquid and gas velocities, for spray cone angle of 25 degrees (the top four lines are for the liquid-phase velocities, while the bottom four are for the gas-phase)

An argument could be made against the use of the above dynamical relationships, as the method assumes that the liquid is in a drop form of some representative diameter, from the injector exit. The dynamics of the liquid core and ligaments are quite different from that of a spherical drop. However, we are interested not in the liquid core or the ligament velocity, but only in the final drop velocity at a downstream location where the atomization is assumed to be complete. The momentum is evidently high in the near-injector region, and is retarded by an appreciable amount mostly at downstream locations. Thus, we consider the momentum balance by Rothe and Block[17] to provide a reasonable estimate of this drop velocity in the entrained gas velocity field at the end of the atomization process.

For the energy equation, the injected kinetic energy is re-distributed between the droplet kinetic and surface energy terms through the atomization process. σ is the surface tension in [N/m²]. It was found that a viscous dissipation term is needed for the computed drop size to follow experimentally observed range of values. In the integral form, the viscous dissipation term has the unit of the energy dissipation rate multiplied by volume. Here, we try a form that is proportional to the difference in the velocities squared divided by the spray lateral length scale ($d_s$). This is roughly the velocity gradient squared in the lateral direction. This term is then multiplied by the spray volume, and the resulting form,

$$\mu_L \left( \frac{\partial u}{\partial y} \right)^2 (Spray\,Volume) \sim K\mu_L \frac{u_{inj}^2 - \bar{u}^2}{d_s^2} \frac{4}{3} Ax$$ , is inserted in the energy equation above

as the viscous dissipation term. There is a constant factor of K, which is calibrated based on comparison with experimental data, and $d_s$ is the lateral length scale of the viscous shear stress. If we take this length scale to be equal to the spray diameter corresponding to A, then this length is canceled and the only length scale remaining is x, the atomization length. To be rigorous, the viscous dissipation should be proportional to the square of the velocity difference, not to the difference of the velocities squared. We have tried several forms of the viscous dissipation term, and the current form yields the best agreement with experimental data. Thus, this term is subject to further refinements, through more comprehensive comparisons with experimental data under wider range of injection conditions.

After the above steps, we can utilize one of the convenient aspects of this framework: an expression for the Sauter Mean Diameter (SMD) naturally appears out of the mass and

energy equation defined above (Lee and Robinson 2011). To start, we can solve for the

drop number density, n, from the mass conservation equation above, to obtain

$$n = \frac{\rho_L u_{inj} A_{inj}}{\frac{\pi}{6} \rho_L \bar{u} A \sum_i^N p(D_i) D_i^3 \Delta D_i}$$

Substitution of this expression into the energy equation results in an expression for the

SMD or $D_{32}$, after some algebra. This is due to the 2nd- and 3rd-moment terms that appear

in the energy equation.

$$\frac{\sum_i^N p(D_i) D_i^3 \Delta D_i}{\sum_i^N p(D_i) D_i^2 \Delta D_i} = D_{32} = \frac{6\sigma}{\rho_L \left( \frac{u_{inj}^2}{2} - \frac{\bar{u}^2}{2} \right) + \frac{4K}{3} \mu_L \frac{u_{inj}^2 - \bar{u}^2}{u_{inj}} \frac{x}{d_{inj}^2}}$$

As shown in the equation above, the SMD is determined from the surface tension,

liquid density, the viscous dissipation, and the kinetic energy defect in the spray (the

difference in the kinetic energy of the liquid-phase from the injector to the equilibrium

plane). If the kinetic energy of the droplets is small with respect to the injected value,

then SMD is small, and vice versa. That is, if the droplets are moving at high speeds, they

will be doing so in large sizes, as the kinetic energy is not converted to surface tension

energy. In that regard, the estimation of the drop velocity is a critical component in this

framework, as described above. The viscous effect is also included in the SMD equation above, after proper normalization.

We can use the setup described above to examine the effects of velocity on the spray drop size. For example, the SMD equation shows that if there is a large velocity defect then the surface tension energy should be high or the drop size small. We start by examining the trend of the drop size as the drop velocity is varied, and compare with experimental data. There is a set of data taken by Ruff et al.[18] that includes both the drop size and velocity in the dense regions of pressure-atomized sprays. A relatively large-diameter injector, 9.5 mm, were used to inject water into quiescent air at ambient condition, with typical injection velocity of 56.3 m/s. These numbers corresponded to Reynolds number of 534,000 and liquid-phase Weber number of 412,000. The details of the experiment can be found in Ruff et al.[18]. In the data (plotted as dark symbols in Fig. 3.3), it can easily be observed that large droplets are found in the interior of the spray where liquid-phase velocities also tend to be high. The drop velocities decrease as one moves further away from the centerline (Ruff et al. 1991), and so does the drop size. There could be quite complex dynamical processes in the droplets forming from the contiguous liquid core; however, the current integral approach overlooks the detailed mechanisms and only relates the input and output variables. Thus, we may apply a pencil-like control volume originating from the injector toward a particular radial location in the spray, and make use of the SMD equation to relate the drop size with drop velocity, as in Fig. 3.3.  For the constant K, a fixed value of 55,000 appears to give the best results in Fig. 3.3. This is a large number, which either indicates the significance of the viscous dissipation term or that some of the scales in the viscous dissipation term are

underestimated. An alternate interpretation is that if we take the lateral scale, $d_s$, to be of the order of the mean drop size, say 100 µm, then the scaling constant, K, would be 5.5. Thus, SMD itself may be the better length scale to use in assessing the magnitude of the viscous dissipation term. Most of the viscous shear stress is expected to occur at the scales where the drops are torn from the contiguous liquid ligaments. However, this would only alter the numerical value of the constant K, and leave the main results unaffected.
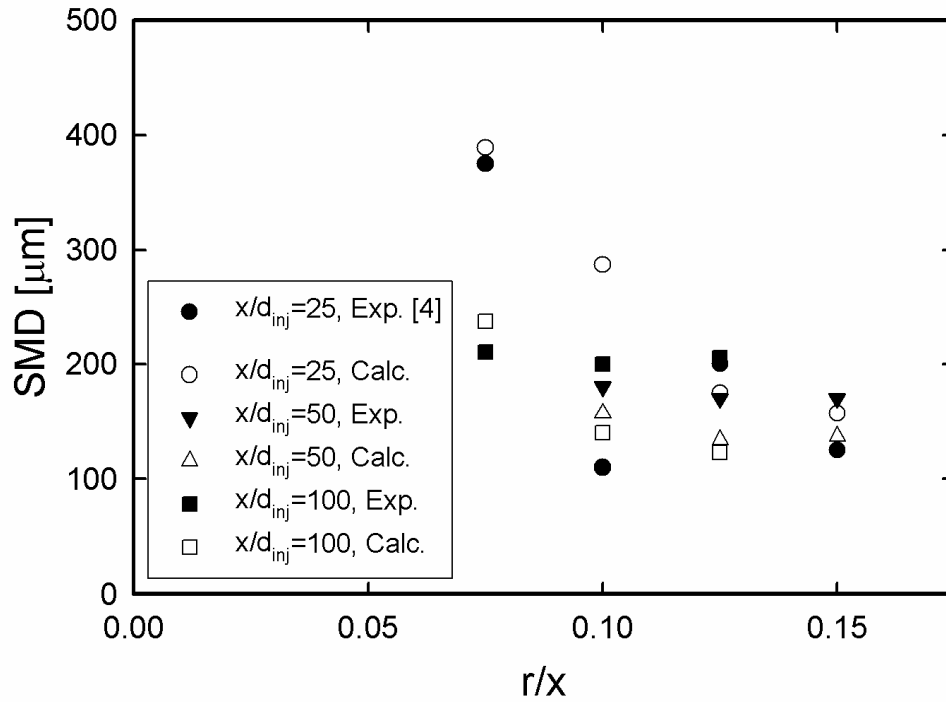


Fig. 3.3. Comparison of the calculated SMD with experimental data

For $x/d_{inj}$ = 25, the agreement between the measured and calculated SMD is quite good, except at r/x of 0.1 at which point the measured SMD is quite small compared to all of the other data points. Overall, the measured SMD's at this axial location show a decrease with increasing radial distance. The data point at r/x=0.1 lies well outside the

trend shown by the other data at $x/d_{inj} = 25$, and is attributed to measurement

uncertainties. At $x/d_{inj} = 50$, there is a gradual decrease in the SMD as one moves

radially outward, with the computed values underestimating the measured ones by 10 to

20 %. The measured SMD stays more or less flat at $x/d_{inj} = 100$ in spite of the fact that

measured drop velocity decreases with increasing radius (Ruff et al. 1991). Since the

drop velocity decreases with increasing radial distance, the computed SMD follows the

same trend. Overall, the trend and values of the SMD are captured well, based on the

energy equation using the measured drop velocities in the calculations. To compute the

SMD using the SMD equation, we only need the drop mean velocity from the data by

Ruff et al.[18], along with fluid parameters such as the surface tension, viscosity. As noted

above, without the viscous dissipation term, the SMD estimates would be very low,

typically 10 μm or less, as all of the lost kinetic energy must appear in the form of surface

tension energy. The viscous term absorbs a good portion of this energy, so that the

resulting drop size are close to observed values.

As shown back in Fig. 3.2, the liquid velocities decay with increasing distance from

the injector. Other injection parameters, such as the spray cone angle, the density ratio,

and the atomization length, also will determine the liquid velocity, and subsequently the

SMD. We can examine the effects of these spray parameters on the SMD. In order to do

so, we first keep the atomization length assumed to be $100d_{inj}$, which is in the range of

typical experimental observations (Lee and Mitrovic 1996). Evidently, if the atomization

lengths were assumed to be at a further downstream location, then the liquid velocities

are smaller (as shown in Fig. 3.2), and therefore so would the SMD be. The SMD

computed in this way are plotted as a function of the density ratio at several spray cone

angles in Fig. 3.4. In Fig. 3.2, when the gas density is large in comparison to the liquid

density, i.e. small $\rho_L/\rho_g$, the liquid velocity is retarded much faster, due to the larger

aerodynamic drag. This is reflected in Fig. 3.4, where smaller drop sizes are observed at

low density ratios. The spray cone angle also affects the SMD, as the liquid velocity

decays faster at larger spray cone angles. However, beyond 45° further changes are

relatively small. If we plot the liquid velocities again at different spray cone angles in Fig.

3.5, we can see that for a factor of two or more increase in the spray cone angle there is

only a modest decrease in the liquid velocity beyond 45°.
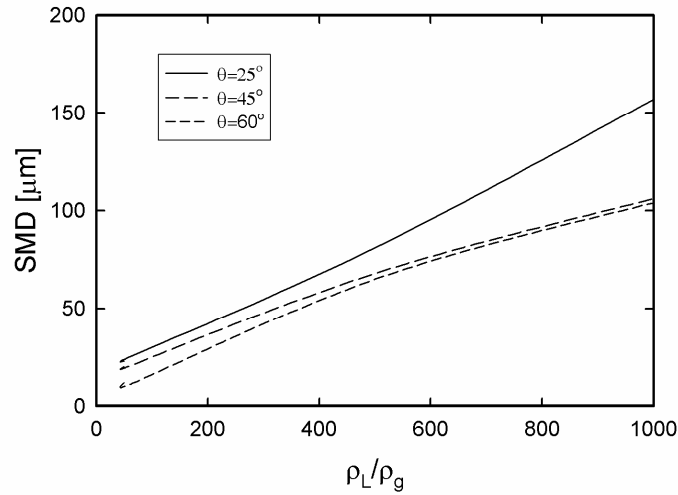


Fig. 3.4. Variations of the SMD with the density ratio
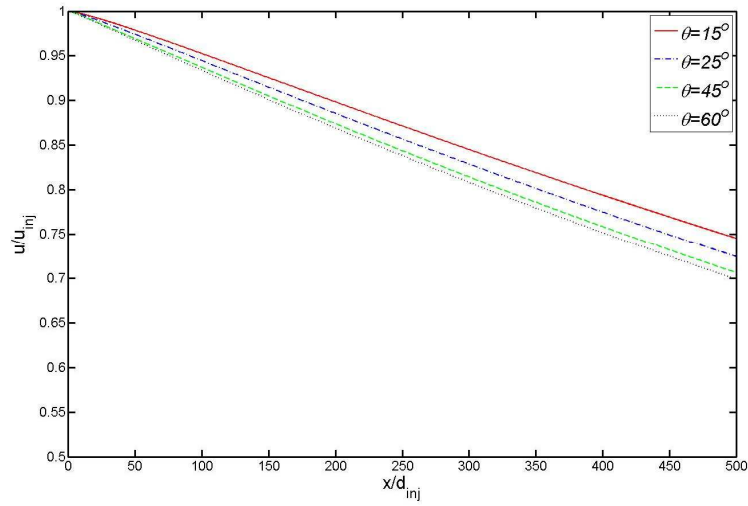
Fig. 3.5. Normailzied liquid-phase velocities, for various injection angles

The effect of the atomization length can also be examined, as in Fig. 3.6. At larger

atomization lengths, the drop velocities are much smaller as shown in Figs. 3.2 and 3.5,

and this is reflected in the smaller SMD's at larger atomization lengths, in Fig. 3.6.

Beyond $x/d_{inj}$ of ca. 200, the SMD levels off, and undergoes relatively small change.

Calculations of the Weber number, using the injector diameter as the length scale, yield a

similar asymptotic behavior. The Weber number approaches an asymptote close to $x/d_{inj}$

of ca. 200, for density ratios above 100. Thus, this length scale is appropriate for

estimation of the atomization length in pressure-atomized sprays.
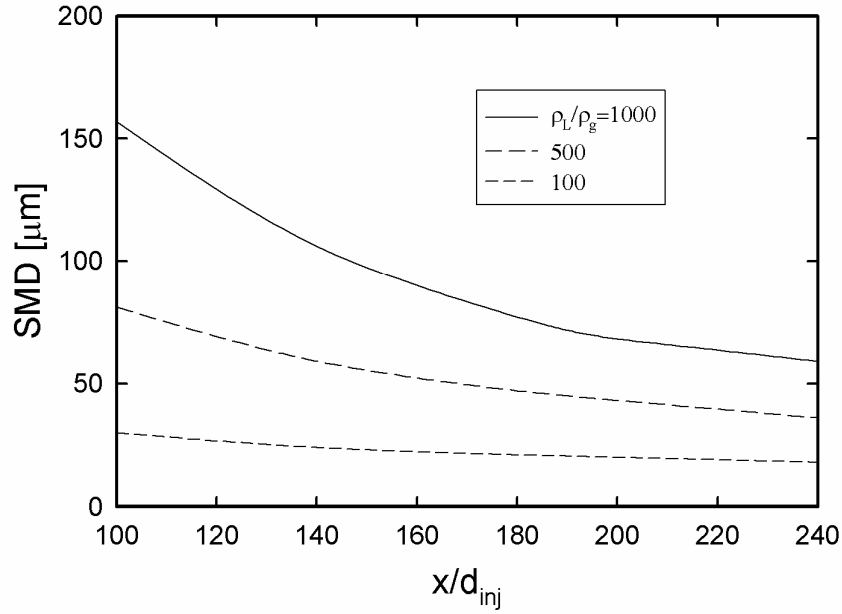
Fig. 3.6. SMD as a function of the atomization length, at various density ratios

## 4. Conclusions

In this work, we have considered an appropriate form of the viscous dissipation term in the integral form of the conservation equation, and examined the effects of momentum terms on the computed drop size. The SMD calculated in this manner agrees quite well with experimental data that included measurements of both the drop velocities and sizes. The revised treatment of liquid momentum, following the work by Rothe and Block[17], also leads to quite stable calculations for a wide range of density ratios. Injection parameters such as the spray cone angle and the atomization length are directly input to the system of equations. Thus, this approach can incorporate various injection parameters into the computations, and can be used for further considerations of the drop and velocity distributions under a wide range of spray geometry and injection conditions.

References

1. Ahmadi, M. and Sellens, R.W. 1993. Simplified maximum entropy based drop size distribution. *Atomization and Sprays*, 3 (3): 291-310.

2. Babinsky, E. and Sojka, P.E. 2002. Modeling drop size distributions. *Progress in Energy and Combustion Science*, 28 (4): 303-329.

3. Cousin, J., Yoon, S.J., and Dumouchel, C. 1996. Coupling of classical linear theory and maximum entropy formalism for prediction of drop size distribution in sprays. *Atomization and Sprays,* 6 (5): 601-622.

4. Dumouchel, C. 2007. A new formulation of the maximum entropy formalism to model liquid spray drop-size distribution. *Particle and Particle Systems Characterization*, 23 (6): 468-479.

5. Dumouchel, C. 2009. The maximum entropy formalism and the prediction of liquid spray drop-size distribution. *Entropy*, 11 (4): 713-747.

6. Dumouchel, C. and Boyaval, S. 1999. Use of the maximum entropy formalism to determine drop size distribution characteristics. *Particle and Particle Systems Characterization*, 16 (4): 177-184.

7. Herrmann, M. 2010. A parallel Eulerian interface tracking_Lagrangian point particle multi-scale coupling procedure. *Journal of Computational Physics*, 229 (3): 745-759.

8. Herrmann, M. 2010. Detailed numerical simulations of the primary atomization of a turbulent liquid jet in crossflow. *Journal of Engineering for Gas Turbines and Power in ASME Transaction*, 132 (6): 061506. 1-10.

9. Herrmann, M., Gorokhovski, M. 2009. A large eddy simulation subgrid model for turbulent phase interface dynamics. *The 11th Triennial Conference on Liquid Atomization and Spray Systems*, in Vail, CO. Paper No. ICLASS2009-205.

10. Lamb,H. 1945. *Hydrodynamics.* New York: Dover Publication.

11 . Lee, T.-W. and Mitrovic, A. 1996. Liquid core structure of pressure-atomized sprays via laser tomographic imaging. *Atomization and Sprays,* 6 (1): 111-126.

12. Lee, T.-W. and Robinson, D. 2011. Calculation of the drop size distribution and velocities from the integral form of the conservation equations. *Combustion Science and Technology,* 183 (3): 271-284.

13. Li, X., Chin, L.P., Tankin, R.S., Jackson, T., Stutrud, J., and Switzer, G. 1991. Comparison between experiments and predictions based on maximum entropy for sprays from a pressure atomizer. *Combustion and Flame*, 86 (1-2): 73-89.

14. Li, X., Tankin, R.S., Sztal, B., and Most, J.-M. 1988. Derivation of droplet size distribution in sprays by using information theory. *Combustion Science and Technology,* 60 (4-6): 345-357.

15. Mugele, R. and Evans, H.D. 1951. Droplet size distribution in sprays. *Industrial and Engineering Chemistry,* 43 (6): 1317-1324.

16. Ritz, R.D. 1987. Modeling atomization processes in high-pressure vaporizing sprays. *Atomisation and Spray Technology,* 3 (4): 309-337.

17. Rothe, P.H. and Blcok, J.A. 1977. Aerodynamic behavior of liquid sprays. *International Journal of Multiphase Flow,* 3 (3): 263-272.

18. Ruff, G.A., Bernal, L.P., and Faeth, G.M. 1991. Structure of the near-injector region of non-evaporating pressure-atomized sprays. *Journal of Propulsion*, 7 (2): 221-230.

19. Sellens, R.W. and Brzustowski, T.A. 1986. A simplified prediction of droplet velocity distributions in a spray. *Combustion and Flame,* 65 (3): 273-279.

20. Sirignano, W.A. and Mehring, C. 2000. Review of theory of distortion and disintegration of liquid streams. *Progress in Energy and Combustion Science,* 26 (4): 609-655.

21. Sovani, S.D., Sojka, P.E., and Sivathanu, Y.R. 2002. Prediction of drop size distributions from first principles: joint PDF effects. *Atomization and Sprays*, 10 (6): 213-222.

22. van der Geld, C.W.M and Vermeer, H. 1994. Prediction of drop size distributions in sprays using the maximum entropy formalism: the effect of satellite formation. *International Journal of Multiphase Flow,* 20 (2): 363-381.

**CHAPTER 4**

**ESTIMATION OF GROUNDWATER ELEVATION**

1. **Introduction**

Water is a necessary and useful resource for human life. Fresh water is central to sustainable development, economic growth, social stability and the alleviation of poverty (Clarke and King 2004). Groundwater is held by underground aquifers, representing almost all fresh water that is not in the form of ice (Clarke and King 2004). In other words, groundwater is commonly understood as the water occupying all of the voids within a geologic stratum.

Groundwater is a scarce and useful resource because only 2.5% of all water resources on Earth are fresh water, and only 30.1% of all of the fresh water resources are in the form of groundwater (Gleick 1993). Desert life in arid states can be maintained through the use of groundwater. Hence, groundwater presents a potential solution to the lack of potable water faced by many regions of the world. For example, without groundwater, Palm Springs, California, would not be a popular leisure destination for golfers (U.S. Geological Service 2005). The area of interest in this work is either arid or semi-arid, in which needs groundwater and encompasses the southwestern states of the United States, such as California (CA), Arizona (AZ), Utah (UT), and Nevada (NV).

Many methods were implemented to estimate groundwater level. Methods include the delaunay polygon, kriging, radial basis function, and inverse distance weighting methods. The main assumption of the aforementioned methods is that groundwater level can be interpolated by a related mechanism.

A delaunay interpolation is used to define regions based on a set of data points in a given plane, such that the regions must be enclosed by a line midway between the measured point under consideration and the surrounding points (Brassel and Reif 2010). In geostatistics, Kriging is an interpolation method for which the interpolated values are modeled by prior covariance, governed by a Gaussian process, commonly known as the best linear unbiased prediction method (Olea 1974). A radial basis function is a real-valued function whose value is dependent only on the distance from the origin (Lin and Chen 2004). Using this function, the sums of radial basis functions are used to approximate given functions, which give interpolated values. Inverse distance weighting is a deterministic multivariate interpolation method that uses a known set of scattered points (Watson and Philip 1985). Other interpolation methods such as the bilinear, nearest-neighbor, and bi-cubic methods can also be used.

The aforementioned traditional methods perform very poorly when sparsity is apparent. Therefore, many researchers look for methods of how one can find a true estimated value without degrading the accuracy.

A novel compressed sensing (CS) algorithm is introduced for an estimation of groundwater level to find a true measurement while reducing data acquisition. Estimated groundwater levels by CS can also help making a visualization of groundwater contour map to monitor trend of groundwater use. CS is a recently developed advanced technology that enables the reconstruction of a signal by using sparsity to solve significantly underdetermined linear algebra problems in broad fields.

The CS technique has several requirements, as described below.

54

- The desired groundwater network database must be compressible, in other words, the database must show the sparsity in the domain. Based on the numerous types of experiments conducted in these regions, groundwater network databases are naturally compressible. When the spatial domain is transferred to the Fourier domain, they also show the transform sparsity.

- The measurement matrices are random matrices, such as a Gaussian, Bernoulli, or more generally any sub-Gaussian distribution that is known to satisfy the restricted isometry property (explained in Section 3) with high probability.

- The l1-optimization algorithm, also known as the basis pursuit algorithm, is mainly used. An alternate recovery model known as Total Variation (TV) can be applied. The TV model uses gradient sparsity in the spatial domain.

This scheme is entirely new and can also be used for analog 2-Dimensional (2-D) data recovery. Originally, the CS measures the signal via on-line sensing devices and then, signals are recovered afterwards by off-line. Because a groundwater network has not been established by online sensing devices, which are not typically interconnected with the same data acquisition board, instead the accessible groundwater data for a certain time period and within certain registered wells are gathered and pre-processed for an appropriate use. Therefore, on-line measurements of groundwater network data remain unexplored. Hence, for this work, after the groundwater network data are set up, the recovery method written above is applied to solve the convex optimization problem.

Groundwater retrievals via the National Aeronautics and Space Administration (NASA) data are explained in two ways in Section 2 to compare our results and eventually validate our suggested method. In Section 3, CS algorithm, materials, computational methods are described. The sparse representation of the groundwater network is shown; the detailed steps used to acquire groundwater level data from various sources are explained; and the algorithmic flow is provided. Results are shown and discussion is followed in Section 4. Finally, the conclusions of this work are drawn in Section 5.

## 2. Groundwater Retrieval

Two groundwater retrieval methods via NASA data will be explained in this section. One is wetness percentile and the other is groundwater budget.

The National Drought Mitigation Center at the University of Nebraska-Lincoln, as part of the NASA data assimilation, provides wetness percentile on a weekly basis. It is defined as the percentage of days within a one-month window of the current day of the year that were drier than the current value at the same location during the period 1948 to present. In other words, the groundwater wetness percentile represents the percentile of the time, for a given location and time-of-year, that the groundwater storage level was lower than that of the current time. For example, a wetness percentile of 10 means that for only 10% of the time, is groundwater storage level is lower than the current level for that particular location and time of the year.

The construction of the wetness percentile for a given location and time of the year is related to complex procedures with several NASA data components. Briefly, total water

storage consists of surface water storage and groundwater storage. Using NASA Gravity

Recovery And Climate Experiment (GRACE) data, total water storage can be obtained.

By NASA Global Land Data Assimilation System (GLDAS) land surface models (LSMs),

total amounts of surface water storage can be calculated. The amount of groundwater

storage can be estimated by subtracting total amounts of surface water storage from total

water storage. Historical data of groundwater storage in NASA database range from 1948

to present. The location of current groundwater storage can be picked in the cumulative

density function (CDF) of groundwater storage database on a specific location.

NASA GRACE satellites measure the time-variable gravity field of the Earth. Low

Earth Orbit (LEO) satellites orbit the Earth on the same path, separated from each other

by a given distance, allowing the relative position of a pair to be accurately determined.

The GRACE outcome is a set of fully normalized spherical harmonics coefficients, $C_{lm}$

and $S_{lm}$, with degree l and order m up to 96. Therefore, the Terrestrial Water Storage

(TWS) anomalies can be directly estimated by gravity coefficient anomalies, $\Delta C_{lm}$ and

$\Delta S_{lm}$, for each month (Swenson and Wahr 2002), as written below.

$$\Delta\eta_{land}(\theta,\phi,t)= \frac{a\rho_{avg}}{3\rho_{water}} \sum_{l=0}^{\infty} \sum_{m=0}^{l} \tilde{P}_{lm}(\cos\theta) \frac{2l+1}{1+k_l} (\Delta C_{lm}\cos(m\phi) +\Delta S_{lm}\sin(m\phi))$$

where $\theta$ is the polar distance, $\phi$ is the longitude, a is the equatorial radius of the Earth,

$\rho_{avg}$ is the average density of the Earth, $\rho_{water}$ is the density of fresh water, $\tilde{P}_{lm}$ is the fully

normalized Legendre associated function of degree l and order m, and $k_l$ is the Love

number of degree l (Han and Wahr 1995).

At high degrees and orders, spherical harmonic coefficients are degraded due to noises and various errors. Gaussian filters and de-stripping filters are usually applied to minimize the effect of errors.

The TWS anomaly is the change of the total water storage amount in the vertical column from the groundwater to surface water at a specific location. Once the TWS is established on the Earth, four GLDAS LSMs such as the Community Land Model (CLM), the Variable Infiltration Capacity (VIC), Mosaic, and Noah simulate the Earth surface water and groundwater flows in a sophisticated way by interacting with several forcing variables and multiple sources of observational data from the various climate monitoring institutions.

From the simulation results presented by the LSMs, the amount of variation in terms of the surface water and groundwater can be made. In particular, the surface water runoff, storm surface water runoff, base groundwater runoff, precipitation, soil moisture, snow water equivalent, evaporation, and evapotranspiration are discretely evaluated and made publicly available. As a result, groundwater storage can be calculated by subtracting the total GLDAS land surface water storage from the TWS.

Based on the computed data for the changes in groundwater amount and the historical database of changes in groundwater storage, a CDF of the groundwater storage changes from the entire time series from 1948 to the present for the same month of the year can be created. A CDF is a benchmark of the relative location of the current groundwater storage change based on time-series data. Then, for any change in groundwater storage, the wetness percentile can be estimated correctly. NASA has published the wetness

58

percentile data since August 2002. This is currently used to give a good indication of the frequency of drought conditions.

To develop percentile data from our groundwater level data, groundwater network data from January 1942 to December 2014 were used. For a comparison with the wetness percentile, two spatial resolutions (0.25 by 0.25 degree and 1 by 1 degree) with yearly temporal resolution were used to build groundwater level percentile. First, the groundwater level percentile in 2002 is initiated because NASA has published the wetness percentile data since August 2002. A time-series of groundwater network data is generated to make a CDF of groundwater level over the periods of interest, and then the yearly measurement of groundwater level for a specific year is used to determine the groundwater level percentile. The groundwater level percentile data span from 2002 to 2014.

Because the yearly groundwater level percentiles were constructed due to intermittent measurements of groundwater level data, the wetness percentiles given by NASA were converted to yearly averaged wetness percentiles as well. These values are then compared with the groundwater level percentile. We call the groundwater level percentile as groundwater percentile in this study.

Secondly, for derivation of groundwater budget, GLDAS LSMs data are used. Groundwater budget can be defined in a sentence as the variation in groundwater elevation is equal to the variation in the difference between the recharge amount and consumption amount.

Scientists at the National Oceanic and Atmospheric Administration (NOAA) National Centers for Environmental Prediction (NCEP) and the NASA Goddard Space Flight

Center (GSFC) jointly developed the GLDAS for a prediction of weather and climate change. In this work, water contents in terms of vertical columns from ground to atmosphere can be found in the products from GLDAS.

GLDAS uses a variety of satellite observation data and conventional observation data in simulation routines. Satellite data from the Advanced Very High Resolution Radiometer (AVHRR) are used for the land cover class (surface fields of vegetation greenness and its seasonality) (Hansen et al. 2000), data from the Advanced Microwave Scanning Radiometer (AMSR) are used for soil moisture fields (Mahrt and Pan 1984; Reynolds et al. 2000), data from the Television Infrared Observation Satellite (TIROS) Operational Vertical Sounder (TOVS) are used for temperature (Ottle and Vidalmadjar 1992), the Moderate Resolution Imaging Spectroradiometer (MODIS) is used for real-time snow cover (Rodell et al. 2002), data from the Special Sensor Microwave/Imager (SSM/I), NASA-NASDA's Tropical Rainfall Measuring Mission (TRMM), the Advanced Microwave Sounding Unit (AMSU) are used for real-time precipitation (Atlas and Lucchesi 2000; Klinker et al. 2000; Turk et al. 2000;Huffman et al. 2003). Observational data from hourly 24-km World Wide Merged Cloud Analysis (WWMCA) and the Air Force Weather Agency's (AFWA) Agricultural Meteorology modeling system (AGRMET) (Kopp and Keiss 1996) are used for solar radiation (Hamill et al. 1992; Shapiro 1987; Idso 1981).

Both satellite data and conventional data are used to derive either an important factor or to correct important parameters and forcing model outputs in various steps while the LSM runs. In GLDAS, surface runoff is determined by the simple water balance model (Schaake et al. 1996), using a devised probabilistic model in upper layer and bottom layer

to predict runoffs. Evaporation is derived from the Penman potential evaporation (Mahrt and Ek 1984). The prognostic equations for non-dimensional volumetric water content predict the soil moisture state variables (Mahrt and Pan 1984). Other values such as the soil temperature, snowpack depth, snowpack water equivalent, surface water content, the energy flux and water flux terms of the surface energy balance and surface water balance are estimated as GLDAS outputs (Rodell et al. 2004).

The Noah LSM is used in this paper because it only provides fine grid (0.25 by 0.25) outputs. In the Noah data, the hydrological cycle elements such as evaporation, surface runoff, base groundwater runoff, storm runoff, snow content and moisture content in the subsurface layers of the Earth were pulled and processed for comparison with the suggested method in this paper.

The hydrological budget equation is written below,

$$\Delta GW_{budget} = \Delta Q_s + \Delta Q_{storm} + \Delta Q_{base\ GW} + \Delta M + \Delta S - \Delta E$$

where $\Delta GW_{budget}$ is the groundwater budget, $\Delta Q_s$ is the surface runoff, $\Delta Q_{storm}$ is the storm runoff, $\Delta Q_{base\ GW}$ is the base groundwater runoff, $\Delta M$ is the moisture content, $\Delta S$ is the snow content, and $\Delta E$ is the evaporation. The base grid from the Goddard Earth Sciences Data and Information Services Center (GES DISC) and NASA Earth Observatory is 0.25 degree in both latitude and longitude. The Noah data span from March 2000 to November 2014, allowing for the construction of a yearly averaged groundwater budget.

Initially, all units mentioned above are given in $kg/m^2$. For comparison with total rainfall in feet and groundwater elevation in feet, the values are divided by water density

at 4 degrees Celsius. Therefore, the groundwater budget unit is the meter. It is converted to feet by conversion factor 3.28084.

## 3.  Algorithm, Materials and Methods

A compressible signal is a signal that can be sparsely represented in a proper basis. According to CS, compressible signals can be perfectly recovered from far fewer samples than the number required by the Nyquist theorem, which specifies that one must sample at least two times faster than the signal bandwidth.

Using groundwater network data, the construction of compressible signal network data is first illustrated, and then the modeling approach for an l1-optimization based on the groundwater network databases is shown.

First, we suppose that the network data are composed of a matrix of size N by 1, in which N nodes are elements of the network data. Each node acquires a sample $x_i$, which is the ensemble averaged groundwater level at the specified coordinate ranges on Earth. The first goal when using the groundwater network data is to collect the vector $\mathbf{x}$ $=[x_1,\ldots,x_n]^T$. We set $\mathbf{x}$ as an m-sparse representation if a proper basis $\Psi=[\Psi_1,\ldots,\Psi_n]^T$ can be found and it meets the condition of $\mathbf{x}=\sum z_i\Psi_i$, where i=1 to m as well as m≪n.

The Null Space Properties (NSP) states that only an m-sparse vector is guaranteed in the null space $\Psi$ whose $z_i$ =0. Restricted Isometry Properties (RIP) guarantees that matrix $\Psi$ preserves the distance between any pair of m-sparse vectors and ensures that they remain nearly orthonormal (Eldar and Kutyniok 2012). When these conditions are

62

satisfied, we can collect the sample $\mathbf{y}=\mathbf{\Phi x}$, where $\mathbf{\Phi}$ is a size K by N sensing matrix whose element $\Phi_{j,i}$ is a set of independently and identically distributed random variables with variance 1/k. In most cases, its element is a zero-mean random variable. Consequently, we can recover $\mathbf{x}$ from $\mathbf{y}$ by solving a linear programming problem formulated as below.

Min $\|\mathbf{x}\|_1$ such that $\mathbf{y}=\mathbf{\Phi\Psi z}$.

where matrix $\mathbf{\Phi}$ satisfies an RIP with (m, δ) for δ∈ (0, 1) if $(1-\delta)\|x\|_2^2 \leq \|\Phi x\|_2^2 \leq (1+\delta)\|x\|_2^2$.

One specific condition for RIP is defined as m=2K and $\delta<\sqrt{2}-1$. Random matrices such as a Gaussian, Bernoulli, or more generally any sub-Gaussian distribution are known to satisfy the RIP with high probability. The related condition, which is referred to as incoherence, requires that the rows of matrix $\mathbf{\Phi}$ cannot sparsely represent the columns of matrix $\mathbf{\Psi}$ (Baraniuk 2007). The condition that guarantees the accuracy of the recovery results is given by k≥C·m·log(n), where C is a small constant. As suggested by the four-to-one practical rule (Donoho 2006), m=4k is generally sufficient. The requirement of compressed sensing means that a sensor measures samples y=Φx, where y is a length M vector, and satisfies K<M≪N, such that one can reconstruct the original data from far fewer samples K≈M≪N than the traditional sampling method.

Most groundwater network data problems are solved in the spatial domain. In cases in which the transform sparsity must be applied, 2-D groundwater network data $f(t_x,t_y)$ from samples F(x,y) of the discrete Fourier transform on a radial domain Θ are constructed. Furthermore, the 2-D Fourier transform is formulated below.

$$F(x,y)=\sum_{t_x=0}^{N-1}\sum_{t_y=0}^{N-1}f(t_x,t_y)e^{-2\pi i\left(t_x\frac{x}{N}+t_y\frac{y}{N}\right)}$$

where $f(t_x,t_y)$ is the 2-D groundwater network data set, and $F(x,y)|_\Theta$ are samples on the domain $\Theta$.

For a better understanding of the idea of CS, an example is shown in Fig. 4.1 for a brain CT scan. The image size is 256 by 256. The total pixel count is 65,536. Two reconstructed examples are shown in Figs. 4.2 and 4.3: the former reconstruction was obtained with a low sampling rate, and the latter, with a high sampling rate.

The right side of Fig. 4.2 shows the recovered brain CT obtained by solving the l1-optimization after gathering 2,025 sample pixels. This approach uses 22 radial lines for sampling, as shown on the left side of Fig. 4.3. Obvious deviations in comparison with the original brain CT can be observed. For measurement errors between the original and the reconstructed image, the 2$^{\text{nd}}$ norm is used, which is denoted as below.

$$\sqrt{\sum\left(x_{ij}-\bar{x}_{ij}\right)^2}\ \text{ for all i,j} \in (1,n)$$

The mean of percent deviation is denoted as below.

$$\sum\left(\left|\frac{x_{ij}-\bar{x}_{ij}}{x_{ij}}\right|/n^2\right).$$

Its error is 2956 (42% by mean of percent deviation). Note that at the Nyquist sampling rate is $2\pi/N$ (0.0087 Hz). However, in this low sampling rate case, the sampling rate is $\pi/22$ (0.1428 Hz). Few samples are collected, causing the reconstruction of the original image to fail.

When the sampling rate is increased to $\pi/90$ (0.0349 Hz), the reconstructed brain CT on the right side of Fig. 4.3 is successfully recovered. The total count of sampled pixels

in Fig. 4.3 is only 12,479 of 65,536, or approximately 19%. The error in this case is 386 (12% by mean of percent deviation).
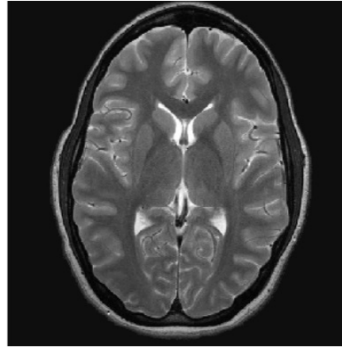


Figure 4.1. Original brain CT
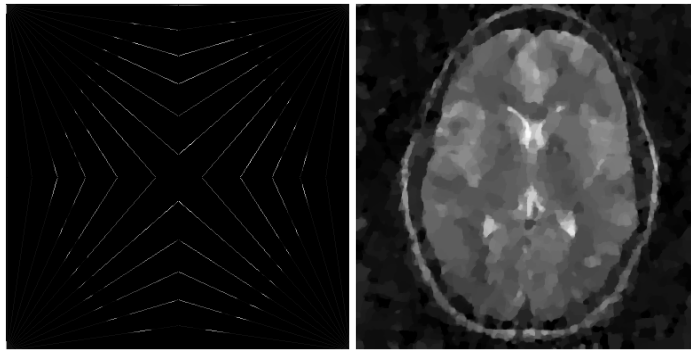


Figure 4.2. Recovered brain CT (right) based on a low sampling rate (the white dots are sampled on the left)
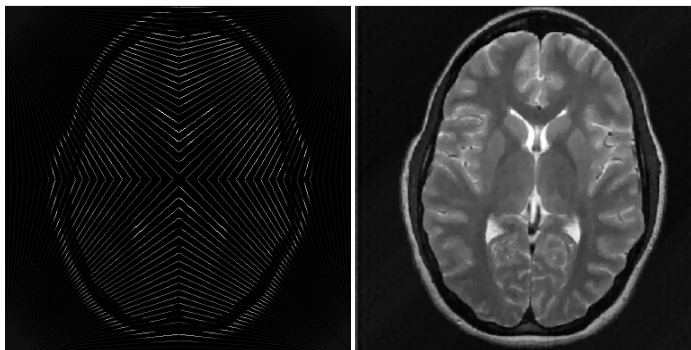


Figure 4.3. Recovered brain CT (right) based on a high sampling rate (the white dots are sampled on the left)

In these examples, which utilize sufficiently smaller sampling rates than the Nyquist rate, CS enables incomplete measurements to be reconstructed.

For the application of CS to groundwater network data, the sparsity of the constructed groundwater network data must first be verified. The successful reconstruction of original data from smaller measurements should be checked, accordingly. The exact and unique reconstruction can be obtained by using a measurement process that satisfies RIP and incoherence in most cases. As the incoherence of the measurement matrix in the sparse basis increases, fewer measurements are needed.

In this paper, measurements of the groundwater network data are regarded as analog numeric data with a different time frame at each point of measurement. This is similar to treating the approach as a geological measurement type for K-sparse compressible measurements. l1-optimization is used for compressible groundwater network data. A generic measurement matrix is considered first. Many other formulations can be achieved because the measurement itself can contain errors, and the same problem can be cast with different selectors for the statistical estimation.

Note that many other sparse transforms, such as the discrete cosine transform, discrete curvelet transform, and discrete wavelet transform, can be applied to the measurement of compressible groundwater network data. For a detailed review of and further assistance with CS theory, please refer to these papers (Elad 2010;Elda and Kutyniok 2012;Yin et al. 2008;Elad et al. 2005;Stojnic 2010;Takhar et al. 2006;Duarte and Elda 2011;Donoho 2006;Candes et al. 2006;DeVore 2007).

Groundwater data pre-processing, groundwater data network construction, and the computational methods are described below.

66

To obtain groundwater level measurements, the sensing modality is either a pressure transducer fitted with a data logger or a floating device fitted with a roller in a rail that is pulled by a counter weight on the opposite end as the water head fluctuates within the registered well (Cunningham 2014).

In each registered well, the depth-to-well (or the water head) is measured by the hydrostatic pressure change calibrated by the reference point or the displacement measured by the rolling distance of the wheel, which is sensed by an odometer (Cunningham 2014). The measurements used in this work were made by the USGS Groundwater Data Watch for Nations, whereas other data were derived from databases in each state's water department and consist of data from multiple sensor data collecting platforms. These platforms collect the data and then send the data to the data logger on the site, which then transmits the information through satellite networking or land lines; ultimately, all of the data are collected at ground receiver station. Furthermore, it is worth noting that some wells have been measured manually by the USGS and the state's water department.

The measured groundwater data at the wells consist of the depth-to-well by date and the elevation. A depth-to-well is the measurement of the height of water relative to the well hole. This measurement is a benchmark that enables us to monitor any changes in the storage of groundwater. Elevation is the vertical datum used to describe the well location, taking the sea surface level as the reference point. Note that NGVD29 (National Geodetic Vertical Datum of 1929), NAVD88 (National Geodetic Vertical Datum of 1988), or NED (National Elevation Dataset) values are used. The elevation allows

measurements of the depth-to-well to be represented with respect to the sea surface level for the gathered well databases.

In this paper, the term called groundwater elevation is used for the calculated depth-to-well with respect to sea surface level. Groundwater elevation can be obtained by subtracting the depth-to-well from the elevation of the well location. It produces information which is comparable with the data for other wells within the areas of interest.

A groundwater network map can be established by gathering all of the information for the registered wells. To collect the groundwater data, we used the USGS and the state-managed water department sites  shown in Figs. 4.4 and 4.5, respectively since USGS and the state water department monitor wells, in addition to providing a historical database. The groundwater elevations can be plotted in a 2-D gridded plane by longitudinal and latitudinal degrees, according to a predetermined grid size, for example, 0.25° by 0.25°.
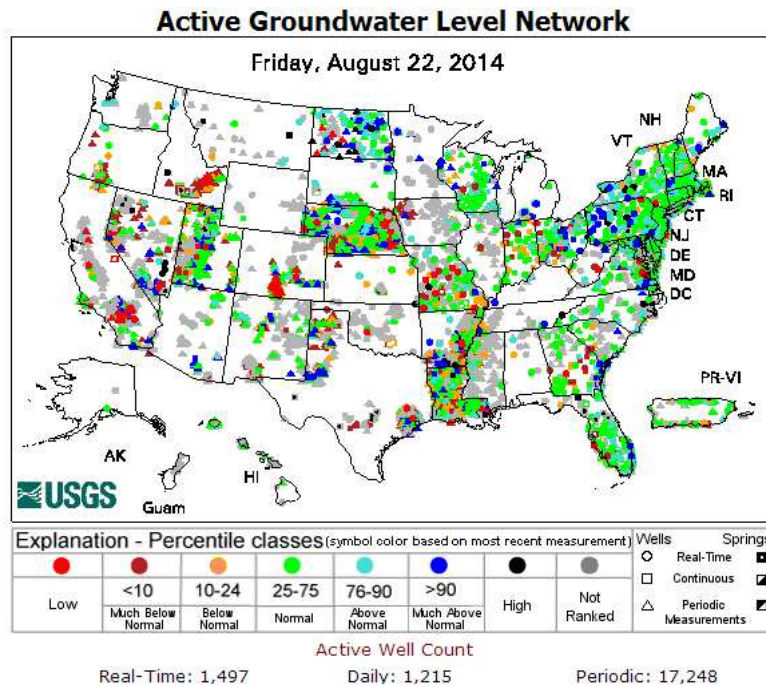
Figure 4.4. USGS Groundwater Watch Site (Circle, Square, and Triangle represent the monitored sites); http://groundwaterwatch.usgs.gov/default.asp
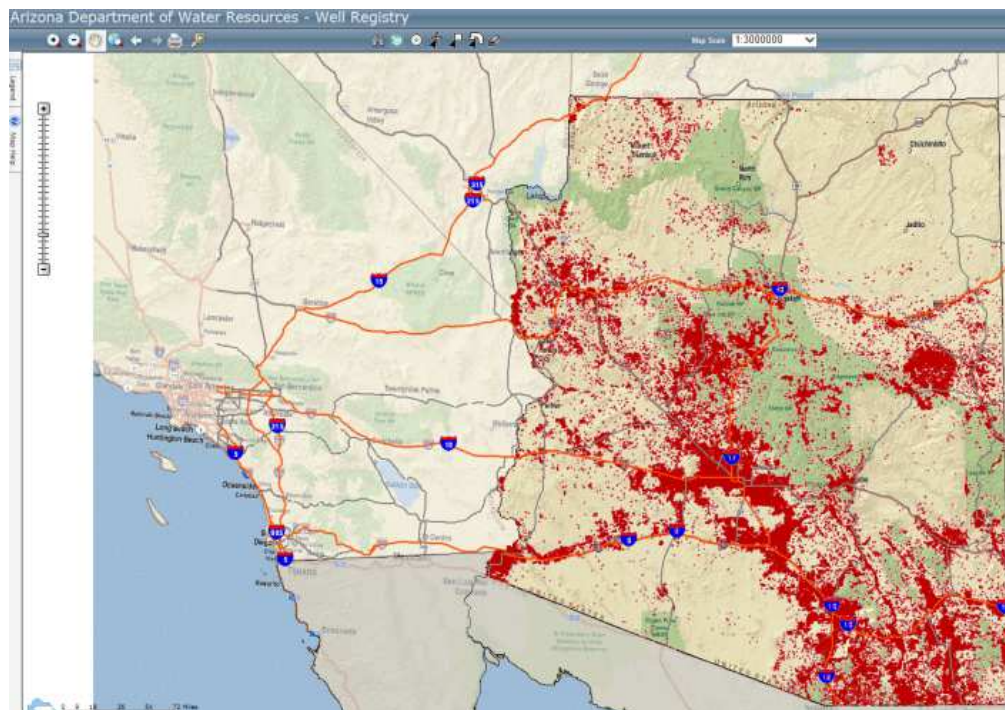


Figure 4.5. Arizona Groundwater Watch Site (Red dots represent the registered wells in the highlighted region); https://gisweb.azwater.gov/WellRegistry/Default.aspx

After the groundwater data network was built from data sources originating from the USGS, Arizona Department of Water Resources (ADWR), California Department of Water Resources (CDWR), Nevada Department of Water Resources (NDWR), and Utah Department of Water Resources (UDWR), each row in the database contains a latitudinal degree, a longitudinal degree, ground elevation, record year, record month, and record day such as [36.1675, -119.3569, 169, 2010, 8, 18]. For example, the GWSI site ID 361003119212501 is located at (36.1675, -119.3569), its ground elevation is 169 feet, and it was recorded on 8/18/2010. This format is used throughout the computations in this work.

For the areas of interest, a latitudinal degree ranges from 31.125 to 42.125, and a longitudinal degree falls within -124.375 to -109.125. Based on the pre-set degree above, all of the data were fit to the same grid system, such as 0.25 by 0.25 degree or 1 by 1 degree, to build the groundwater network data construction. Additional values in unverified areas in the groundwater network were obtained by Delaunay method. Due to the intermittence of the measured groundwater data, a yearly comparison of the data is assessed instead of a monthly data comparison.

In each run of the l1-optimization procedure, a sampling rate $\alpha$ must be varied. At the end of each run, important variables are stored in the groundwater network database (GNDB). These variables include the total sampling rate, compression rate, original groundwater network data, recovered groundwater network data, error ($2^{nd}$ norm), and total computation time. The initial sampling rate is 90%. Based on extensive trial and error, a sampling rate $\alpha$ was determined.

Using the data in the GNDB, three samples are chosen as the sparsest, the intermediate, and the densest, respectively, according to the cardinality (total number of nonzero elements in the data) of the given network data. A pilot run is performed from the highest sampling rate to the lowest sampling rate in each category, while tracking key performance indices. Based on the pilot test results, a minimum sampling rate is chosen, as well as a minimum error, denoted by $\delta$. These two parameters are used to terminate the l1-optimization loop.

Immediately after the termination criterion mentioned in the previous step has been met, the integrity of the groundwater network data is assessed. Once the integrity has been assured, then all procedures are finished. A primal-dual algorithm for linear programming is used to reconstruct the groundwater data, and l1-magic embedded in Matlab is used. Detailed step-by-step procedures (Boyd and Vandenberghe 2004; Candes et al. 2006) are explained in Appendixes A and B. A flowchart is shown below, in Fig. 4.6.

```
        ┌─────────────────┐
        │ Data Acquisition │
        └────────┬────────┘
                 │
                 ▼
        ┌─────────────────┐
        │ Data Pre-Processing │
        └────────┬────────┘
                 │
                 ▼
        ┌─────────────────┐
        │  Groundwater Data │
        │  Network Buildup  │
        └────────┬────────┘
                 │
                 ▼
        ┌─────────────────┐
   ┌───▶│  l1-optimization │
   │    └────────┬────────┘
   │             │
   │             ▼
   │         ◇ δ ≥ Error ◇
   │  N                       Yes
   └───                        │
                               ▼
                     ┌─────────────────┐
                     │ Store Data in DB │
                     └────────┬────────┘
                              │
                              ▼
                         (  End  )
```
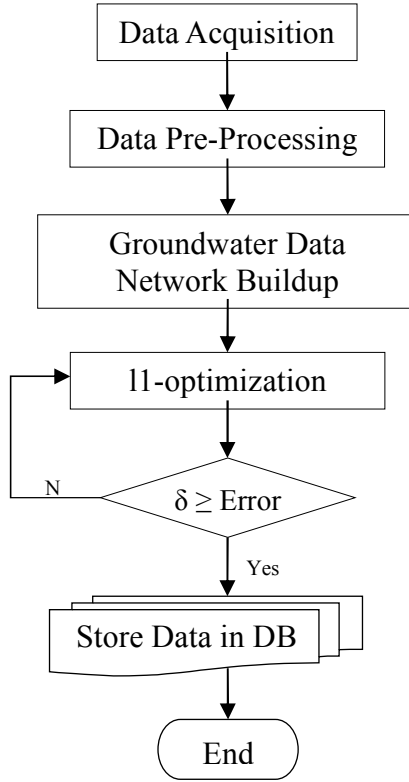
Figure 4.6. A flow chart depicting the algorithm used in this work

## 4. Results and Discussion

The validity of the application of the l1-optimization approach to groundwater elevation estimation must be proved through the aforementioned methods in Sections 2.

Before these methods are proved, we use a self-validation method to prove our suggested method. To do so, several point measurements are excluded from the original data. The questions are 1) whether l1-optimization can construct the excluded point measurements, 2) what the minimum sampling rate must be for the optimization to accomplish the construction, and then, 3) how the method functions once the maximum sampling rate has been chosen.

A total of 26 point measurements (5 to 7 point measurements per state, apart from each point) are selected randomly for the southwestern US and are shown in Fig. 4.7. The red asterisks represent the excluded point measurements, and the black dots show the state boundaries. If the selected point measurement site falls within a city boundary, the city name is written near the red asterisk in Fig. 4.7. If the point is simply near a road or does not fall close to the city boundary, then no annotations are provided. When the l1-optimization was applied, those points had been purposefully eliminated so that the compressibility of the groundwater network data and the accuracy of the l1-optimization could be checked by comparing the reconstructed data with the original data. The groundwater network data in 2004 among the GNDB were chosen.
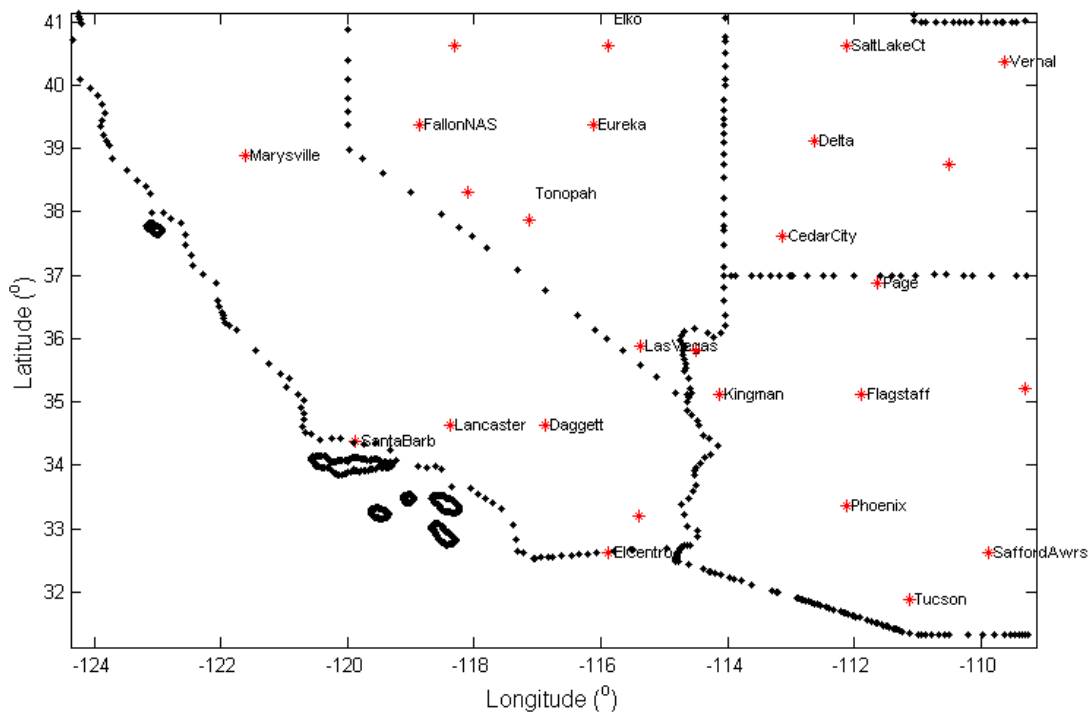


Figure 4.7. The selected set of 26 point measurement locations in the southwestern US

For the three sampling rates, validation line plots are given on the right-hand-side of Figs. 4.8-10. At a poor sampling rate (32 %), which cannot ensure the reasonable maximum error δ (here, 1.00), the original groundwater network, reconstructed groundwater network, and comparison line plot between the original data and reconstructed data are plotted in Figs. 4.8 for the selected points. The left-hand-side depicts an original groundwater network from 2004. The black dots represent the state boundaries. The black inverted triangles show the eliminated cities, and black diamonds denote the unnamed point measurements. The middle figure presents the reconstructed data. The l1-optimization fails to reconstruct the original data. If the optimization had succeeded, this figure would appear identical to the left-hand-side figure. The validation line plot shows disagreements between the original data point and the reconstructed data. Only one point measurement is exactly reconstructed among the 26 points. The error is considerable.
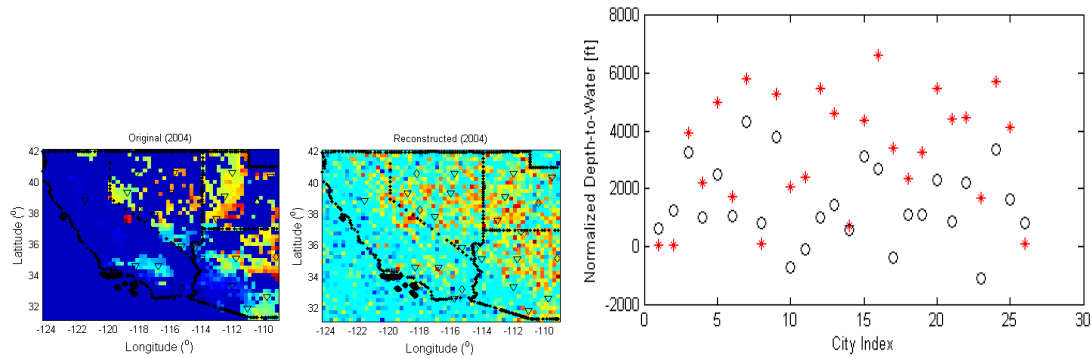


Figure 4.8. Validation based on a 32 % sampling rate for the groundwater network of the southwestern US, 2004 (Black circles denote original values and red asterisks represent reconstructed values)

At a proper sampling rate (59 %), the reconstructed plot precisely depicts the original plot in Fig. 4.9. In the validation line plot, the successful reconstruction of the excluded points is shown.

74
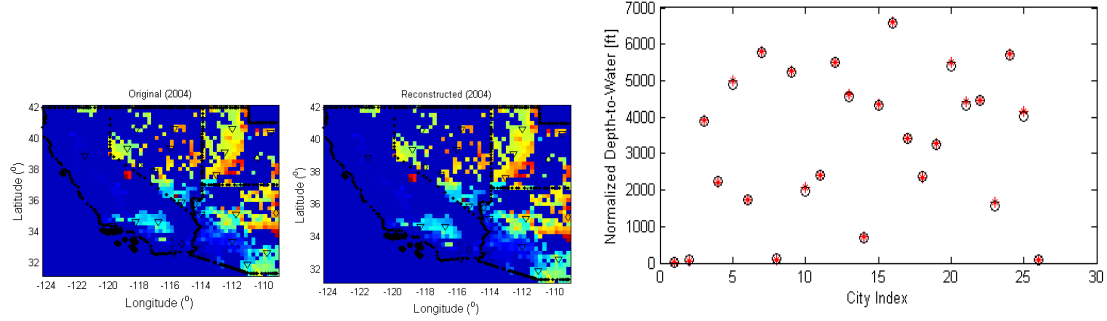
Figure 4.9. Validation based on a 59 % sampling rate for the groundwater network of the southwestern US, 2004 (Black circles denote original values and red asterisks represent reconstructed values)

At a maximum sampling rate, the reconstructed plot looks exactly like the original given in the validation plot of Fig. 4.10. The l1-optimization reconstructs the sparse data very well, and the expanded values in the reconstruction procedure are obtained with 100% measurement accuracy. Through this successful self-validation method, the existence and uniqueness of compressibility in the groundwater network data is proven, a minimum sampling rate is selected, and the algorithmic characteristics for the chosen maximum sampling rate are observed.
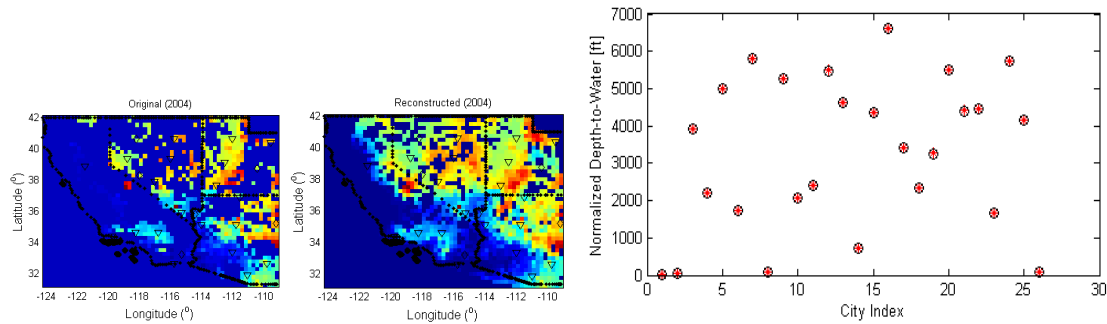


Figure 4.10. Validation based on a 100 % sampling rate for the groundwater network of the southwestern US, 2004 (Black circles denote original values and red asterisks represent reconstructed values)

For a more clear visualization of the original groundwater network data for 2004 as presented in Fig. 4.10, an enlarged figure with a color bar is presented in Fig. 4. 11. This contains 743 point measurements on 62 by 45 gridded planes.

75
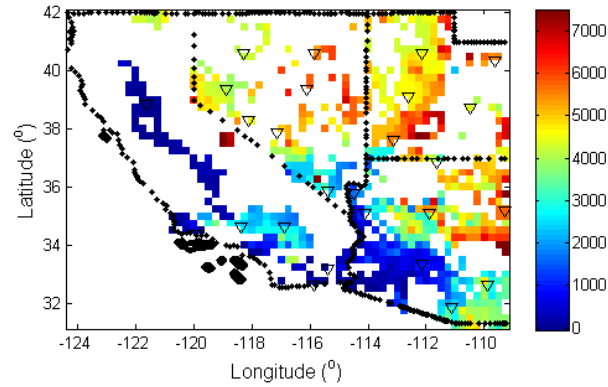
Figure 4.11. Original groundwater network in the southwestern US, 2004 (Inverted triangles represent the selected 26 cities)

An enlarged view of the reconstructed groundwater network data based on the 100% sampling rate in 2004 is shown in Fig. 4.12. In Fig. 4.11, if no point measurements of groundwater elevation were recorded, the corresponding point value is 0, displayed in white based on the conversion to a value indicating not-a-number; this was done intentionally to contrast the measured points with other non-measured sites. By contrast, after performing the l1-optimization reconstruction, values of zero are scarce because the approach outputs small fractional values for the non-measured sites instead of 0.
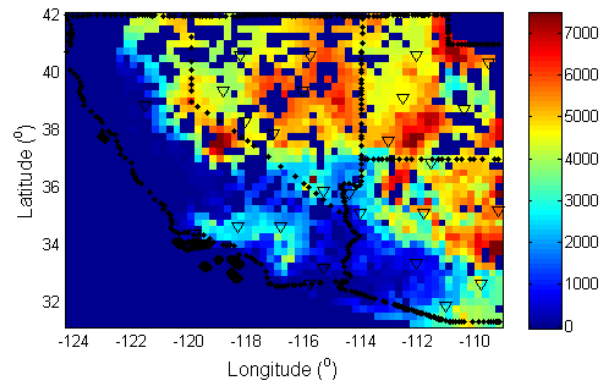


Figure 4.12. Reconstructed groundwater network in the southwestern US, 2004 (Inverted triangles represent the selected 26 cities)

A magnified view of the original groundwater network in the state of Arizona in 2004 is shown in Fig. 4.13. Seven cities are represented by inverted triangles. The cities are

76

Phoenix, Tucson, Flagstaff, Page, Kingman, Safford, and somewhere in the vicinity of St. Johns.
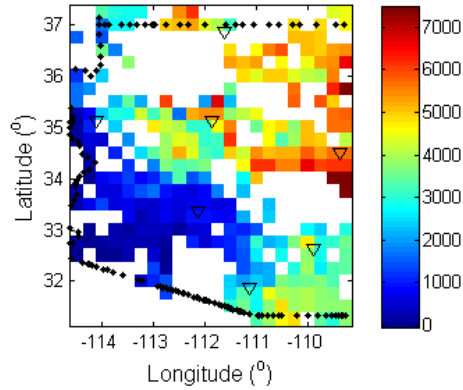


Figure 4.13. Magnified original groundwater network in the state of Arizona, 2004

A magnified view of the reconstructed groundwater network in the state of Arizona in 2004 is shown in Fig. 4.14. In this magnified figure, the reconstruction augmented the point measurements. A maximum absolute deviation, defined by $\left|x_{ij}-\bar{x}_{ij}\right|$, applied only on the measurement point is approximately 1. We can say that the reconstructed groundwater network is exactly the same as the original groundwater network.
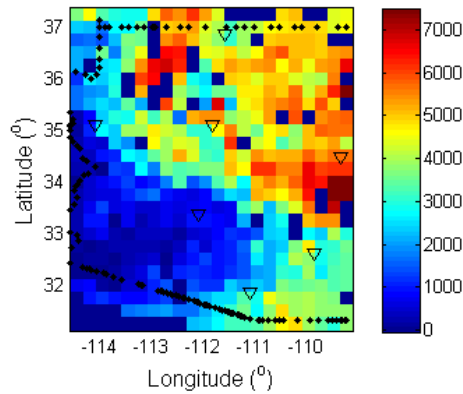


Figure 4.14. Magnified reconstructed groundwater network in the state of Arizona, 2004

By increasing the spatial resolution from 0.25 to 0.1 degree while constructing the groundwater network, the groundwater network data from 2004 can be plotted on 128 by

128 gridded planes in Fig. 4.15. The sparsity of the measurements is more noticeable than before, as the spatial resolution of the data increases.
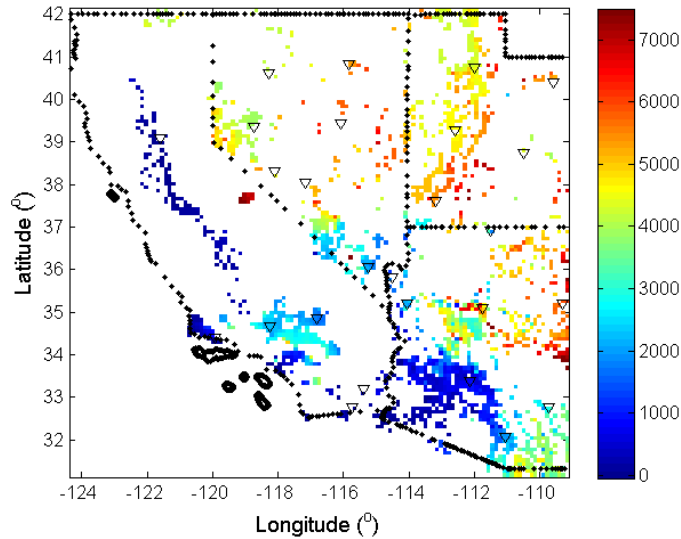


Figure 4.15. Original groundwater network in the southwestern US, 2004

The reconstructed groundwater network is shown in Fig. 4.16. This reconstruction depicts an exact match between the measured sites and expanded values for the overall gridded planes. In comparison with Fig. 4.12, many spots still are filled with small fractional numbers due to the high spatial resolution, which places a significant computational burden on the l1-optimization.
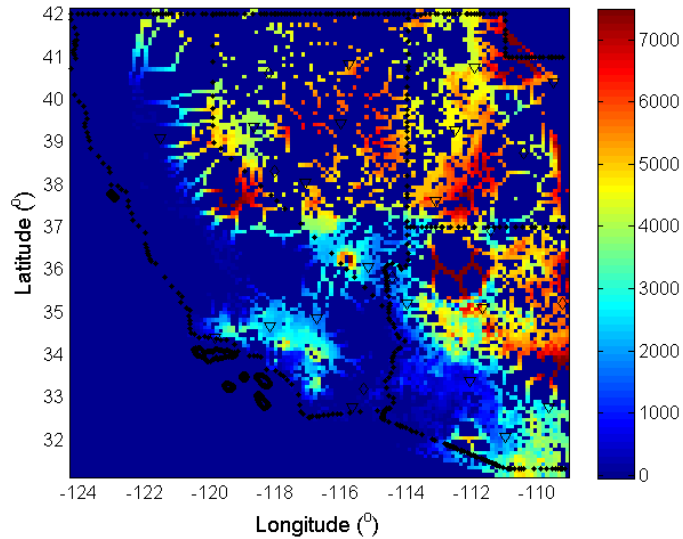
Figure 4.16. Reconstructed groundwater network in the southwestern US, 2004

We select the best interpolation result using the four interpolation methods (Delaunay, Kriging, and Radial Basis Function, Inverse Distance Weighting). Phoenix in Arizona is selected to show validity of the self-check method and superiority over the traditional interpolation methods.

A comparison by varying the sampling rates and picking the best interpolation value over a 21 year period is shown in Figs. 4.17. The sampling rate affects the accuracy similarly, as shown in Figs 4.8-10. Sampling rates of 30 % and 50 % do not perform well, even in comparison with the best interpolation method, because the lines have a large degree of fluctuation. As a proper sampling rate (59 %-60 %) is approached, the accuracy is enhanced accordingly. Obviously, the highest accuracy is obtained at the maximum sampling rate. The original points are precisely reconstructed by the proper sampling rate and maximum sampling rate, so that three lines appear as one in both figures. Regarding the interpolation methods, even though the best value was selected, the interpolated value

does not match at all in either figure. Hence, the sampling rate must be carefully selected when a low sampling rate is required for sensing.
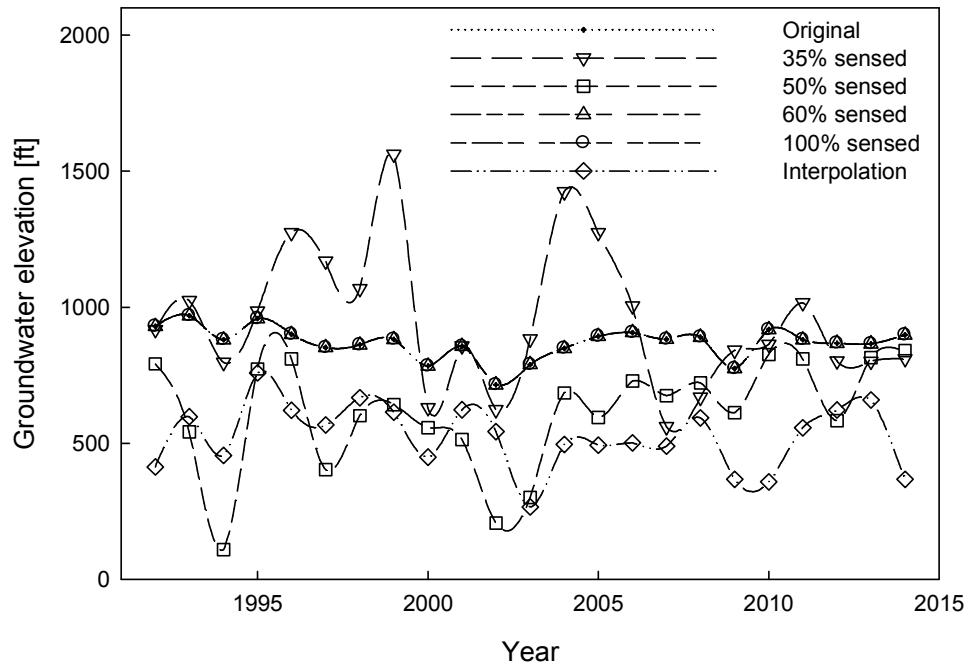


Figure 4.17. Point validation in Phoenix, AZ, from 1992 to 2012

   Groundwater elevation over long periods is compared with reconstructed groundwater elevation by CS. The results are plotted in Fig. 4.18. This shows the correct reconstruction and validity of the suggested method (CS) for developing the established groundwater network data.

80
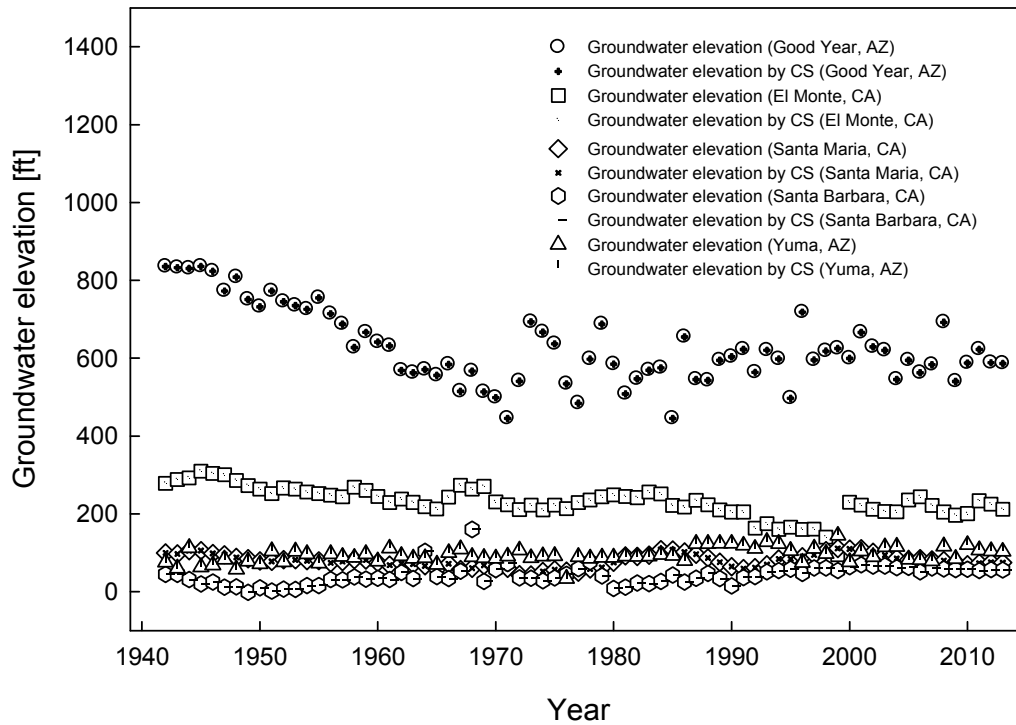
Figure 4.18. Comparison line plot of the measured groundwater elevation with reconstructed groundwater elevation for various cities of the southwestern US

According to the groundwater budget description given in the Section 2, changes in groundwater range from 0 to 25 feet. Even a small number in feet can be a large amount of groundwater storage because the original LSM data are the point estimate ($kg/m^2$) in $0.25° \times 0.25°$ area (approximately 625,000,000 $m^2$). Its contour plot in 2002 (measuring 62 by 45) is shown in Fig. 4.19.
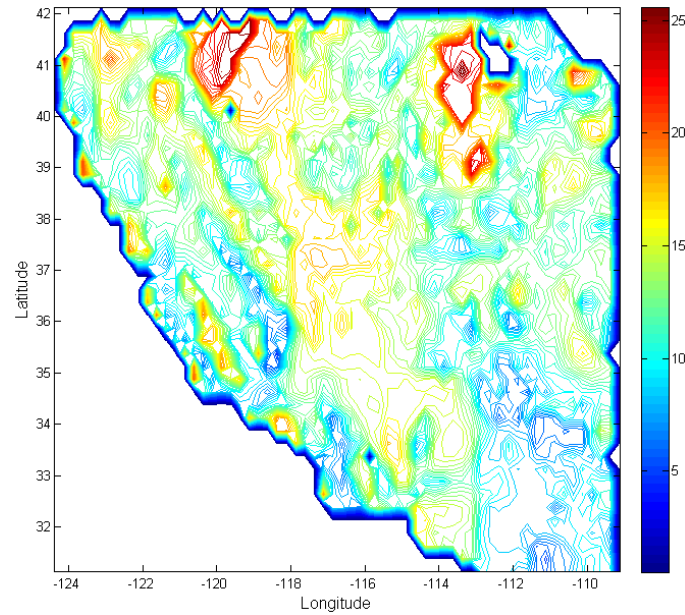
Figure 4.19. Groundwater budget contour plot of the southwestern US, 2002

To construct a contour plot of groundwater elevation for a region lacking compressed sensing data, the average values of groundwater level data over 72 years were used. After the data infusion was performed, a contour plot of groundwater elevation in 2002 (62 by 45) was generated, as shown in Fig. 4.20.

Figure 4.20 exhibits many noticeable differences relative to Figure 4.19. These differences arise from the fact that groundwater elevation reflects the topographical changes in the southwestern US, which ranges from -50 feet to 9000 feet, as well as the large differences in the control values in each figure. In spite of these disadvantages, a similar, constant contour was found in certain regions over the periods. The contours around Fresno, CA (36°45′N, 119°46′W), are clearly similar to each other. This region is well known as groundwater depletion area due to extreme agricultural irrigation by pumping groundwater.
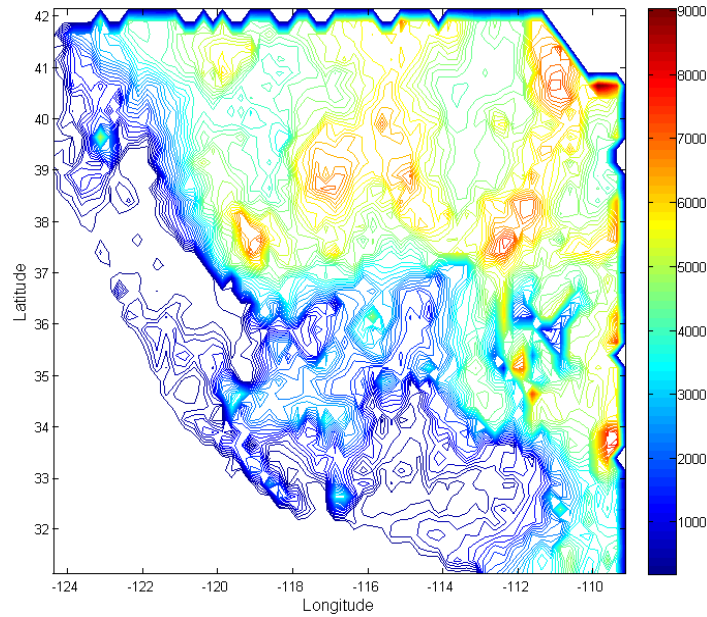
Figure 4.20. Groundwater elevation contour plot of the southwestern US, 2002

Several regions in the southwestern US were investigated to validate the CS method based on the groundwater budget. These regions include Luke Air Force Base (AFB) in Arizona; Mercury in Nevada, Oxnard in California, and Delta in Utah. The line plots are shown in Figs. 4.21. A comparison of the groundwater elevation with the groundwater budget shows a very similar trend among the two within those areas. In military regions, groundwater elevation is well matched with the groundwater budget. Possible reasons for this might be that the groundwater is not heavily used in these areas, that surface runoff is hindered by the pavement and that the areas are highly monitored by the Water Departments or other regulations.
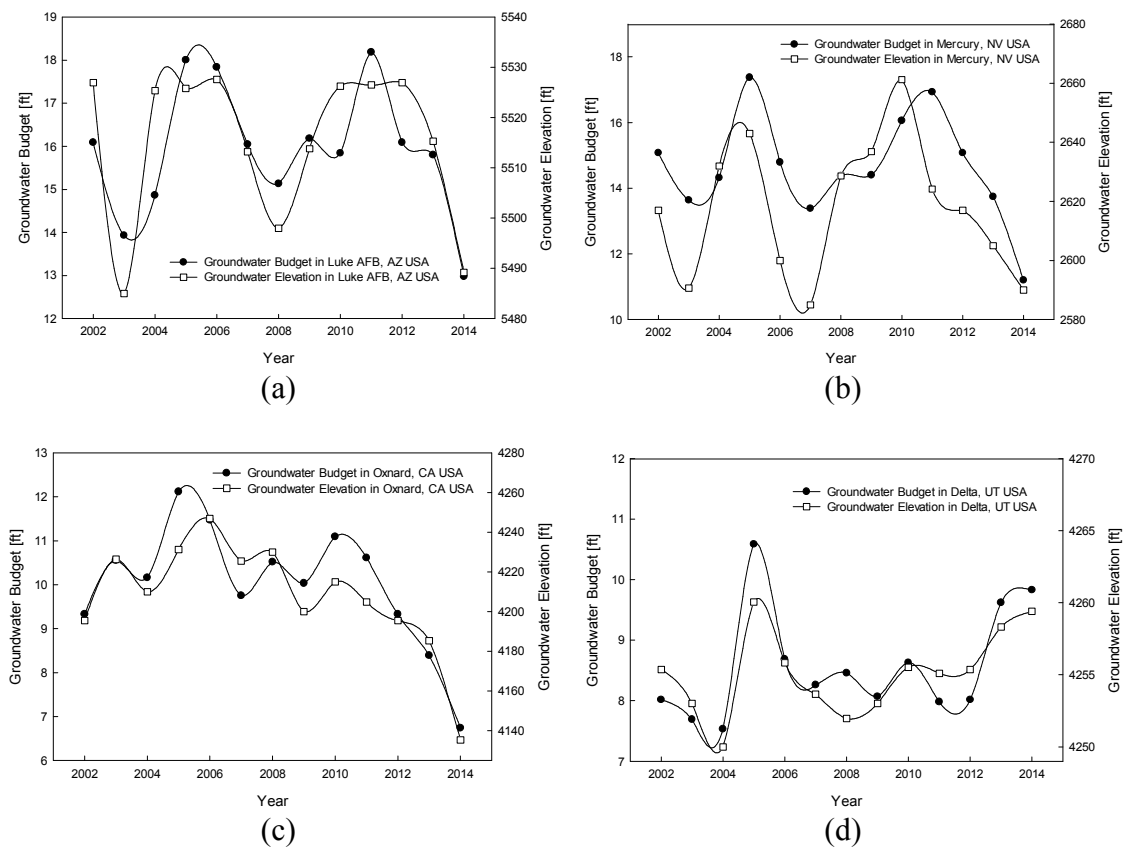
Figure 4.21. Comparison of the groundwater budget with the groundwater elevation at (a) Luke AFB, AZ, USA (b) Mercury, NV, USA (c) Oxnard, CA, USA (d) Delta, UT, USA

To validate our data based on a comparison with the NASA wetness percentile, line plots for comparing the wetness percentiles with groundwater percentiles for Prescott in Arizona, Caliente in Nevada, Merced in California, and Cedar City in Utah are shown in Figs. 4.22 at a spatial resolution of 0.25 degrees. These trends are clearly well matched in the southwestern US. At this spatial resolution, stable trend matches around all regions could not be found even though some areas shown in Fig. 4.22 are showing good agreement.
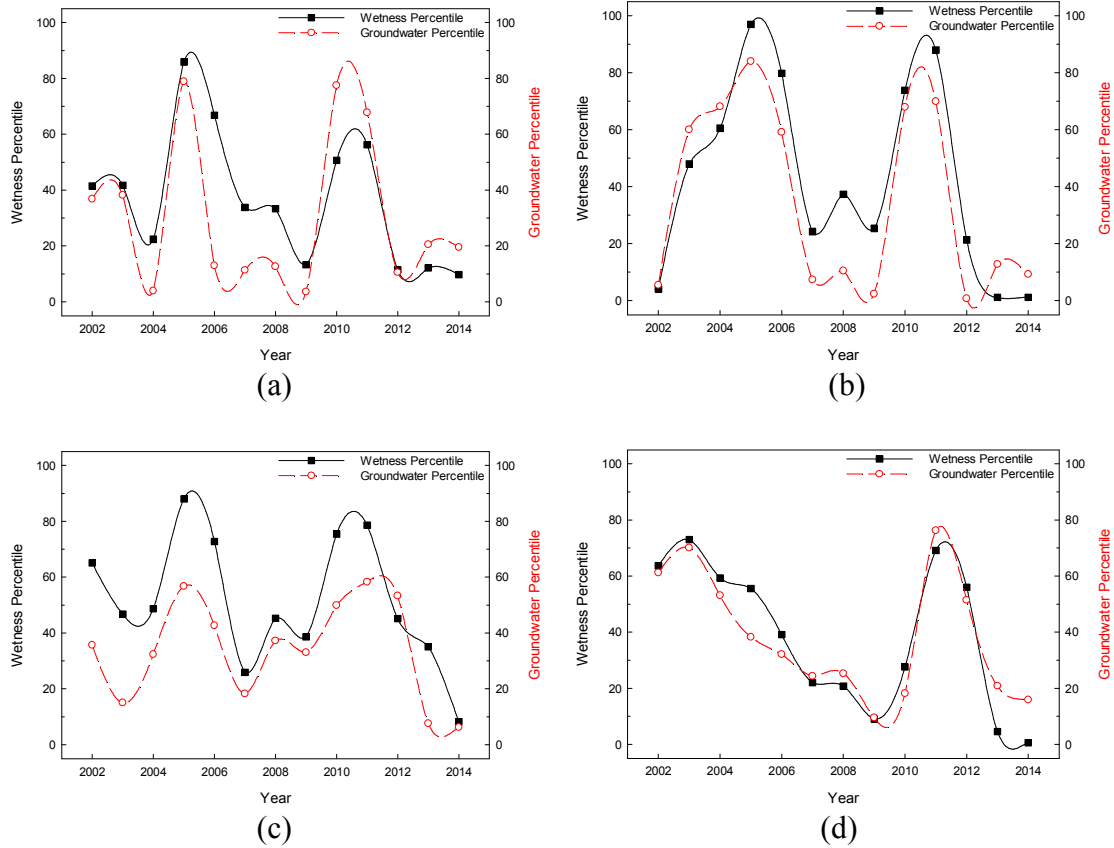
Figure 4.22. Comparison of wetness percentile with groundwater percentile in (a) Prescott, AZ (b) Caliente, NV (c) Merced, CA (d) Cedar City, UT, at a spatial resolution of 0.25 degree

To find more locations showing similar trends between the groundwater percentile and NASA wetness percentile, while varying the spatial resolution, several grids at varying resolutions (in degree) were investigated. Among these attempts, the 1-degree grid is used to make a line plot for validation comparisons, as shown in Fig. 4.23. Modesto and Fresno in California, Salt Lake City and St. George in Utah, Las Vegas in Nevada, and St. Johns in Arizona are represented in Fig. 4.23. 1-degree grid is estimated as 100 km by 100 km. Strictly speaking, the city mentioned above is included in the grid. These results present very similar trends, and most of the locations show patterns that are highly similar to those presented in the figures. The number assigned in each grid cell

85

represents the location of the groundwater percentile and wetness percentile in the

southwestern US.
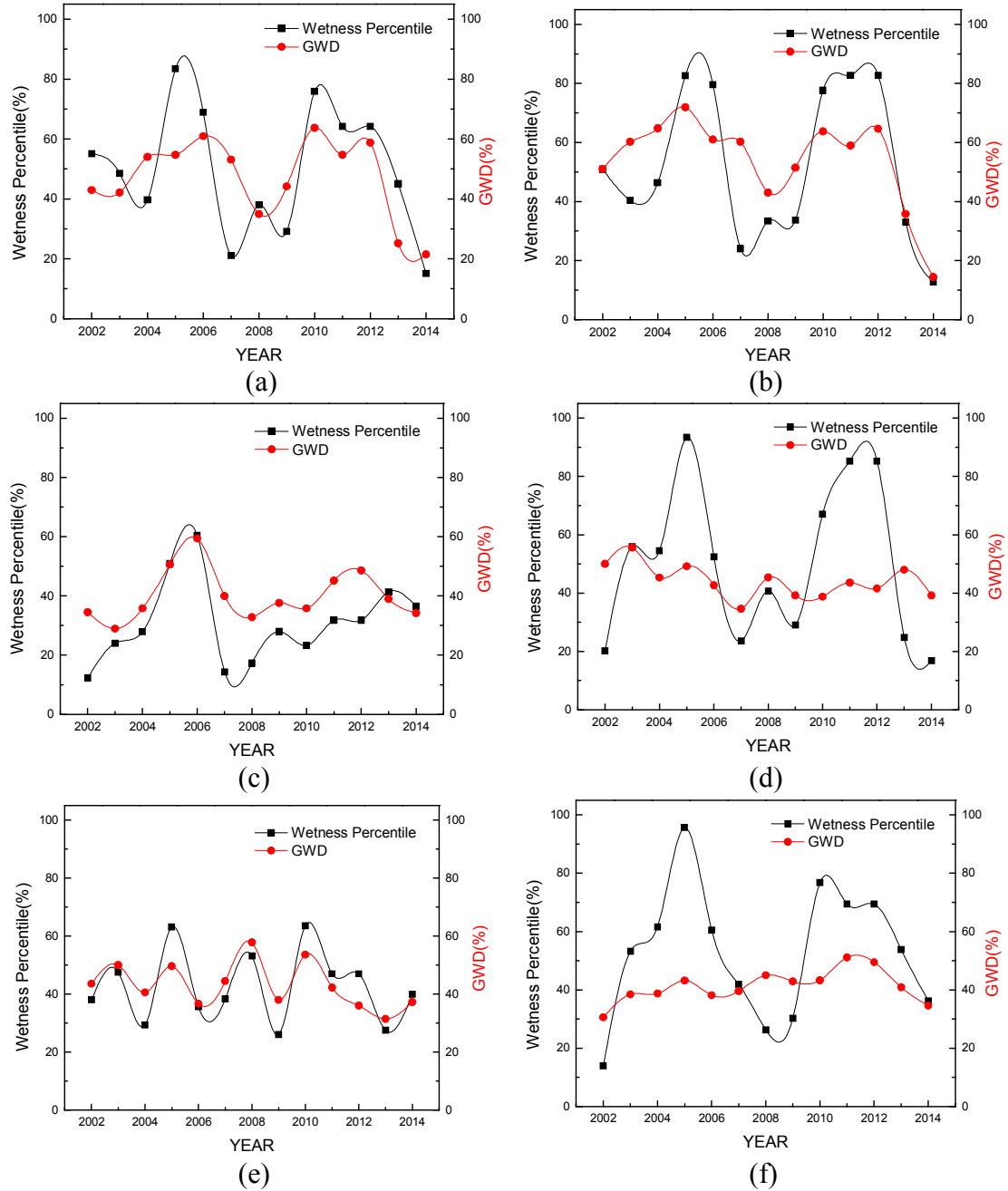


Figure 4.23. Comparison of wetness percentile with groundwater percentile in (a) Modesto, CA (b) Fresno, CA (c) Salt Lake City, Utah (d) Saint George, UT(e) St. Johns , AZ (f) Las Vegas, NV, at a spatial resolution of 1 degree

Although the l1-optimization problem has been solved over a certain sampling rate, the error increases exponentially as shown in Fig. 4.24. The compression rate, as defined below, is inversely proportional to the error norm.

$$\text{Compression rate} = \sum_{\forall i} k_i \big/ n^2$$

The compression rate is specified as the cardinality (total sum of non-zero elements) divided by the total size of the groundwater network. The results of this calculation can be interpreted as a measure of the compressibility of a data set. The validity degrades significantly as the compression rate decreases. The critical compression rate was not easy to obtain; in this case, a red-dashed area is used to show the overlaid region of magnification in Fig. 4.24.
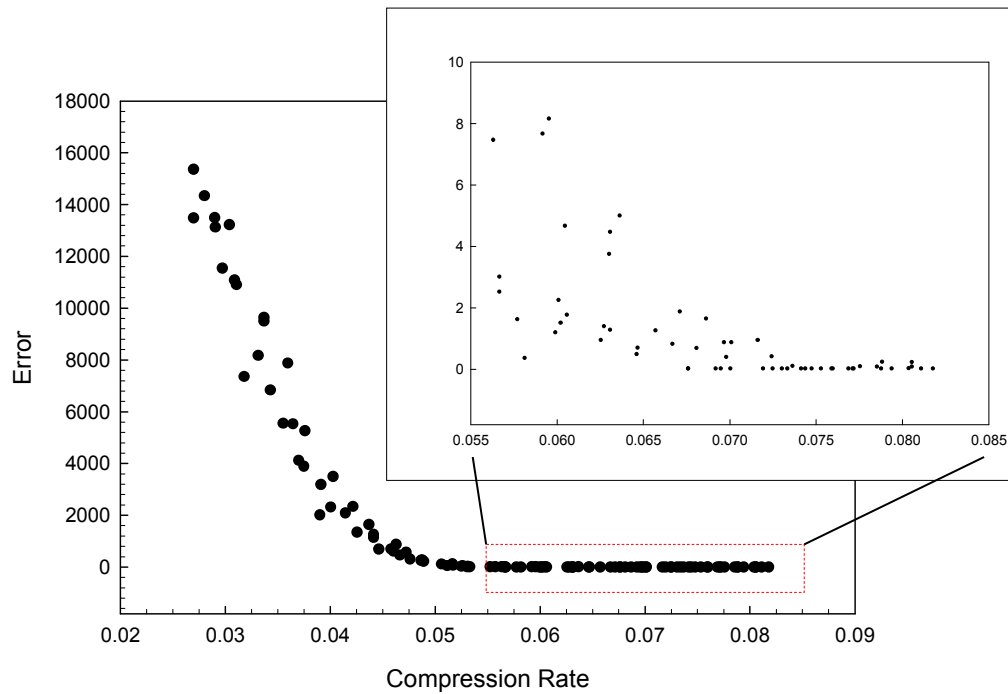


Figure 4.24. Plot between the error versus compression rate (a magnified view of the relationship between the error and compression rate is overlaid)

The compression rate at which the validity of the results is critically harmed is defined by values less than 5.8%. In a study such as this, the compression rate must be inspected in detail because a certain critical value of the sampling rate governs the performance of the l1-optimization. To do so, the condition that satisfies the RIP should be analyzed. The measurement bounds for achieving the RIP can be calculated by $M \geq C \cdot K \cdot \log\left(\frac{N}{K}\right)$, where C is a small number. In the groundwater network presented in Fig. 4.11, the total sum of the non-zero measurements is approximately 743 of 2790, giving a value of 26.7 %. By simple calculation with C≈0.37, we obtain M ≥462. In Fig. 4.25, the minimum boundary to meet the RIP from the groundwater network data from 1942 to 2014 is calculated. The original data points (black circles) represent the cardinality of the original groundwater network, and the minimum boundary is plotted with inverted triangles. We can use the values above the minimum boundary for the algorithmic loop, guaranteeing a successful reconstruction. If the sampled data points fall below the minimum boundary, our method is highly likely to fail reconstruction.
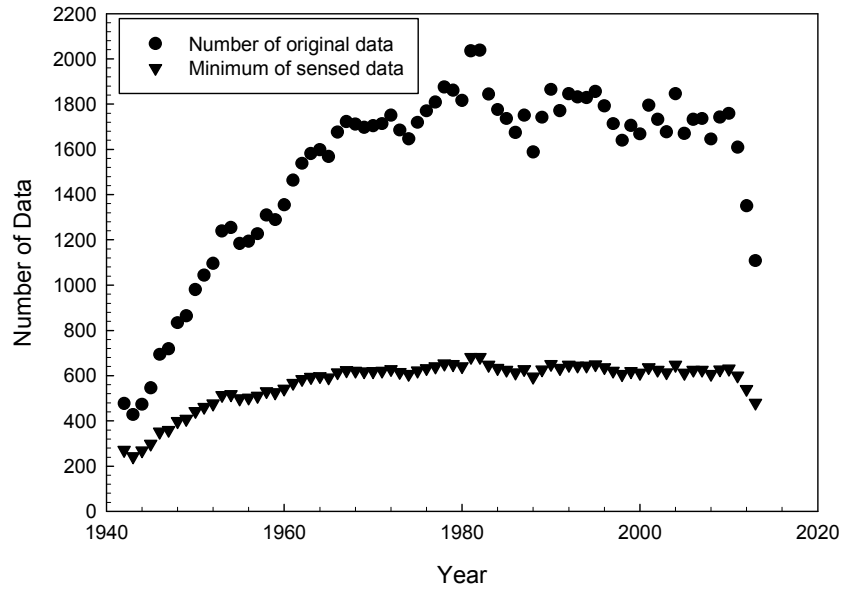
Figure 4.25. Minimum boundary for achieving the RIP in the groundwater network

The difference between digitally sensed data and analog data in terms of cardinality on a 2-D matrix should be noted. Digitally sensed data contain the meaningful data source in a numeric format throughout the entire 2-D matrix; however, the analog format data does not contain such meaningful data in any region that has not been sensed (or measured). In particular, the element of zero in a 2D matrix of digitally sensed data can be used in the l1-optimization procedure because it is a projected value developed during sensing. In other words, the element of zero can be an important proper basis for a compressible signal. However, a value of zero in analog data cannot be regarded to hold the same meaning for digitally sensed elements of zero. For example, the phantom reconstruction (or Shepp-Logan Image reconstruction) retains at least half of the meaningful data out of the total size of a 2-D image. In that regard, the compression rate can be as low as 5 %. In our case, the total counts of measurements in a 2-D matrix (total

89

of 2,790 elements) vary, ranging from several hundred to thousands. This represents a compression rate range from approximately 14 % to 32 %. The key performance attribute of the groundwater level estimation based on compressed sensing depends on the extent to which the measurements can be sensed in a compressive manner. We should increase the meaningful measurement rate throughout the total domain size by at least to 50% to improve the compressed sensing rate. In our case, the rate is 1,380 of 2,790. To overcome the lack of good performance in the analog data format, Xampling and a finite rate of innovation methods have been developed based on their well-designed circuitry. In this work, such methods cannot simply be applied to the past data in the GWSI site inventory. That is, for the past groundwater network data, these measurements are data-dependent. However, for future research utilizing advanced analog to digital converting technology, such data conversions may be more accessible than those performed in the past.

Although the groundwater network data have been constructed, the geological area, which guarantees the accuracy of reconstructed results, should be considered. For example, metropolitan Phoenix resides upon the Phoenix basin. The Phoenix basin is very flat and has not shown any severe change in groundwater elevation. This type of geological area is very suitable for our research. In contrast to observations recorded for the Phoenix basin, the Bulge of Sedona is not a good area of research for the suggested methods because the elevation changes are significant within a narrow region because this region is a valley.

The integrity of historical well data is another point of concern. In the data pre-processing phase, any unverified data were removed to the best of our ability. Because only a very small portion of the well data is maintained as a verified source in the USGS,

and access to this network requires authority, certain limitations are inherent in the comprehensive construction of groundwater level network data. For example, ADWR maintains the registered wells either periodically or continuously. The real-time data from these wells have not been provided to the public; as a result, even though these wells are monitored continuously or for short periods of time, we can only construct the data provided at the time of query on our side. The utilization efficacy of groundwater level data can be enhanced if the access limit is unlocked.

The matrix size can be adjusted by either increasing or decreasing the grid dimensions in terms of longitude or latitude. However, without increase of the meaningful measurements, this approach would not enhance the quality of a groundwater level estimation.


## 5. Conclusion

We investigated estimation methods of groundwater using CS in this work. Our suggested method outperformed the traditional geological interpolation methods in terms of accuracy. After validations through the wetness percentile and the groundwater budget, our groundwater estimation method using CS proved to work very well since our method results were matched with those from NASA groundwater trends.

The suggested method is very useful because it reduces the required number of total measurements by at least 42%. It is also an effective method for visualizing discretely measured, sparse data because a sparse dataset can be augmented by a factor of 1.7. If the size of the sampled data fall within certain ranges, which are governed by the CS properties, our method can be effectively used to estimate the groundwater level in the

southwestern US. Using the suggested method, trend analysis could be done for future research.

References

1. Atlas, R.M. and Lucchesi, R. 2000. File specificatioin for GEOS-DAS gridded output. *DAO-1001*, Ver. 4.3, 41.

2. Baraniuk, R.G. 2007. Compressive sensing. *IEEE Signal Processing Magazine*, 24 (4): 118-121.

3. Boyd, S. and Vandenberghe, L. 2004. *Convex optimization*. Cambridge:Cambridge University Press.

4. Brassel, K.E. and Reif, D. 2010. A procedure to generate Thiessen polygons. *Geographical Analysis*, 11 (3): 289-303.

5. Candes, E.J., Romberg, J., and Tao, T. 2006. Robust uncertainty principles: exact signal reconstruction from highly incomplete frequency information. *IEEE Transactions on Information Theory.* 52 (2): 489-509.

6. Clarke, R. and King, J. 2004. *The atlas of water:mapping the world's most critical resource*. London:Earthscan Publications, Ltd.

7. Cohn, S.E., Da Silva, A. , Guo, J. Sienkiewicz, M., and Lamich, D. 2003. Assessing the effects of data selection with the DAO physical-space statistical analysis system. *Monthly Weather Review*, 126 (11): 2913-2926.

8. Cosgrove, B.A. and coauthours 2003. Real-time and retrospective forcing in the north American land data assimilation system project, *Journal of Geophysical Resources*, 108 (D22): 8842-8853.

9. Cunningham, W. Direct conversation, March 15, 2013.

10. DeVore, R.A. 2007. Deterministic constructions of compressed sensing matrices. *Journal of Complexity*, 23 (4-6): 918-925.

11. Divekar, A. and Ersoy, O. 2009. Image fusion by compressive sensing. *The 17th International Conference on Geoinformatics*, in *Fairfax, VA*. Aug. 12-14.  2 (1): 1-6.

12. Donoho, D.L. 2006. Compressed sensing. *IEEE Transactions on Information Theory.* 52 (4): 1289-1306.

13. Duarte, M.F. and Eldar, Y.C. 2011. Structured compressed sensing: from theory to applications. *IEEE Transactions on Signal Processing.* 59 (9): 4503-4085.

14. Elad, M. 2010. *Sparse and Redundant Representations.* New York:Springer.

15. Elad, M., Starck, J.-L., Querre, P., and Donoho, D.L. 2005. Simultaneous cartoon and texture image inpainting using morphological component analysis (MCA). *Applied and Computational Harmonic Analysis*, 19 (3): 340-358.

16. Eldar, Y.C. and Kutyniok, G. 2012. *Compressed Sensing: Theory and Applications.* Cambridge:Cambridge University Press.

17. Gleick, P.H. 1993. *Water in crisis: A guide to the world's fresh water resources.* Oxford:Oxford University Press

18. Hackett, O.M., 1963. *Ground-water levels in the United States 1956-1960 southwestern states*. Geological Survey Water-Supply Paper 1770.

19. Hamill, T. M., R. P. d'Entremont, and J. T. Bunting, 1992. A description of the Air Force real-time nephanalysis model. *Weather and Forecasting*, 7 (2): 288-306.

20. Han, Dazhong and J. Wahr, 1995. The viscoelastic relaxation of a realistically stratified earth, and a further analysis of post-glacial rebound, *Geophysical Journal International*, 120 (2): 287-311.

21. Hansen, M.C., DeFries, R.S. Townshend, J.R.G., and Sohlberg, R., 2000. Global land cover classification at 1km spatial resolution using a classification tree approach. *International Journal of Remote. Sensing*, 21 (6-7): 1331-1364.

22. Huffman, G. J., R. F. Adler, E. F. Stocker, D. T. Bolvin, and E. J. Nelkin, 2003. Analysis of TRMM 3-hourly multi-satellite precipitation estimates computed in both real and post-real time. In *Proceedings of 12th Conference on Satellite Meteorology and Oceanography, Long Beach, CA, February 8-13*, P4.11.

23. Idso, S., 1981. A set of equations for the full spectrum and 8- and 14-micron and 10.5- to 12.5 thermal radiation from cloudless skies. *Water Resources Research*, 17 (2): 295-304.

24. Klinker, E., F. Rabier, G. Kelly, and J. F. Mahfouf, 2000. The ECMWF operational implementation of four dimensional variational assimilation. Part III: Experimental results and diagnostics with operational configuration. *Quarterly Journal of the Royal Meteorological Society*, 126 (564): 1191-1215.

25. Kopp, T. J., and R. B. Kiess, 1996. The Air Force Global Weather Central cloud analysis model. In *proceedings of 15th Conference on Weather Analysis and Forecasting,* in *Norfolk, VA, August 19-23*, 1220-1222.

26. Lin, G.F. and Chen, L.H. 2004. A spatial interpolation method based on radial basis function networks incorporating a semivariogram model. *Journal of Hydrology.* 288 (3-4): 288-298.

27. Mahrt, L. and Ek, M. 1984. The influence of atmospheric stability on potential evaporation. *Journal of Applied Meteorology,* 23 (2): 222-234.

28. Mahrt, L. and Pan, H. 1984.A two-layer model of soil hydrology. *Boundary Layer Meteorology,* 29: 1-20.

29. Olea, R.A. 1974. Optimal contour mapping using universal Kriging. *Journal of Geophysical Research.* 79 (5): 695-702.

30. Ottle, C., and D. Vidalmadjar, 1992. Estimation of land surface temperature with NOAA9 data. *Remote Sensing of Environment*, 40 (1): 27-41.

31. Pfaendtner, J., S. Bloom, D. Lamich, M. Seablom, M. Sienkiewicz, J. Stobie, and A. da Silva, 1995. Documentation of the Goddard Earth Observing System (GEOS) Data Assimilation System-Version 1. *NASA Technical Memorandum 104606,* 4: 1-44.

32. Reynolds, C. A., T. J. Jackson, and W. J. Rawls, 2000. Estimating soil water-holding capacities by linking the Food and Agriculture Organization Soil map of the world with global pedon databases and continuous pedotransfer functions. *Water Resources Research*, 36 (12): 3653-3662.

33. Rodell, M., P. R. Houser, U. Jambor, J. Gottschalck, C.-J. Meng,K. Arsenault, N. DiGirolamo, and D. Hall, 2002. Use of MODIS-derived snow fields in the Global Land Data Assimilation System. Presented at *Mississippi River Climate and Hydrology Conference*, in *New Orleans, LA, May 15*, 118.

34. Rodell, M., Chen, J., Kato, H., Famiglietti, J.S., Nigro, J., and Wilson, C.R. 2006. Estimating groundwater storage changes in the Mississippi river basin (USA) using GRACE. *Hydrogeology Journal,* 15 (1): 159-166.

35. Rodell, M., Houser, P.R., Jambor, U., Gottschalck, J., Mitchell, K., Meng, C-J., Arsenault, K., Cosgrove, B., Radakovich, J., Bosilovich, M., Entin, J.K., Walker, J.P., Lohmann, D. and Toll, D. 2004. The global land data assimilation system. *American Meteorological Society,* 85 (3): 381-394.

36. Schaake, J.C., Koren, V.I., Duan, Q-Y., Mitchell, K. and Chen, F. 1996. Simple water balance model for estimating runoff at different spatial and temporal scales. . *Journal of Geophysical Research.* 101 (D3): 7461-7475.

37. Shapiro, R., 1987: A simple model for the calculation of the flux of direct and diffuse solar radiation through the atmosphere. Air Force Geophysics Laboratory, *AFGL-TR-87-0200*, Hanscom AFB, MA, 40.

38. Stojnic, M. 2010. $l_2/l_1$-optimization in block-sparse compressed sensing and its strong thresholds. *IEEE Transactions on Selected Topics in Signal Processing.* 4 (2): 350-357.

39. Swenson, S., and Wahr, J. 2002. Estimated effects of the vertical structure of atmospheric mass on the time-variable geoid. *Journal of Geophysical Research*, 107 (B9): ETG4.1-11.

40. Takhar, D., Laska, J.N., Wakin, M.B., Duarte, M.F., Baron, D., Sarvotham, S., Kelly, K.F., and Baraniuk, R.G. 2006. A new compressive sensing imaging camera architecture using optical-domain compression. In *Proceedings of Computational Imaging IV at Society of Photo-Optical Instrumentation Engineers Electronic Imaging*, in *San Jose, CA, January 15*, 6065 (67001): 43-52.

41. Turk, F. J., G. Rohaly, J. D. Hawkins, E. A. Smith, A. Grose, F. S. Marzano, A. Mugnai, and V. Levizzani, 2000. Analysis and assimilation of rainfall from blended SSM/I, TRMM and geostationary satellite data. In Proceedings of $10^{th}$ *Conference on Satellite Meteorology and Oceanography*, in *Long Beach, CA, January 10*, 66-69.

42. Tillman, F. D. and Leake, S. A. 2010. Trends in groundwater levels in wells in the active management areas of Arizona, USA. *Hydrogeology Journal*, 18 (6): 1515-1524.

43. Todd, D.K. and Mays, L.W. 2005. *Groundwater hydrology 3rd ed*. Hoboken:John Wiley and Sons, Inc.

44. U.S. Geological Service. 2009. *Estimated use of water in the United States in 2005*. USGS Circular 1344.

45. Verdin, K. L. and Jenson, S. K. 1996. Development of continental scale digital elevation models and extraction of hydrographic features. In *Proceedings of $3^{rd}$ International Conference and Workshop on Integrating GIS and Environmental Modeling*, in *Santa Fe, NM*, *January 21*, Session 8.2.

46. Vinogradov, Y. B. 1988. Mathematical modeling of river runoff processes. *Gidrometeoizdat*, St. Petersburg, Russia.

47. Watson, D.F., and Philip, G.M. 1985. A refinement of inverse distance weighted interpolation. *Geo-Processing. Journal of Hydrology*. 2 (4): 315-327.

48. Yin, W., Osher, S., Goldfarb, D. and Darbon, J. 2008. Bregman iterative algorithms for l1-minimization with applications to compressed sensing. *Journal of Imaging Science in Society for Industrial and Applied Mathematics*, 1 (1): 143-168.

**CHAPTER 5**

**TRENDS IN GROUNDWATER ELEVATION IN THE SOUTHWESTERN US**

## 1. Introduction

Groundwater is among the most important natural resources. Measurements of groundwater levels in wells indicate the status of this resource, especially, used to evaluate the quantity and quality of groundwater and its interaction with surface water. Using the suggested method in the previous chapter by help of these essential data via Federal, State and Local agencies over the long-term period, trends in groundwater levels have been investigated in the southwestern United States (US). Through this effort, in coming decades, there will be a good policy made for appropriate use of its extensive groundwater resources.

Groundwater is held by underground aquifers, representing almost all fresh water that is not in the form of ice (Clarke and King 2004). In other words, groundwater is commonly understood as the water occupying all of the voids within a geologic stratum. Groundwater presents a potential solution to the lack of potable water faced by many regions of the world. However, groundwater is a scarce resource because only 2.5% of all water resources on Earth are fresh water, and only 30.1% of all of the fresh water resources are in the form of groundwater (Gleick 1993).

Groundwater sources provided approximately 23% of the fresh water consumed in the United States in 2010. Surface water sources supplied the other 77%. The exploitation of groundwater requires more work and is more costly than accessing surface water; however, in the arid regions of the US, where minimal surface water is present,

groundwater is the only source of water for satisfying the region's water needs (Gleick 1993).

The bar chart in Fig. 5.1 shows the United State's use of ground and surface water resources from 1950 to 2010. According to this chart, groundwater is important for meeting the everyday water needs of the US. Groundwater is regularly used for irrigating crops and supplying water to homes, businesses, and industries (U.S. Geological Service 2005). The central bar in each set of three bars shows the amount of groundwater withdrawn in the United States in the corresponding year. In total, approximately one-quarter of the historical water used in the United States has come from groundwater. This proportion has remained relatively constant throughout the last 50 years. The majority of groundwater goes toward crop irrigation. Groundwater is also used by people who supply their own home water (self-supplied domestic use).
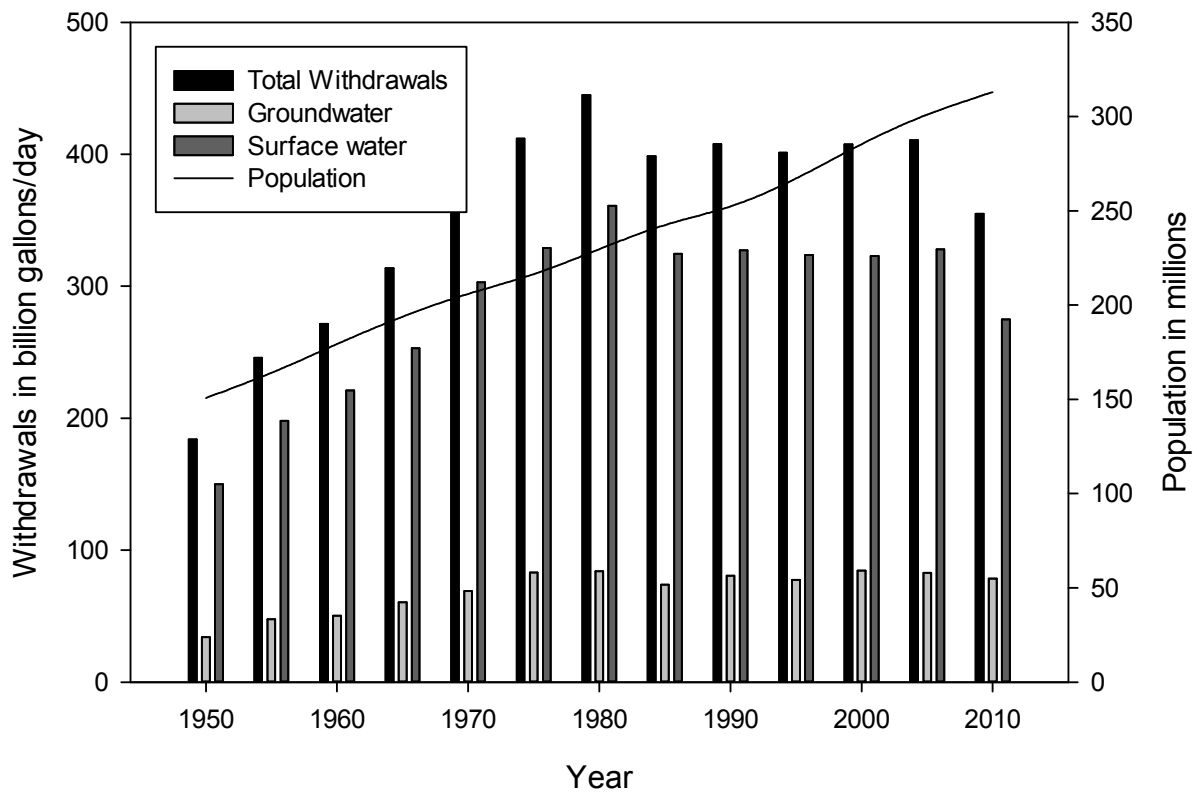
Figure 5.1. Trends in population and freshwater withdrawals by source, 1950-2010 (Courtesy of USGS)

The area of interest encompasses the southwestern states of the United States such as Arizona (AZ), California (CA), Utah (UT), and Nevada (NV). The study area in Arizona lies within 72 identifiable unconsolidated Alluvial Basins in the arid to semi-arid southwestern US as shown in Fig. 5.2. The annual average precipitation generally ranges from 8 to 76 cm (Anderson et al. 1992). Coarse-grained surface sediments are prevalent near mountain fronts while fine-grained surface sediments are dominant towards basin centers (Anderson et al. 1992; Anderson 1995).

In California, Central Valley Basin is the main area of interest since groundwater depletion is remarkably noticed. It is a major agricultural area in a large valley with an

area of about 52,000 km$^2$ (Williamson et al. 1989; Bertoldi et al. 1991). It includes the Sacramento Valley, the San Joaquin Valley, and the Tulare Basin. Its climate is an arid to semi-arid Mediterranean. The annual average precipitation ranges from 33 to 66 cm in the Sacramento Valley and 13 to 41 cm in the San Joaquin Valley (Bertoldi et al. 1991). Streamflow entirely supplies the water to the valley. This area depends heavily on precipitation in the Sierra Nevada to the east and in parts of the Klamath Mountains in the north (Williamson et al. 1989). Besides, Antelope Valley, Mohave River Basin, Death Valley Region, Coachella Valley, Los Angeles Basin are included in the area in CA.

In Utah, the Beryl-Enterprise area of the Escalante Desert in the Basin and Range physiographic province is our concern and its area is about 4,970 km$^2$ (Mower 1982). Drastic declines in groundwater level resulted from groundwater development in the region. The aquifer system is made up of saturated unconsolidated to semi-consolidated valley fill. Thickness ranges from zero near the edge of the valley to more than 300 m in the central part of the valley. The average annual precipitation is less than 30.5 cm in most of the irrigated parts of the area and ranges from about 2 to 76 cm in the mountains (Mower 1982). The Milford area is our area of work and its area is about 3,000 km$^2$ in the northern part of the Escalante Desert. The average annual precipitation is about 23 cm (Slaugh 2002). Its climate varies from seim-arid on the basin floor to sub-humid at higher altitudes.

In Nevada, the Death Valley region covers 100,000 km$^2$ of southern NV and southeastern CA. The aquifer consists of carbonate, volcanic and alluvial rock units (Belcher et al. 2010). Surface water is limited in the region, groundwater is major sources

of water supply, and its climate is typically arid. In the southern NV, Las Vegas Valley is

located, its area is 4,050 km$^2$, and it has an arid climate. The major geologic units are

bedrock and valley fill deposits (Wood 2000; Plume 1986).
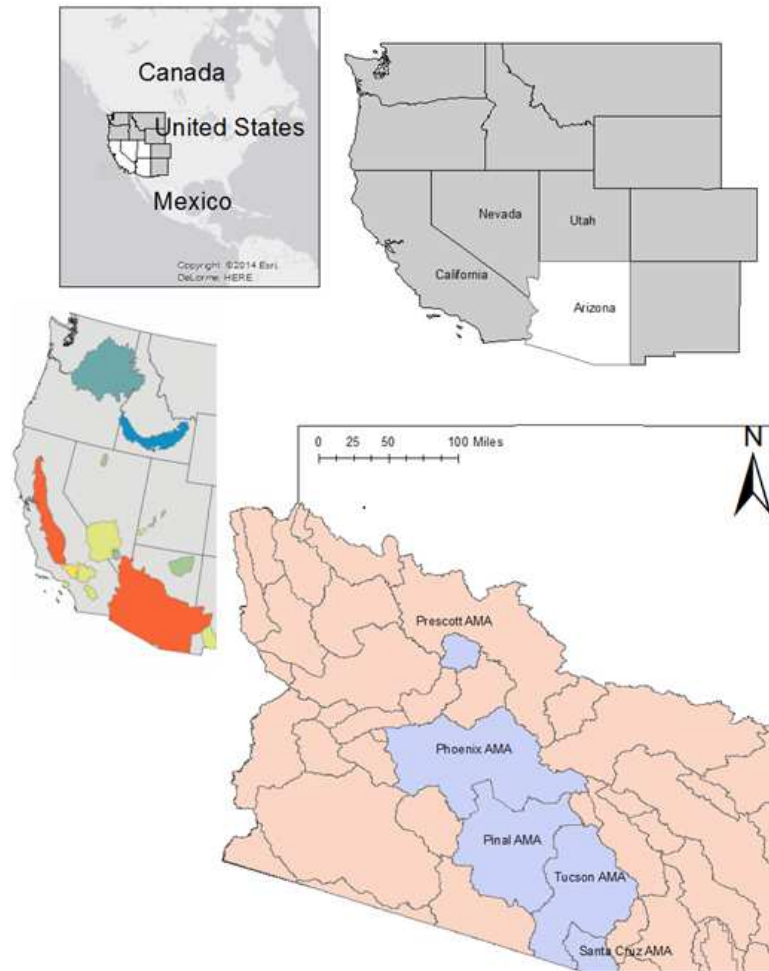


Figure 5.2. Map depicting the locations of California, Arizona, Utah, and Nevada in the
southwestern United States, Aquifers of interest in the states and the active management
area (AMA) within the state of Arizona

Most of aquifers in our study are experiencing moderate to drastic declines of

groundwater level. Groundwater is pumped at greater rates than it can be naturally

recharged, so that immediate attention and remedial action needs to be required. For

example, since 2011, the amount of water removed from the Sacramento Valley and San Joaquin Valley in the Central Valley basin, CA each year added up to 4 trillion gallons, which is equivalent to or greater than the amount that 38 million Californian residents can use in cities and homes annually (Kaplan 2014).

Trends in groundwater levels are complex results from multiple factors over different time scales. Climate change affects the water cycle so that patterns of groundwater recharge from precipitation could be different from that of the past. For example, extreme drought impacts groundwater recharge. It makes a decrease in streamflows and dries up water reservoirs. Consequently, more groundwater pumping to meet the demand exacerbates groundwater depletion. Rapid decrease in groundwater level results from this complex result of subsequent events. In addition to precipitation, changes in population, water-use pattern, and inter-basin water transfers (Central Arizona Project) have multiple influences on groundwater level (Tillman and Leake 2010).

This trend analysis of groundwater level over the long-term period may be useful for 1) recognition and acceptance of groundwater depletion in that more water is used than is available on an annual and renewable basis (Famiglietti 2014); 2) determination of effectivity in groundwater management strategies in certain states; 3) reassurance of needs for effective resource management by sharing measured groundwater level data across political boundaries since groundwater level is a good and direct indicator for groundwater management.

Materials and methods are explained in Section 2. In Section 3, Results are shown and discussion is followed. A limitation in this study is described in Section 4. Finally, conclusions are drawn in Section 5.

## 2. Materials and Methods

The United State Geological Survey (USGS) Groundwater Data Watch for Nations and groundwater data site in each state department of water were used to obtain groundwater level measurements. After data pre-processing, the CS method explained in the previous chapter was used to create groundwater elevation (groundwater level with respect to sea surface level) on a yearly basis.

First of all, a Matlab program was coded to conduct a linear regression on subsets of groundwater elevation data. Each subset is determined by specified criteria. While processing data by each criterion, internal check on data subset is done. Data subsets which are satisfied by each criterion are collected and then trend analysis is performed on them.

174 cities in the southwestern US were selected for a trend analysis. From the groundwater database by CS from 1942 to 2014, trends in groundwater elevation over the period was investigated in terms of three categories such as negative, neutral, and positive. For determination of trend, the associated trend line in each city was calculated and used. When the slope of the linear trend is greater than -1, then the trend is categorized as decreasing. When the slope of the linear trend is greater than 1, then the trend is called increasing. Otherwise, the trend falls within the neutral category. In addition, data counts for trend line calculation, average, standard deviation, median,

mode, maximum, minimum and difference between maximum and minimum were also calculated for statistical analysis.

Cities with data counts lower than 25 were not included in the analysis because 34% of data was lost due to unmeasured and non-estimated groundwater level so that it cannot correctly represent the trend over the period. Any city exhibiting measurement differences greater than 1000 feet was eliminated from the data set, too.

Secondly, trend in area sum of groundwater elevation is compared with trend in area-averaged groundwater percentile. Trend in area sum of total rainfall is drawn along with area-averaged wetness percentile for finding similar patterns. The groundwater percentile and wetness percentile are explained in the previous section of Chapter 4. So, please refer to the Section titled groundwater retrieval. In addition, relationship of total rainfall, groundwater budget and wetness percentile is researched by comparing area sum of total rainfall with area-averaged wetness percentile as well as area sum of groundwater budget.

The area of interest is selected by the report of the recent groundwater depletion trend (Famiglietti 2014) and the announcement of an imminent groundwater management plan or the media (Styler and Jones 2012; Kaplan 2014). The Central Valley Basins was chosen in California. In Nevada, the areas near Las Vegas were chosen. In Utah, the Beryl-Enterprise areas were selected. In Arizona, the areas around Prescott were investigated. For identification of the areas of interests, by using geologic information, the grids containing the areas in the groundwater network data base were marked. After this step, sum of values in the grids and averaged values in the lattices were calculated. By plotting a variety of combinations of the factors over years, we tried to find a similar trend among the specified factors.

The area sum of groundwater elevation, groundwater budget, accumulated snow, snow melt, temperature and total rainfall span from 2000 to 2014 while groundwater and wetness percentile can be shown from 2002 to 2014 according to the data availability for each data type. For data integrity, each data set was visually inspected first, after success on inspection, and then further processing was done. Especially, in the Central Valley Basins, the sum of accumulated snow on the Sierra Mountains is used along with the sum of total rainfall in the Central Valley Basins. We use a simple statistic to mark a warning level for these regions. Groundwater budget is used throughout this analysis method. It is the quantity of groundwater derived by satellite data from the National Aeronautics and Space Administration (NASA) Global Land Data Assimilation System (GLDAS). For detailed explanation, please refer to the Section 2 in the previous chapter.

Lastly, bracketing is used to set time period of interest. Bracketing requires at least 5 observations in a region to be included in the trend analysis. This ensures reliability of trend by elimination of small and not well-distributed data subsets, which can misrepresent a trend in that time bracket. Similarly in the first approach, any region exhibiting measurement differences greater than 1000 feet was eliminated from the data set, too.

Estimation program for groundwater elevation by the compressed sensing algorithm, explained in the previous chapter, generated groundwater network data to provide annual hydrographs for all regions. Visual inspection of hydrographs in wells in the sampled regions was done to check integrity of data and trend analysis. Then, trend in groundwater elevation in each well over the time bracket period was investigated by a linear regression. For trend categorization, the associated trend line in each well was

calculated and used. When the slope of the linear trend is less than 0, then the trend is categorized as decreasing. Otherwise, then the trend is called increasing. In addition, ratio of decreasing trend wells is compared with rate of groundwater depletion over the time bracket period (Konikow 2013).

A catalog of groundwater elevation contour map over the entire period was provided by help of the suggested method for data generation and the Delaunay method for the contour generation.

### 3. Results and Discussion

All groundwater level observations in this study were retrieved from the USGS Groundwater Data Watch for Nations and National Water Information System (NWIS) database as well as Arizona Department of Water Resources (ADWR), California Department of Water Resources (CDWR), Nevada Department of Water Resources (NDWR), and Utah Department of Water Resources (UDWR) site inventory databases. Data from these databases were collected and pre-processed for formatting to use the developed code in Matlab. The total number of data points included for this analysis in the southwestern US is approximately 1.5 million. The average data size each year totals approximately 14,000, and the total number of wells is approximately 0.1 million. The processed dataset was used to input for the linear regression code explained in the previous section. Trends in groundwater elevation in the selected cities were investigated for the period from 1942 to 2014.

An area-weighted sum of the measured groundwater elevation, along with an integrated sum of the reconstructed groundwater elevation, is plotted for Arizona in Fig.

5.3 as a function of time in years. The black dots represent the total area-weighted sum of the measured groundwater elevation, or the so-called original measurements. The circles show the integrated sum of the groundwater elevation after the suggested method was applied. As a result of CS, the estimated groundwater elevation in multiple areas within the regions of interest can be reconstructed so that the data are approximately expanded by a factor of 1.7.
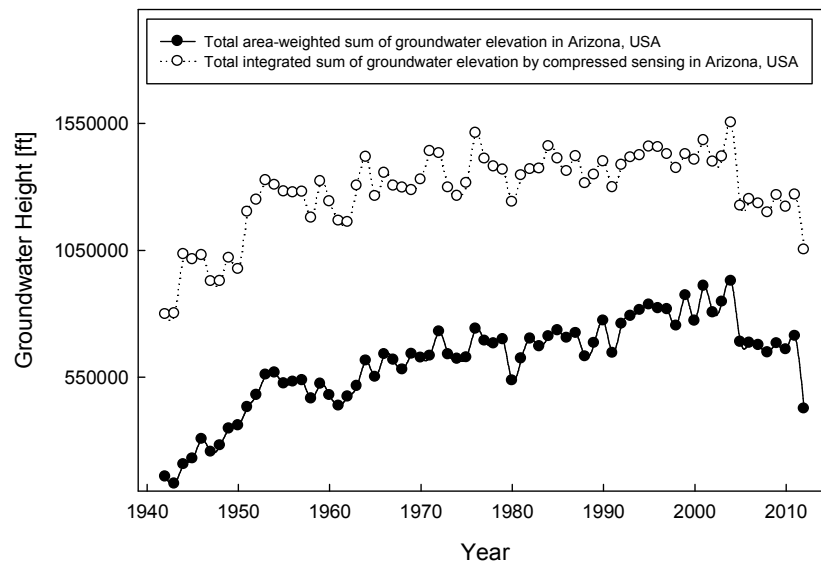


Figure 5.3. Comparison of the total area-weighted sum of groundwater elevation with the total integrated sum of groundwater elevation based on compressed sensing in Arizona, USA

After data filtered, only 78 cities were selected out of the 174 cities. City names are attached in the Appendix C. At least half of the cities in this study show a decreasing trend in groundwater elevation. In particular, 69% of the cities in Arizona show this decreasing trend. In California, a recent drought has impacted the groundwater elevation severely, so that 52.5% of cities lie within this decreasing trend. In Utah and Nevada,

decreasing and neutral trend is almost equally present. However, several areas in Utah

have been designated for groundwater management plan due to drastic declines of

groundwater elevation (Styler and Jones 2012). The results are tabulated in Table 5.1.

Table 5.1. Results of Trends in Groundwater Levels for the Cities in Each State of the US

| Area | Date Range | No. of investigated cities (total number of wells / total number of data) | Decreasing | Neutral | Increasing |
|---|---|---|---|---|---|
| California | 1942-2014 | 40 (41,346 / 725,762) | 21 (52.5%) | 14 (35%) | 5 (12.5%) |
| Arizona | 1942-2014 | 16 (34,434 / 221,974) | 11 (68.75%) | 3 (18.75%) | 2 (12.5%) |
| Utah | 1942-2014 | 11 (15,335 / 296,394) | 5 (45.45%) | 6 (54.55%) | 0 (0%) |
| Nevada | 1942-2014 | 11 (11,946 / 226,183) | 5 (45.45%) | 5 (45.45%) | 1 (9.1%) |

Arizona uses a lot of groundwater. More than eighty percent of the cities in Arizona

shows negative linear trend, and just two cities fell in the positive linear trend in Table

5.2. This intrigues further investigation for several candidate cities. The cities, located in

the vicinity of the Phoenix metropolitan area in AZ and exhibited a negative trend of -3,

were selected, and the resulting trend in groundwater elevation from 1942 to 2014 is

plotted in Fig. 5.4. 5 cities are Deer Valley, Gila Bend, Luke AFB, Scottsdale, Williams

AFB.

The decreasing trend from 1942 until 1980 is clearly shown in all 5 cities. But, after

1980, the slope of the trend levels off and even presents slight gains. The cause for trend

level-off in these regions resulted from the Arizona Groundwater Management Act

(GMA), which took effect after 1980 and was enacted to monitor groundwater level, by

supporting efficient use practices and eventually protecting the overuse of groundwater

from water-thirsty agricultural development (Tillman and Leake 2010).

Although this governmental regulation took effect to accommodate sustainable groundwater use, the absolute groundwater elevation remains below the earliest values reported, from the 1940s and 1950s. At Deer Valley, groundwater elevation started from around 1000 ft but, hit the bottom around 250 ft in 1980, and leveled off then gained back to 550 ft. This result agreed with the statement that the groundwater decline was more than 600 ft (Galloway et al. 1999). During the 1950s to 1970s, population growth in Arizona required significant quantities of groundwater and agricultural irrigation in the region with no surface water was entirely dependent on groundwater use. By recognizing serious problems such as groundwater depletion and entailed drawbacks (land subsidence), water management and water-use patterns changed after 1980. In addition, Central Arizona Project (CAP) has been importing surface water from Colorado River through 336 mile-long constructed aqueducts since 1985 to solve water supply deficit and eventually leading to decreases in groundwater withdrawals (Galloway et al. 1999).

Groundwater management has been continuing since GMA was initiated so that it could increase the opportunity for groundwater elevation to gain back its losses or at least be maintained at an appropriate level. Trends in 5 cities agreed with the statement that the Phoenix Active Management area has more wells classified as rising or nearly stable than declining for the time period of 2000 to 2008 (Tillman and Leake 2010).
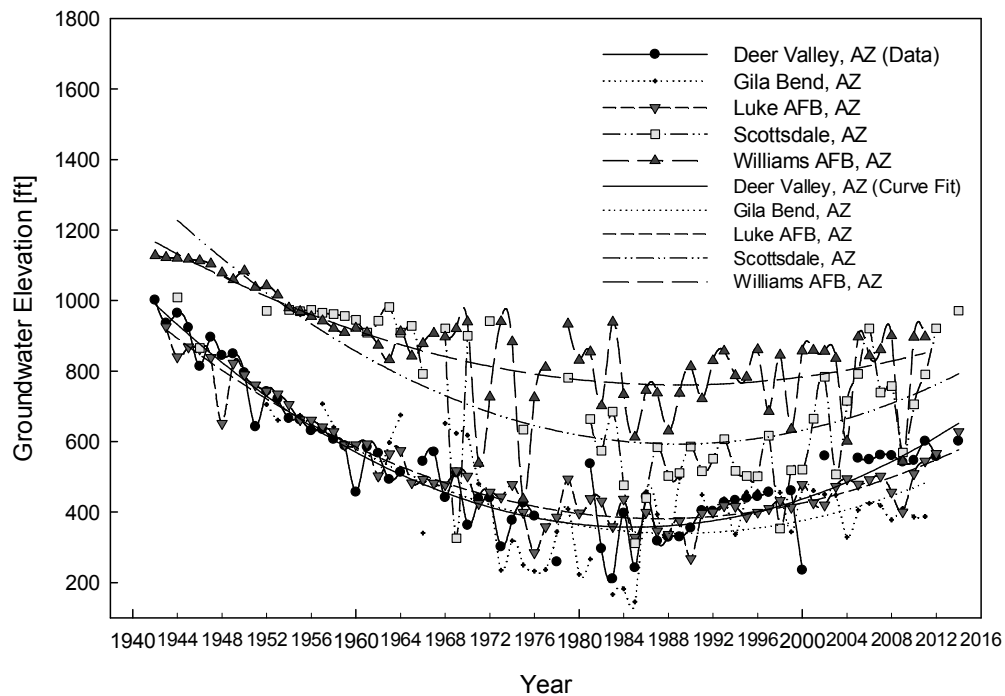
Figure 5.4. Groundwater elevation trends in 5 cities in metropolitan Phoenix, AZ

In Fig 5.5, for Scottsdale in Arizona, trend line in groundwater budget seems to parallel trend line in groundwater elevation even though those two quantities have a high fluctuation and several times those two lines were crossed. Irrigation by CAP should be accounted for to explain the rise in both groundwater elevation and groundwater budget in recent years. It is hard to find relationship between the total rainfall and groundwater elevation. The main causes to change groundwater elevation in the registered wells are very complex. Time range of groundwater recharge varies among the registered wells and artificial recharge to the wells by CAP also increases the complexity.
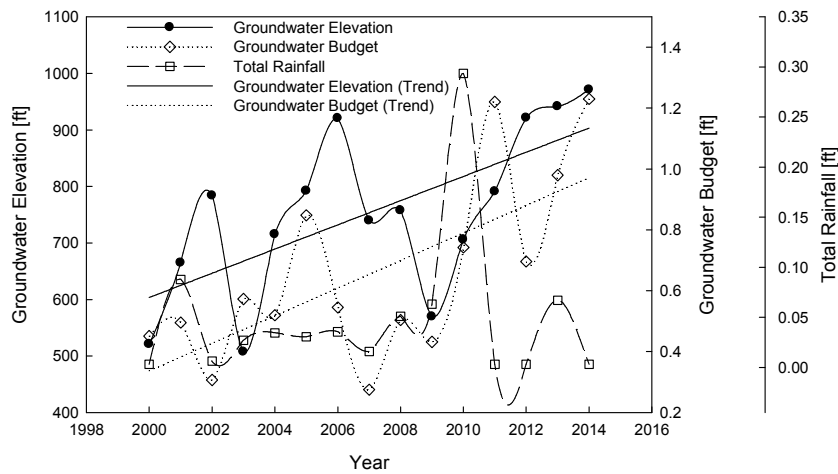
Figure 5.5. Comparison of the groundwater elevation, groundwater budget, and total rainfall in Scottsdale, AZ

For further investigation of direct relationship between the rainfall event and the change in groundwater elevation, small time scale would be better with smaller region than this study area since rainfall has a different intensity in each event. But, we found the very interesting fact between the rainfall and the groundwater budget while applying the second analysis method in different regions across the southwestern US. The area sum of total rainfall in Prescott, Arizona is compared with the area sum of groundwater budget in the same areas, shown in Fig. 5.6. This figure shows the same increasing or decreasing trend between the sum of total rainfall and the sum of groundwater budget except the period 2000-2001 even though they showed the apparent gap each year. The area sum of groundwater elevation fluctuated until 2008, after then it decreased. More exempt wells, which are private and domestic wells designed to pump no more than 35 gallons per minute, were drilled so that the increase in pumping from new wells causes groundwater elevation to decline continuously according to Prescott AMA issues.

111
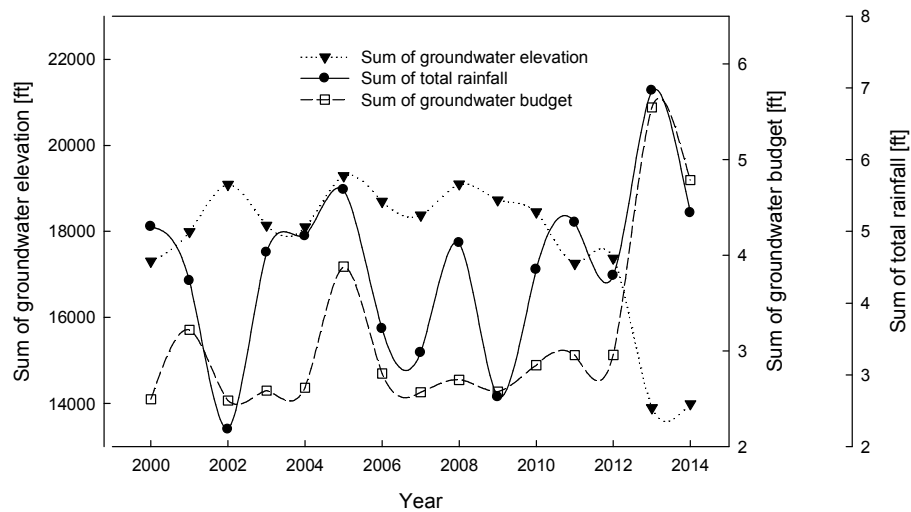
Figure 5.6. Comparison of the area sum of groundwater elevation, groundwater budget, and total rainfall in Prescott, AZ

The area sum of groundwater elevation seems to have no relation with those two

factors. So, we compared it with the area-averaged groundwater percentile shown in Fig.

5. 7. This shows very similar trend between the area sum of groundwater elevation and

the area-averaged groundwater percentile.
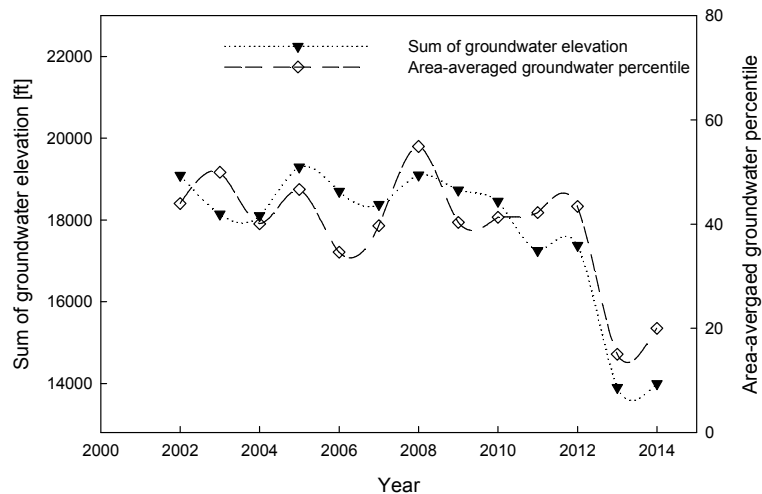


Figure 5.7. Comparison of the area sum of groundwater elevation and the area-averaged groundwater percentile in Prescott, AZ

112

Another graph shows the relationship between the area sum of total rainfall and the area-averaged wetness percentile shown in Fig. 5.8. This shows partial agreement of the trend from 2004 to 2010. In particular, for year in 2013, even though the area sum of total rainfall increased, wetness percentile decreased unlike other periods. Initial periods in 2002 and 2003 seem to contain transient error in the wetness percentile. However, later in the other areas aforementioned, the strong agreement between these two factors will be shown.
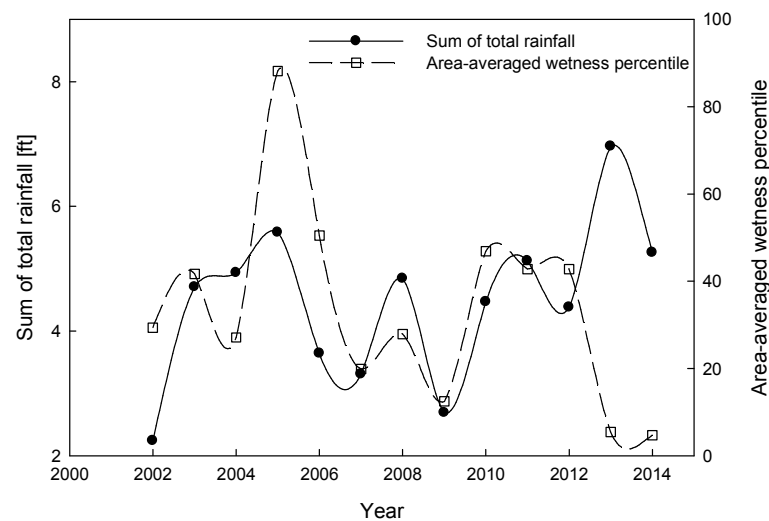


Figure 5.8. Comparison of the area sum of groundwater elevation and the area-averaged wetness percentile in Prescott, AZ

The top 8 cities in a decreasing trend are Deer Valley, Douglas, Luke AFB, Payson, Scottsdale, Fort Huachuca, Williams AFB, and Gila Bend. As shown in Fig. 5.4, the temporal trend in groundwater elevation over the time period in most of the cities in Phoenix AMAs, Pinal AMAs, Tucson AMAs, and Santa Cruz AMAs follows very similar trend. Drastic decline trend occurred during 1940s to 1980s. After 1980, it leveled off or slightly increased. Fort Huachuca and Douglas are in Santa Cruz AMAs. Prescott

was excluded due to violation over 1000 ft difference regarding city investigation, however by the second analysis method we could find that Prescott maintained groundwater elevation in 1980s like other AMAs did up until 2008. However, in recent years, the drastic drop in the groundwater elevation was shown in Fig. 5.6-7. The associated data, sort by alphabetical order of city, are tabulated in Table 5.2.

Table 5.2. Ground Elevation Data Analysis in Arizona

| City | Slope | Data Count | Average | St. Dev. | Median | Mode | Max | Min | Difference |
|---|---|---|---|---|---|---|---|---|---|
| Davis MAFB | -2.26 | 70 | 2,263.96 | 73.71 | 2,276.67 | 2,052.66 | 2,351.97 | 2,052.66 | 299.31 |
| Deer Valley | -5.55 | 63 | 536.22 | 188.99 | 537.00 | 210.40 | 1,001.60 | 210.40 | 791.20 |
| Douglas | -5.46 | 51 | 3,742.52 | 149.16 | 3,687.05 | 3,203.48 | 3,979.40 | 3,203.48 | 775.92 |
| Falcon Field | 0.50 | 66 | 691.67 | 172.55 | 660.30 | 260.70 | 1,046.80 | 260.70 | 786.10 |
| Fort Huachuca | -4.09 | 66 | 3,935.41 | 100.22 | 3,902.52 | 4,043.80 | 4,118.48 | 3,688.48 | 430.00 |
| Gila Bend | -3.80 | 52 | 431.37 | 146.68 | 431.27 | 145.80 | 707.15 | 145.80 | 561.35 |
| Goodyear | 0.04 | 65 | 856.18 | 45.72 | 868.03 | 627.80 | 913.80 | 627.80 | 286.00 |
| Luke AFB | -5.40 | 70 | 518.16 | 153.61 | 478.85 | 268.00 | 926.00 | 268.00 | 658.00 |
| Page | 13.37 | 49 | 3,071.73 | 276.97 | 3,189.93 | 1,986.93 | 3,297.12 | 2386.93 | 910.19 |
| Payson | -5.44 | 39 | 4,669.48 | 154.52 | 4,694.24 | 3,908.60 | 4,860.00 | 3,908.60 | 951.40 |
| Phoenix | -2.92 | 71 | 972.68 | 104.39 | 998.22 | 527.91 | 1,083.26 | 527.91 | 555.34 |
| Safford | 1.30 | 67 | 2,831.51 | 220.20 | 2,869.25 | 2,958.43 | 3,019.06 | 2,077.00 | 942.06 |
| Scottsdale | -5.80 | 54 | 721.54 | 202.87 | 727.33 | 502.50 | 1,009.00 | 311.64 | 697.36 |
| Tucson | -2.26 | 70 | 2,263.96 | 73.71 | 2,276.67 | 2,052.66 | 2,351.97 | 2,052.66 | 299.31 |
| Williams AFB | -4.56 | 69 | 865.32 | 149.60 | 873.17 | 436.74 | 1,127.24 | 436.74 | 690.50 |
| Winslow | -1.01 | 40 | 4,597.24 | 51.60 | 4,602.20 | 4,308.99 | 4,690.00 | 4,308.99 | 381.01 |
| Yuma MCAS | 0.12 | 37 | 92.22 | 18.77 | 97.40 | 26.70 | 126.27 | 26.70 | 99.57 |

In addition, Apache County shows decreasing trend in Fig. 5.9. This County is not included in any AMAs. There is St. Johns which has a power plant. Despite most groundwater measurements were not published to the public, by help of reconstructed groundwater elevations by CS, trends could be investigated. This figure shows decreasing trend in the groundwater and wetness percentile even though the relationship between rainfall and groundwater elevation is not clearly discerned.
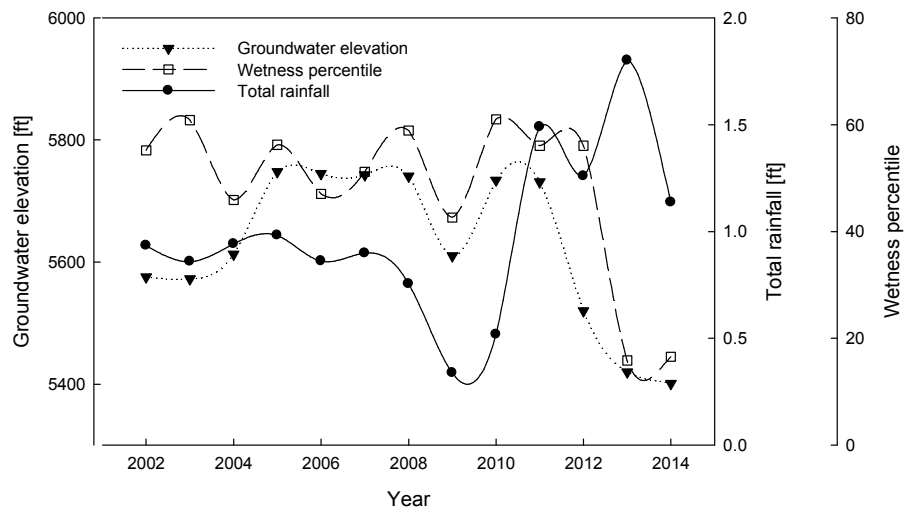
Figure 5.9. Comparison of the deviations in groundwater elevation and groundwater budget along with the average rainfall in Apache County, Arizona, USA

California is the largest state among our regions of interest. An analysis of the groundwater trends in Table 5.1 shows an overall decreasing trend. The trends in groundwater elevation in California fluctuate significantly over time, and the severity of this fluctuation based on trend analysis demands caution with respect to coming to a general conclusion.

An interesting fact was found in accordance with public media attention to heavy groundwater use in Fresno, California. Heavy agricultural regions located in the Central Valley Basin have faced severe warnings of groundwater overuse (Famigliatti 2014). According to this analysis, the groundwater elevation in many regions does show a detrimental decreasing trend, especially in 2013 and 2014. For example, Beaumont in California, which is located on the southern edge of Fresno County, shows a sharp negative trend in Fig. 5.10, with a magnitude of decrease of 480 feet. As side effects, both hydro-compaction and land subsidence are occurring in these heavy groundwater use areas. In Fig. 5.10, a similar pattern of the rise for 2002-2005 can be observed in El

Monte, California in Fig. 5.11. This same pattern of the rise was also observed in many

other southwestern cities of the US such as Fallon NAS, Hawthorne in Nevada,

Beaumont and Lancaster in California, and Ogden in Utah.
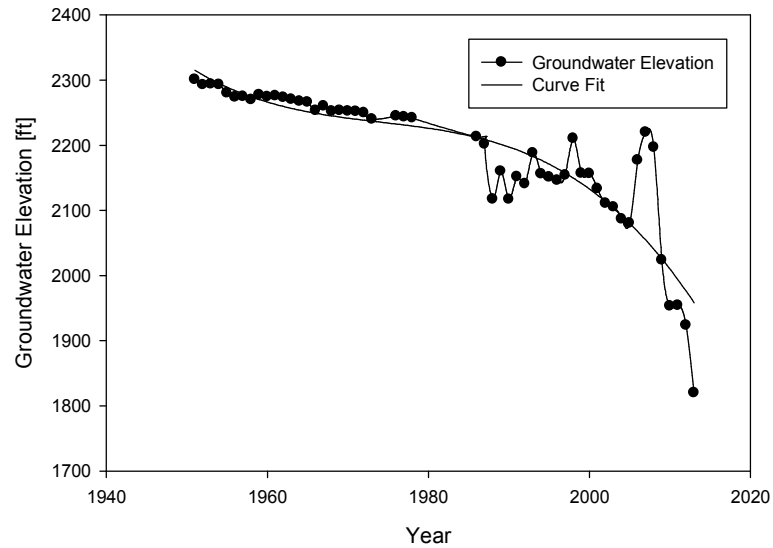


Figure 5.10. Groundwater elevation trend in Beaumont, California, USA
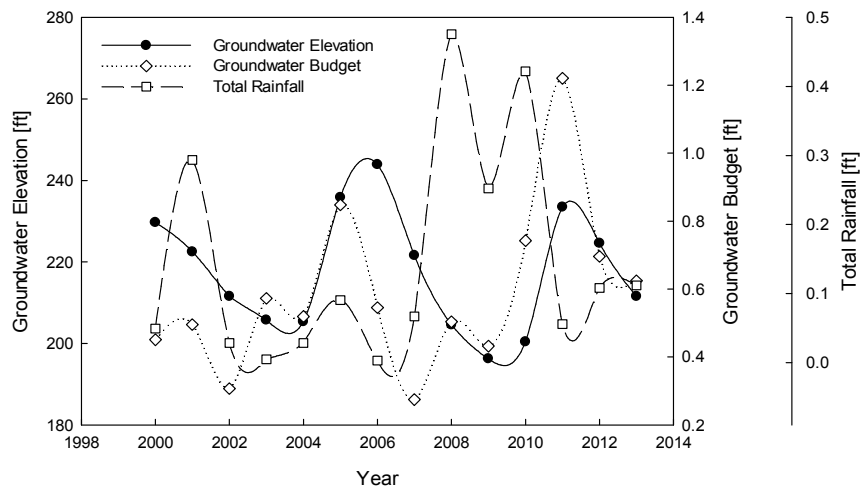


Figure 5.11. Comparison of the groundwater elevation, groundwater budget, and total rainfall in El Monte, CA

For further analysis of the recent groundwater depletion trend in California, the groundwater budget from 2000 to 2014 is used and shown in Fig. 5.12. Note that in 2000, the data for January, February, and March were not published, so that these spans do not include the full year's worth of data; therefore, this figure looks different from the other figures based on lack of data alone. In 2014, the data for October, November, and December were not published either. In comparison with the results data presented for 2000, the groundwater budget in this area has suffered due to insufficiency.

To determine why such a low groundwater budget is shown in 2014, catalogs of accumulated snow in feet, snow melt in feet, and total rainfall intensity in feet are shown in Figs. 5.13-15, respectively. These catalogs are presented to span from 2009 to 2014. Only the winter season is plotted, which extends from November to February. In one row of each figure, the monthly changes of each quantity during the winter are shown.

In the agricultural areas of California, the water supply from the snow pack in the Sierra Nevada Mountains is a critical source during spring and summer, given that rainfall cannot be stored beyond the capacity limit of the region's water reservoirs. During winter, the regions of the Mountains with higher elevation are usually covered with snow. As spring and summer pass, the snow melts and runs through rivers to provide the water supply in the agricultural areas. However, starting in January 2012, the accumulated snow on the mountains has grown lean, as shown in Fig. 5.13. As a result, the amount of snow melt in recent years has been less than historical values, as shown in Fig. 5.14. The bank of water available for use during the hot summer months has disappeared. Instead of snow, rain fell in winter shown in Fig. 5.15. To make matters worse, in 2013 and 2014, very little rain fell as shown in Fig. 5.16.

117
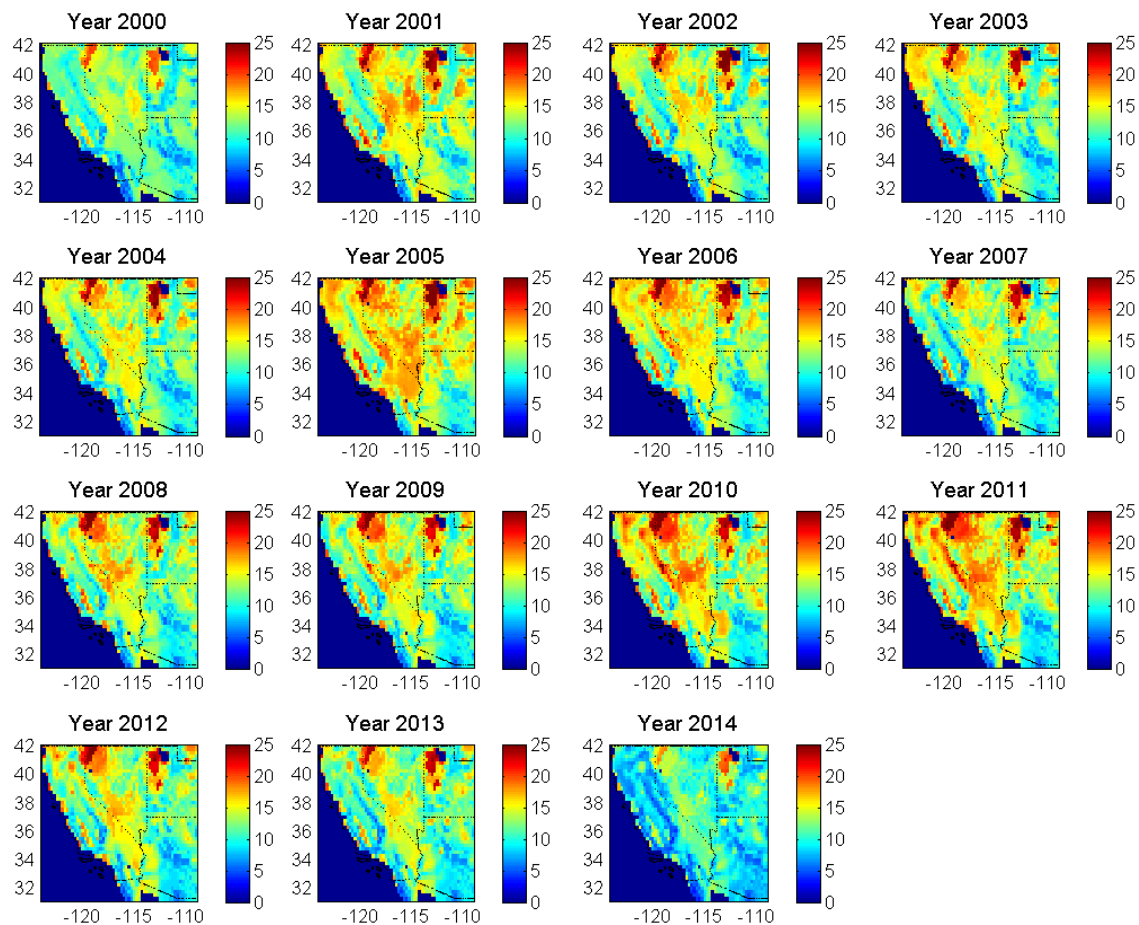
Figure 5.12. Groundwater budget in the southwestern US
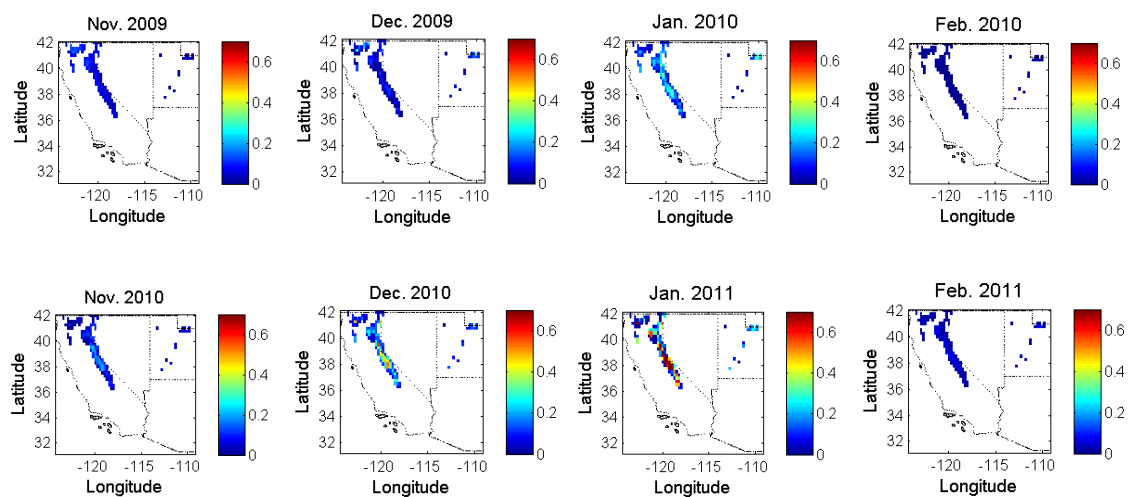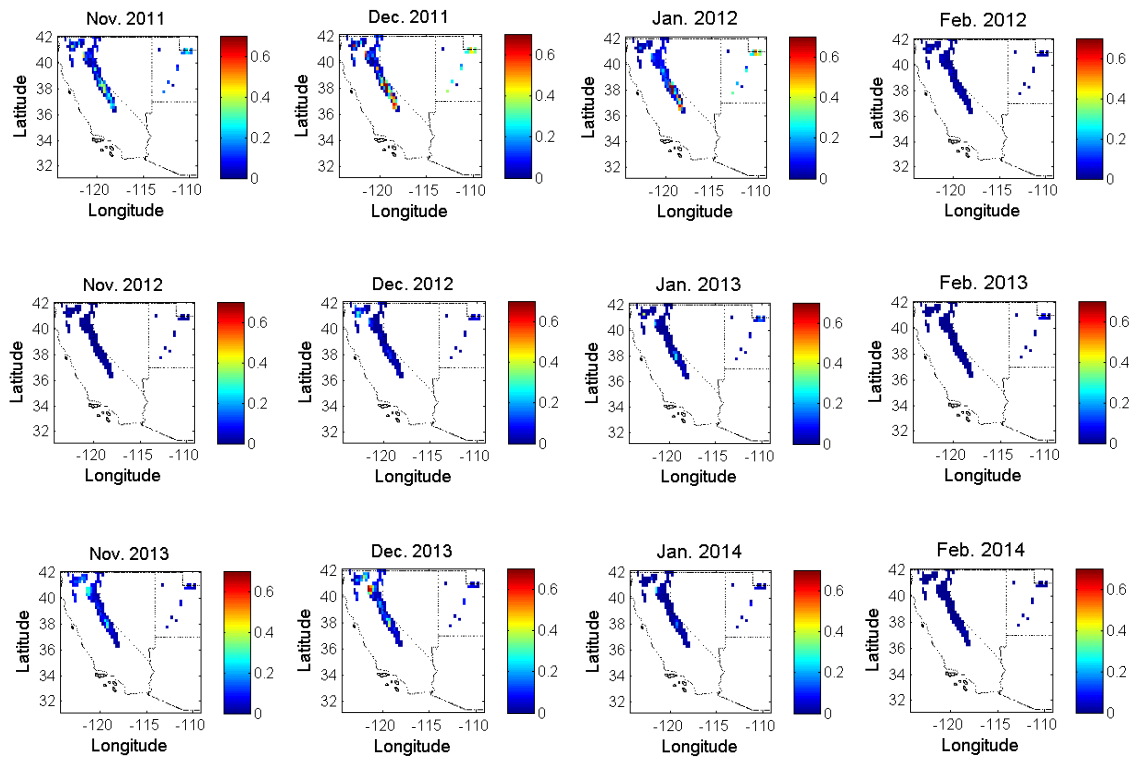
Figure 5.13. Accumulated snow in the Sierra Nevada Mountains, California, USA



119
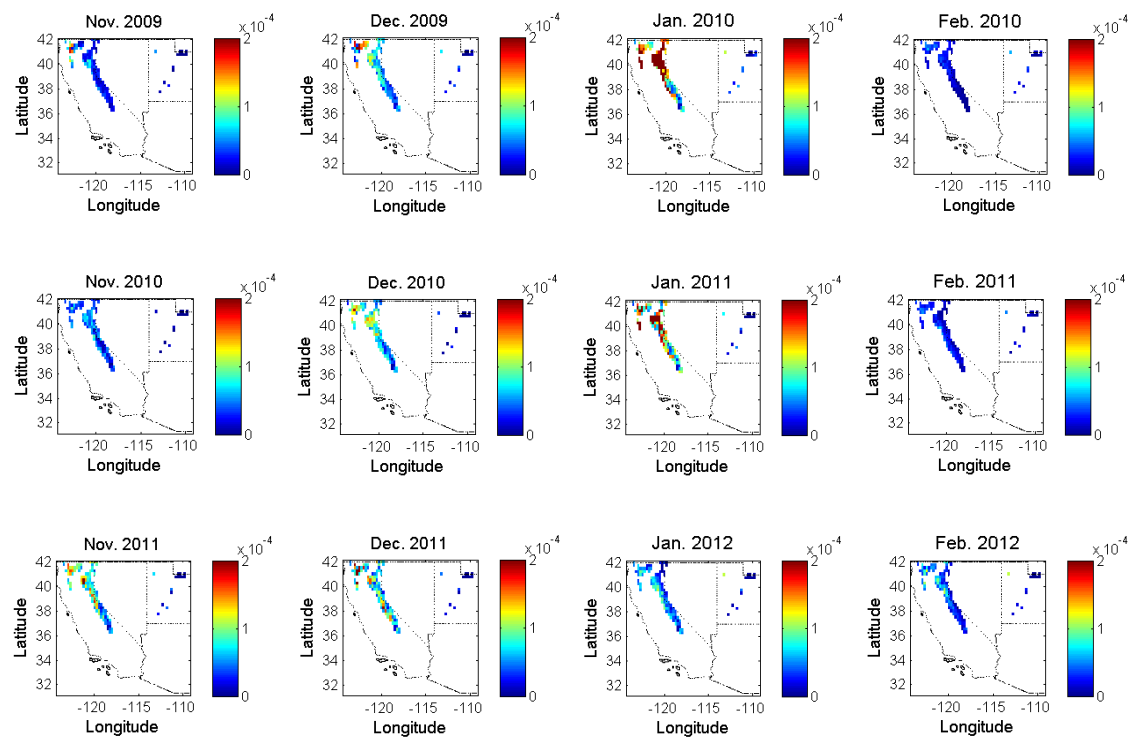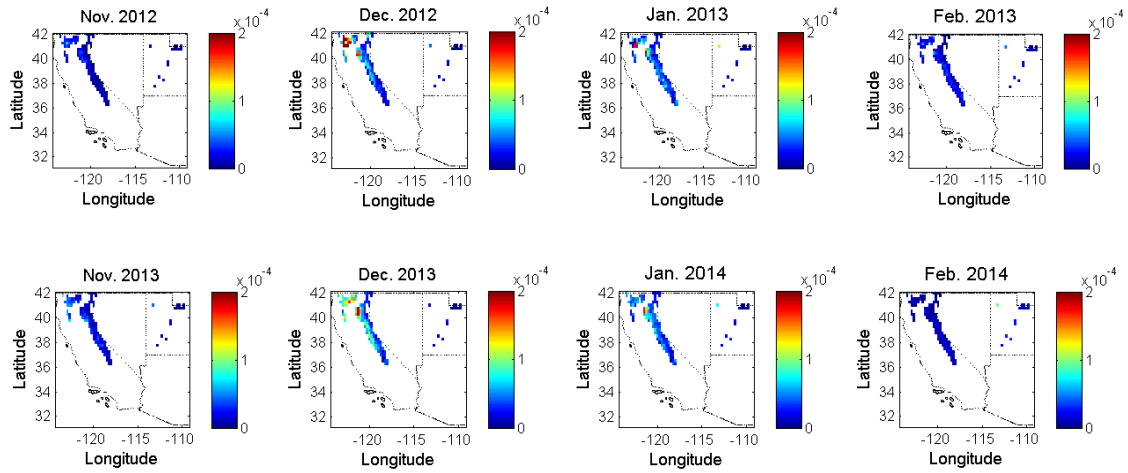
Figure 5.14. Snow melt in the Sierra Nevada Mountains, California, USA
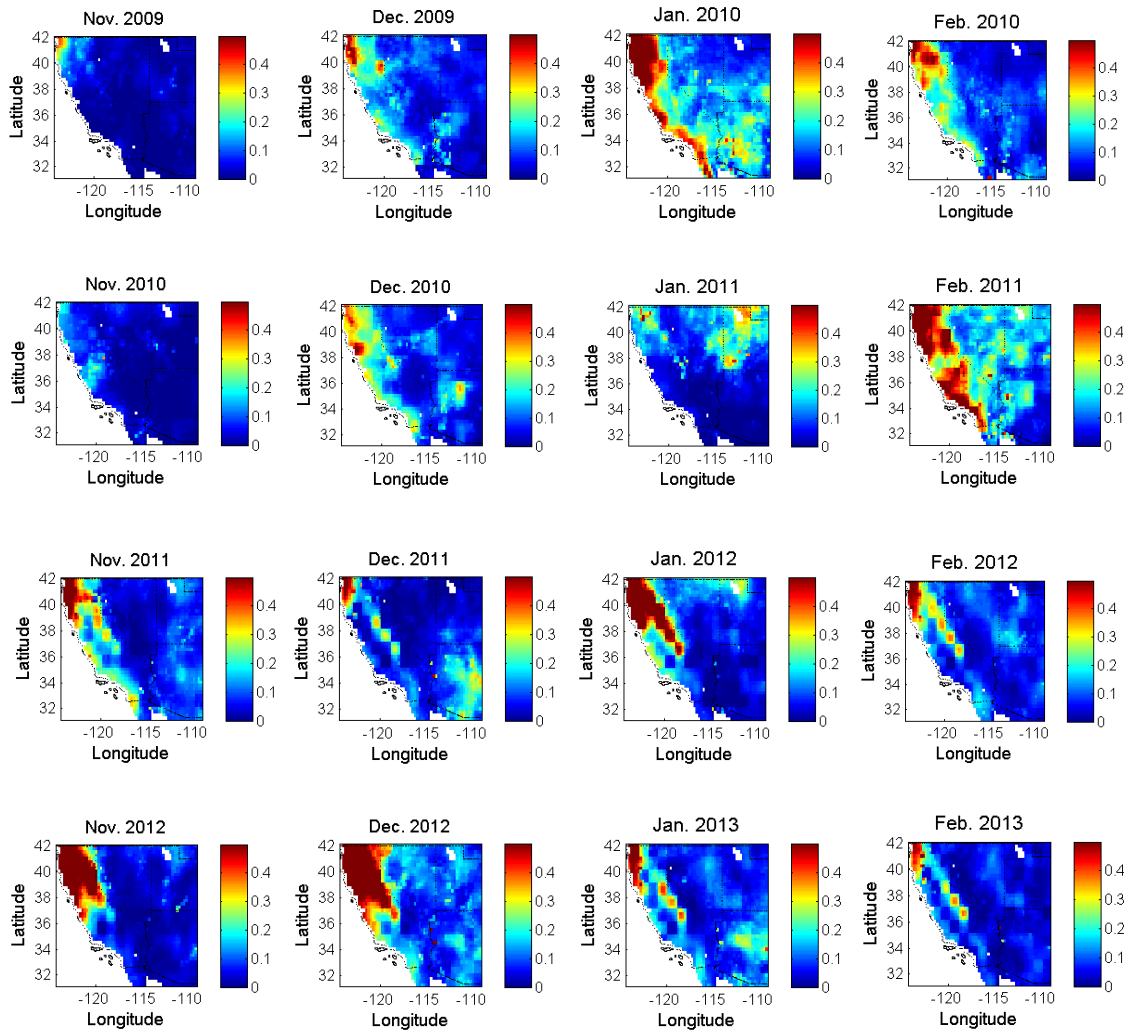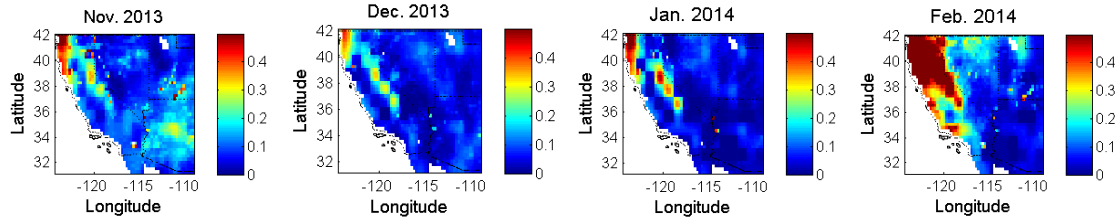
Figure 5.15. Total rainfall in the southwestern US

In Fig. 5.16, for the Central Valley Basins in California, the trend in the area sum of ground elevation matches with sum of groundwater budget, partially during 2005-2011 and 2012-2014. Sum of total rainfall during 2013-2014 was very low as described before.
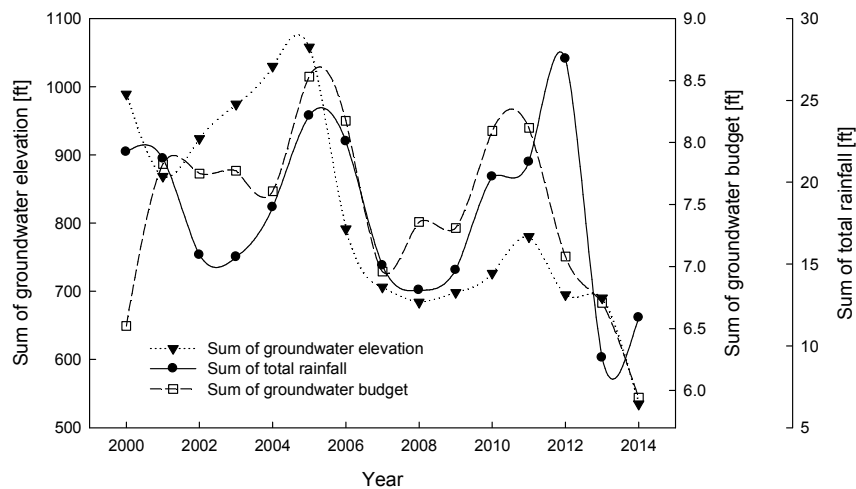


Figure 5.16. Comparison of the area sum of groundwater elevation, groundwater budget, and total rainfall in the Central Valley Basins, CA

The trend in the area sum of accumulated snow matches well with the area sum of snow melt shown in Fig. 5.17. Obviously, once thick snow accumulated, the amount of snow melt should be proportional to its thickness.

121
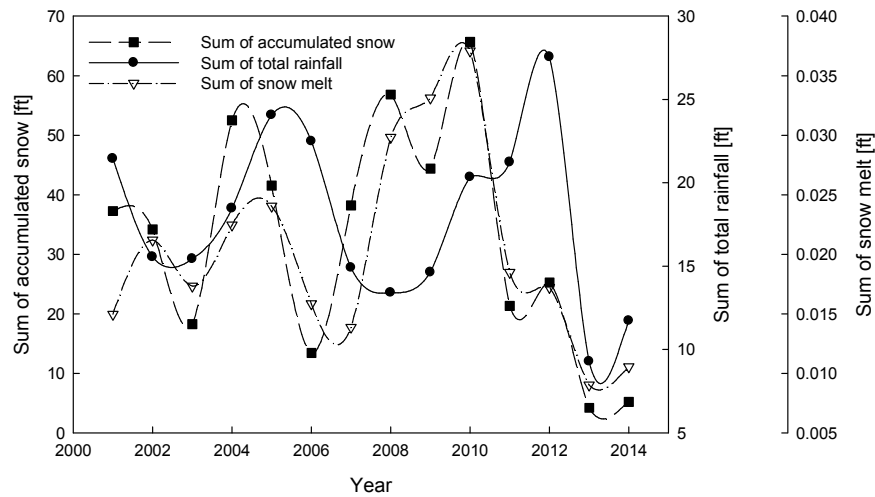
Figure 5.17. Comparison of the area sum of accumulated snow and snow melt in the Sierra Nevada Mountains with the area sum of total rainfall in the Central Valley Basins, CA

   Simple summation between the area sum of accumulated snow in the Sierra Nevada

Mountains and total rainfall in the Central Valley Basins was shown in Fig. 5.18. Once

the sum goes below 35 feet (marked in red dashed line), then it indicates severe drought

in the Central Valley Basins. By monitoring this simple value, we can predict near-future

water use, especially, the sharp increase of groundwater. This unprecedented lack of

water resources made groundwater depleted along with no apparent groundwater

legislative regulation in California.
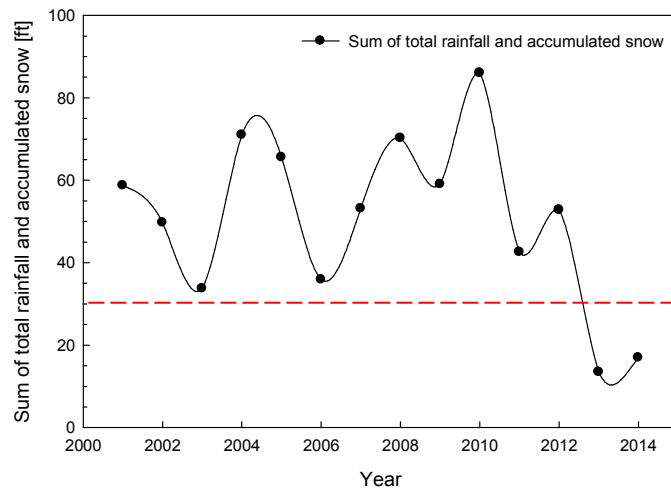
Figure 5.18. The area sum of total rainfall in the Central Valley Basins and accumulated snow in the Sierra Nevada Mountains, CA

In Fig. 5.19, trend in the area sum of groundwater elevation matches well with that in the area-averaged groundwater percentile like other areas in this study.
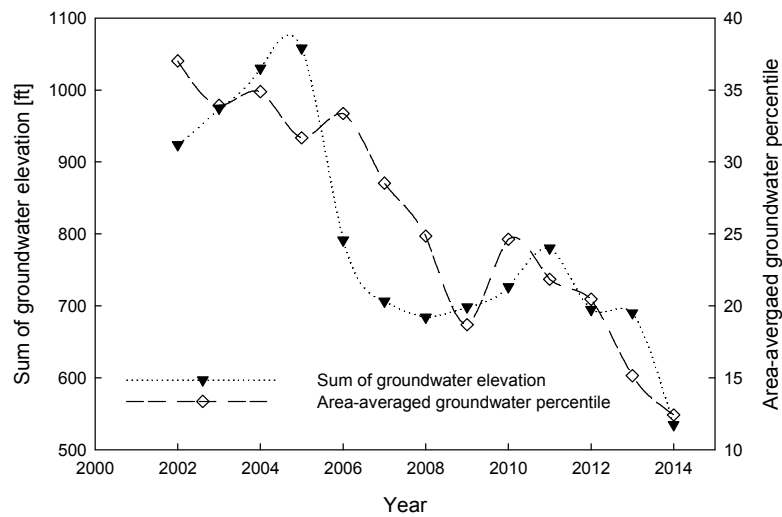


Figure 5.19. Comparison of the area sum of groundwater elevation and the area-averaged groundwater percentile in the Central Valley Basins, CA

123

In Fig. 5.20, the trend in the area sum of total rainfall matches very well with that in the area-averaged wetness percentile. This region heavily depends on precipitation. The effect of total rainfall on wetness percentile is apparently shown.
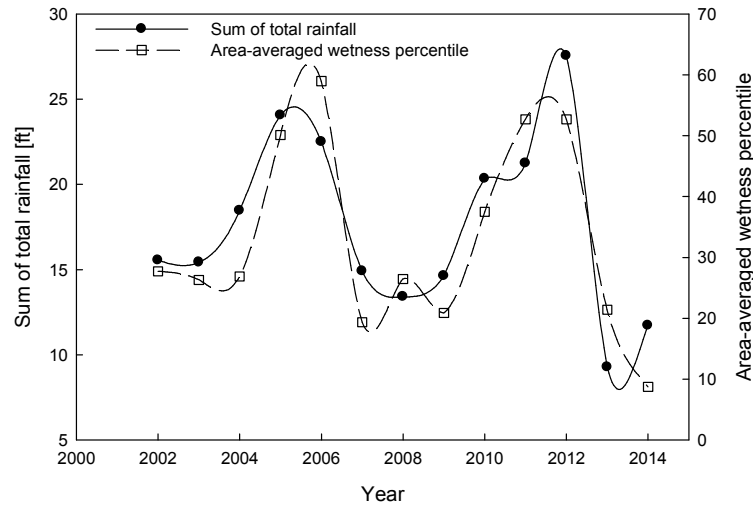


Figure 5.20. Comparison of the area sum of groundwater elevation and the area-averaged wetness percentile in the Central Valley Basins, CA

One important reason for the disappearance of snow is the higher average temperature, as shown in Fig. 5.21. The higher temperature in winter season has also increased the total rainfall shown in Fig. 5.15, although not the snow in Fig. 5.13 in recent years. In Fig. 5.22, trend in temperature in west slopes of the Sierra Nevada Mountains is also shown. Curve fit shows increasing trend in the area-averaged temperature while the sum of accumulated snow is getting lean.

The California government limits the use of surface water to save water for other public purposes, and the penalty for the overuse of surface water is heavy. The only accessible and comparatively inexpensive source of water is from groundwater sources, so that many wells have been drilled to pump water to crops in the agricultural regions

124

because there is no regulation on groundwater in California once the land is owned. As a direct consequence, the groundwater budget and elevation shows the definite decreasing trend.
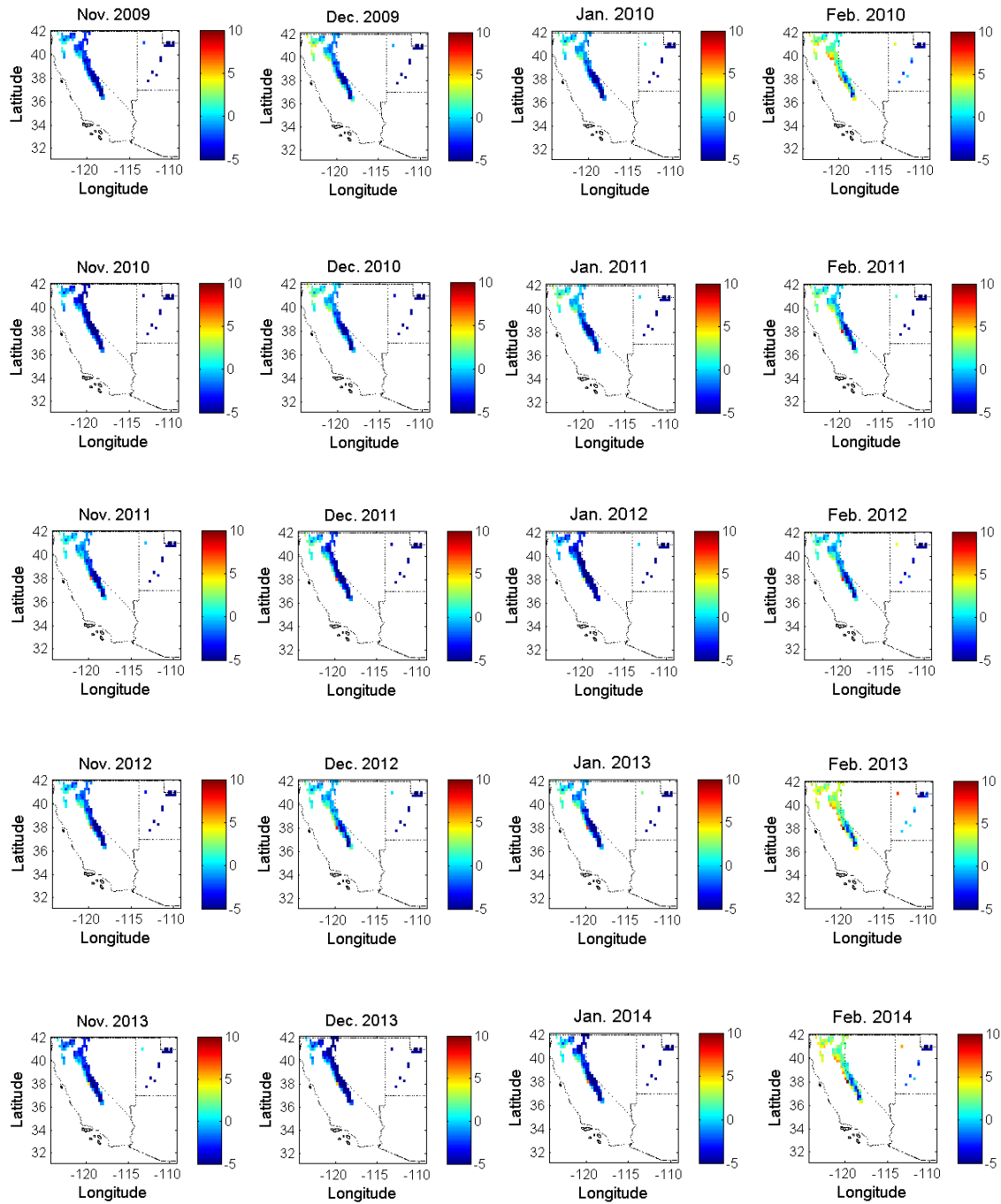


Figure 5.21. Temperature in the Sierra Nevada Mountains, California, USA
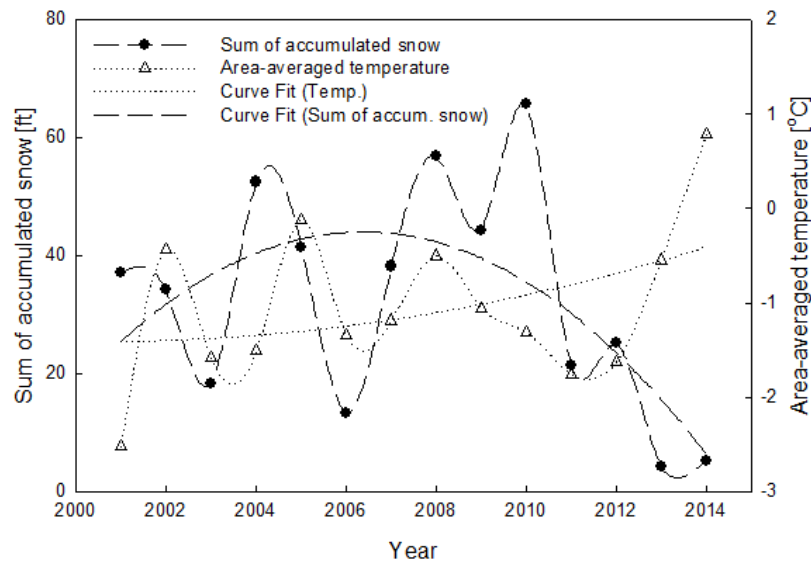
Figure 5.22. Trend in temperature and accumulated snow in the Sierra Nevada Mountains, CA

An analysis of the data recorded for California shows negative trends in the groundwater elevation in the registered wells in Table 5.3. Most of cities in the Central Valley Basins did not pass the filtering process of our trend analysis. USGS and CDWR do not provide historical and periodic data over a long period in that region. From 2002, they started providing hydrographs in some wells. With very limited data, generating reconstructed groundwater elevation was a difficult task. There are huge gaps between data in 1960s and recent data in 2010s. Both groundwater levels and withdrawals must be measured and reported, and importantly, these data must be shared across political boundaries (Famiglietti 2014). Regulations of data request denial between cities and states should be abolished. Even though certain difficulties are present, many regions in the Central Valley Basins were examined in this study. Many such as Chowchilla, Coalinga, etc. show the drastic drop of groundwater elevation in recent years.

Table 5.3. Groundwater Elevation Data Analysis in California

| City | Slope | Data Count | Average | St. Dev. | Median | Mode | Max | Min | Difference |
|---|---|---|---|---|---|---|---|---|---|
| Beaumont | -4.37 | 54 | 2,187.41 | 103.80 | 2,216.36 | 1,819.95 | 2,300.70 | 1,819.95 | 480.75 |
| Bicycle Lake | -1.12 | 47 | 2,278.67 | 26.59 | 2,282.42 | 2,203.36 | 2,296.63 | 2,173.35 | 123.28 |
| Camp Pendleton | -0.18 | 46 | 67.89 | 10.75 | 65.96 | 53.94 | 120.50 | 53.94 | 66.56 |
| China Lake | -0.12 | 48 | 2,179.34 | 6.16 | 2,178.86 | 2,162.19 | 2,193.60 | 2,162.19 | 31.41 |
| Chowchilla | -1.39 | 53 | 80.72 | 27.44 | 85.75 | 87.65 | 135.15 | 16.05 | 119.1 |
| Coalinga | -7.34 | 39 | -41.83 | 60.54 | -51.16 | -52.33 | 43.09 | -133.89 | 176.98 |
| Daggett | -1.99 | 66 | 1,817.02 | 44.37 | 1,820.74 | 1,736.58 | 1,874.35 | 1,736.58 | 137.77 |
| Edwards AFB | -1.35 | 64 | 2,204.60 | 27.38 | 2,201.23 | 2,168.12 | 2,263.52 | 2,168.12 | 95.40 |
| El Monte | -1.13 | 73 | 246.56 | 28.64 | 245.10 | 196.26 | 316.62 | 195.16 | 121.46 |
| Fowler | -1.24 | 39 | 246.93 | 16.68 | 247.20 | 248.90 | 286.80 | 227.70 | 59.10 |
| Fullerton | 1.67 | 52 | 61.85 | 53.48 | 46.72 | -4.57 | 148.22 | -4.57 | 152.79 |
| Fresno | -1.08 | 48 | 255.55 | 26.99 | 268.60 | 281.60 | 287.10 | 204.40 | 82.70 |
| George AFB | -2.96 | 55 | 2,686.28 | 75.26 | 2,709.71 | 2,570.15 | 2,794.67 | 2,570.15 | 224.52 |
| Huron | -2.87 | 42 | -55.18 | 74.12 | -64.19 | -48.6 | 77.75 | -240.28 | 318.03 |
| Kerman | -1.26 | 52 | 133.54 | 33.2 | 130.38 | 208.48 | 223.00 | 59.48 | 163.52 |
| Lake Tahoe | -0.17 | 42 | 6,229.73 | 7.14 | 6,229.91 | 6,208.60 | 6,256.10 | 6,208.60 | 47.50 |
| Lancaster | -1.21 | 73 | 2,239.40 | 33.20 | 2,233.93 | 2,179.25 | 2,336.44 | 2,157.13 | 179.31 |
| Los Banos | -1.38 | 39 | 87.93 | 19.38 | 82.37 | 85.34. | 116.80 | 58.30 | 58.50 |
| Mojave | -0.54 | 61 | 2,426.64 | 13.29 | 2,423.92 | 2,418.22 | 2,474.97 | 2,418.22 | 56.75 |
| Norton AFB | -0.25 | 72 | 932.26 | 31.09 | 933.48 | 876.03 | 1,000.53 | 876.03 | 124.50 |
| Oxnard | -1.07 | 39 | 34.07 | 41.41 | 28.31 | -53.61 | 110.72 | -55.92 | 166.64 |
| Palmdale | -0.54 | 61 | 2,426.64 | 13.29 | 2,423.92 | 2,418.22 | 2,474.97 | 2,418.22 | 56.75 |
| Sacramento | -0.06 | 50 | 9.80 | 4.17 | 9.45 | 9.45 | 18.50 | -7.20 | 25.70 |
| San Diego | -0.10 | 52 | 44.48 | 20.08 | 35.51 | 8.70 | 76.04 | 8.70 | 67.34 |
| San Mateo | 0.26 | 42 | 21.86 | 5.52 | 22.35 | 11.27 | 32.45 | 11.27 | 21.18 |
| Santa Barbara | 1.47 | 72 | 16.28 | 38.95 | 6.26 | -54.39 | 80.22 | -54.39 | 134.61 |
| Santa Maria | -0.04 | 72 | 68.45 | 14.27 | 67.11 | 43.14 | 99.66 | 43.14 | 56.52 |
| Stockton | 0.85 | 52 | -42.76 | 19.59 | -44.35 | -24.65 | -11.79 | -100.30 | 88.51 |
| Travis AFB | 0.40 | 39 | 50.25 | 6.59 | 51.60 | 35.75 | 58.85 | 35.75 | 23.10 |
| Tustin Mcas | -1.01 | 59 | -5.33 | 26.02 | 5.89 | -72.37 | 32.40 | -78.39 | 110.79 |
| Twenty-nine Palm | -2.66 | 58 | 1,979.17 | 112.65 | 1,989.44 | 1,800.84 | 2,243.57 | 1,800.84 | 442.73 |
| Hawthorne | -0.07 | 53 | 4,088.23 | 9.56 | 4,089.79 | 4,090.68 | 4,123.26 | 4,051.54 | 71.72 |

Utah shows negative trends as well with significant fluctuations over the same period as that investigated like in California. Many cities in UT also depend heavily on groundwater. Most of cities in UT did not pass the filtering process of our trend analysis

due to low cardinality like the cities in California did. The associated data are tabulated in Table 5.4.

Table 5.4. Groundwater Elevation Data Analysis in Utah

| City | Slope | Data Count | Average | St. Dev. | Median | Mode | Max | Min | Difference |
|------|-------|-----------|---------|----------|--------|------|-----|-----|-----------|
| Beryl | -1.08 | 67 | 5,094.03 | 21.81 | 5,095.71 | 5,059.45 | 5,127.50 | 5,054.27 | 73.23 |
| Cedar City | -1.44 | 72 | 5,492.64 | 16.17 | 5,491.62 | 5,456.71 | 5,525.69 | 5,456.71 | 68.98 |
| Delta | -0.30 | 71 | 4,613.04 | 9.69 | 4,614.19 | 4,592.07 | 4,634.65 | 4,592.07 | 42.58 |
| Hanksville | -0.91 | 37 | 4308.04 | 13.53 | 4308.10 | 4297.53 | 4350.10 | 4292.00 | 58.10 |
| Hill AFB | -1.51 | 70 | 4,343.02 | 90.77 | 4,322.74 | 4,232.81 | 4,569.55 | 4,232.81 | 336.75 |
| Logan | 0.05 | 72 | 4,464.80 | 4.10 | 4,463.89 | 4,458.60 | 4,476.58 | 4,458.60 | 17.98 |
| Ogden | -1.17 | 72 | 4,280.78 | 20.14 | 4,286.44 | 4,246.73 | 4,335.75 | 4,246.73 | 89.02 |
| Provo | -0.18 | 57 | 4,521.90 | 7.01 | 4,520.98 | 4,510.00 | 4,534.62 | 4,510.00 | 24.62 |
| Saint George | -3.04 | 68 | 2,714.07 | 84.36 | 2,687.48 | 2,606.44 | 2,936.20 | 2,606.44 | 329.76 |
| Salt Lake City | -0.29 | 70 | 4,229.84 | 6.88 | 4,228.83 | 4,223.80 | 4,241.00 | 4,220.27 | 20.73 |
| Tooele | 0.32 | 52 | 4,955.00 | 19.23 | 4,950.38 | 4,949.14 | 5,032.95 | 4,941.65 | 91.30 |

According to the US Census Bureau, St. George in Utah is the second fastest-growing metropolitan area in the US. This trend continued through 2007, and then after 2007 it has slowed significantly. The overall decrease in groundwater stopped in 1970, and then groundwater elevation gained several feet, increasing to approximately 2750 feet before decreasing in 1982. One observation which needs to mention is that in 2005, the high groundwater elevation measurement, which increased beginning in January 2005, was due to a historical flood. This trend is shown in Fig. 5.23.
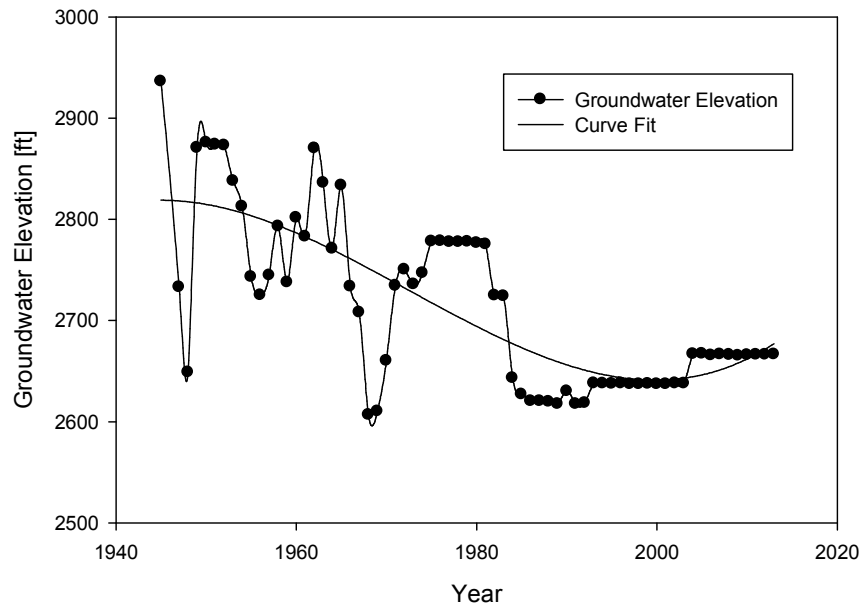
Figure 5.23. Trend of groundwater elevation in St. George, Utah, USA

In Fig. 5.24, the trend in the area sum of ground elevation shows a partial match during 2010-2014 with that in the sum of groundwater budget. The Beryl-Enterprise area has shown the continual decrease in the groundwater elevation since 1942 shown in Fig. 5.25. According to the Beryl Enterprise Groundwater Management Plan, the current average groundwater depletion is estimated at about 65,000 acre-feet per year and the safe yield has been determined to be about 34,000 acre-feet per year (Styler and Jones 2012). This plan projected 5% reduction of groundwater withdrawals in next 10 years and its time frame spans 120 years to achieve total reduction amount. It has not shown any successful implementation at all. As demonstrated in Fig. 5. 4 in Phoenix, Arizona, at least 10 years we should keep monitoring its groundwater elevation for verification of success in the groundwater management act.

Figure 5.24. Comparison of the area sum of groundwater elevation, groundwater budget, and total rainfall in the Beryl-Enterprise area, UT
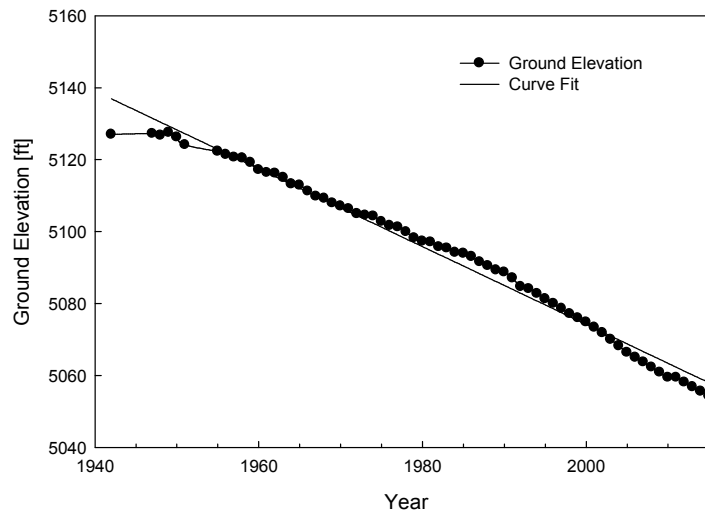


Figure 5.25. Trend in groundwater elevation in the Beryl-Enterprise area, UT

In Fig. 5.26, trend in the area sum of groundwater elevation matches very well with the area-averaged groundwater percentile, as well.

Figure 5.26. Comparison of the area sum of groundwater elevation and the area-averaged groundwater percentile in the Beryl-Enterprise area, UT

In Fig. 5.27, the trend in the area sum of total rainfall shows near perfect matches with the area-averaged wetness percentile. In this region, it also heavily depends on precipitation due to no supply from surface water. Total rainfall impacts on wetness percentile apparently. The highest peaks in both quantities were found in 2005 and 2011.



Figure 5.27. Comparison of the area sum of groundwater elevation and the area-averaged wetness percentile in the Beryl-Enterprise area, UT

131

For Nevada, an analysis of the data shows negative trends over most of cities and tabulated in Table 5.5. Nevada also noticed heavy use of groundwater in 1960s so Nevada water department initiated groundwater management program for several regions. Unless it was performed successfully, the trend would be worse.

Table 5.5. Groundwater Elevation Data Analysis in Nevada

| City | Slope | Data Count | Average | St. Dev. | Median | Mode | Max | Min | Difference |
|------|-------|-----------|---------|----------|--------|------|-----|-----|-----------|
| Austin | 3.43 | 41 | 5,924.81 | 189.99 | 5,999.30 | 6,000.99 | 6,001.83 | 5,253.20 | 748.63 |
| Battle Mtn | 0.11 | 37 | 4,515.54 | 10.22 | 4,514.66 | 4,477.40 | 4,526.98 | 4,477.40 | 49.58 |
| Caliente | -4.73 | 39 | 4,407.01 | 99.01 | 4,375.98 | 4,341.90 | 4,782.30 | 4,341.90 | 440.40 |
| Ely Yelland | -2.42 | 56 | 6,222.69 | 68.55 | 6,220.24 | 6,130.32 | 6,412.43 | 6,130.32 | 282.11 |
| Fallon NAS | -0.10 | 43 | 3,927.68 | 7.59 | 3,927.98 | 3,912.30 | 3,947.90 | 3,912.30 | 35.60 |
| Indian Springs | -0.45 | 36 | 3051.05 | 59.11 | 3077.72 | 2926.91 | 3123.58 | 2926.91 | 196.67 |
| Las Vegas | -1.34 | 70 | 2,080.28 | 59.59 | 2,091.68 | 1,715.65 | 2,149.96 | 1,715.65 | 434.32 |
| Mercury | -1.10 | 38 | 2,384.61 | 24.96 | 2,377.56 | 2,416.00 | 2,416.00 | 2,282.90 | 133.10 |
| Nellis AFB | -1.27 | 50 | 1,762.77 | 35.13 | 1,748.52 | 1,702.10 | 1,863.40 | 1,702.10 | 161.30 |
| Reno | -0.92 | 49 | 4,429.01 | 35.32 | 4,418.85 | 4,363.30 | 4,535.20 | 4,363.30 | 171.90 |
| Winnemucca | 0.04 | 50 | 4,286.21 | 6.70 | 4,285.71 | 4,274.10 | 4,301.25 | 4,274.10 | 27.15 |

Caliente is a very small town with a total population of 1,130 people. Even though Caliente has stream flow from the Meadow Valley Wash, until 1970, groundwater in this region was heavily used, but since 1970, its level has been well maintained. This finding is shown in Fig. 5.28. The practice of measuring the groundwater level in this area was discontinued in 1999.

132
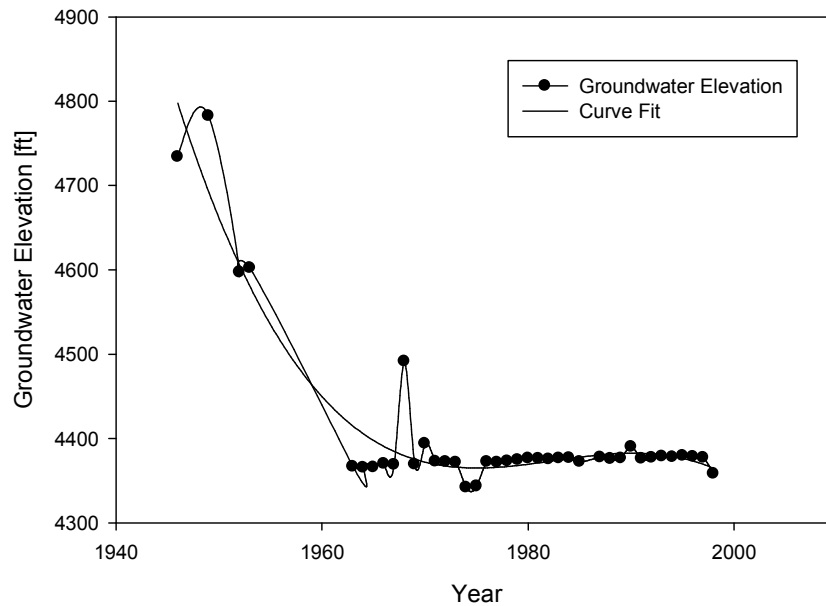
Figure 5.28. Trend of the groundwater elevation in Caliente, Nevada, USA

In Fig. 5.29, the trend in the area sum of ground elevation does not match even partially with that in the sum of groundwater budget. The reason is that the Las Vegas Groundwater Management Program was initiated in early 1970s; artificial water has been recharged to the wells. In results, groundwater elevations have been rising in the long-term since 1990. Artificial recharge has indirectly helped gaining back groundwater elevations in many parts of the basin. Since 1988, more than 300,000 acre-feet of water have been added back into the groundwater supply (Johnson et al. 1997)
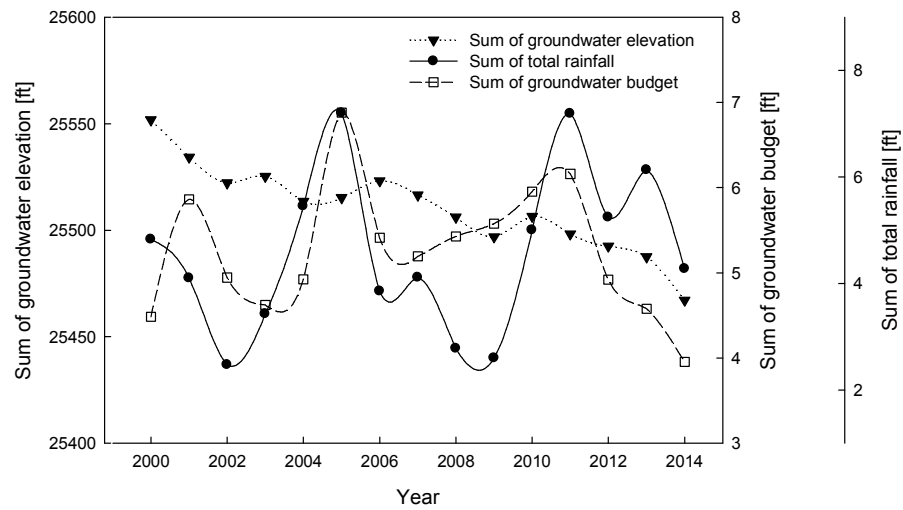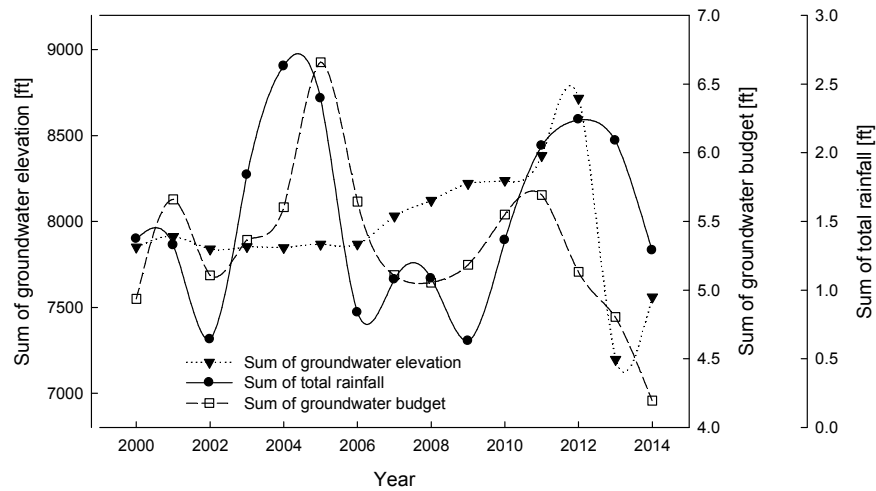
Figure 5.29. Comparison of the area sum of groundwater elevation, groundwater budget, and total rainfall in Las Vegas, NV

In Fig. 5.30 trend in groundwater elevation did not match with that in groundwater

percentile. The reason is due to successful artificial recharge program.
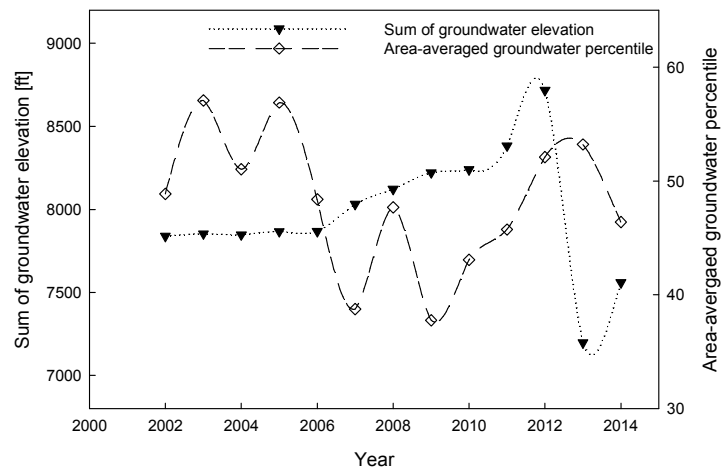


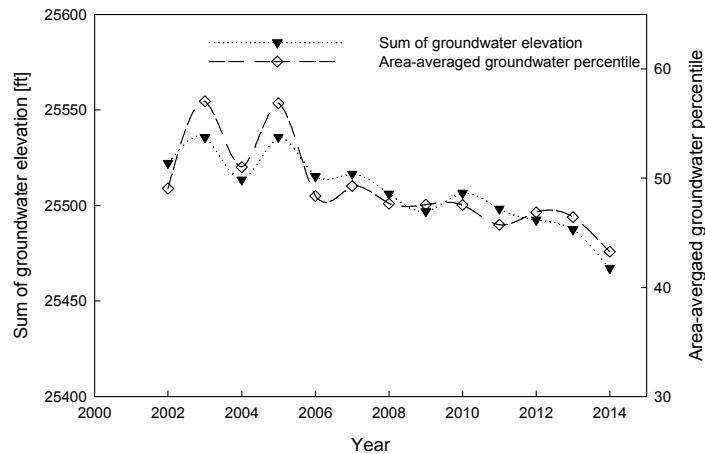Figure 5.30. Comparison of the area sum of groundwater elevation and the area-averaged groundwater percentile in Las Vegas, NV

In Fig. 5.31, the trend in the area sum of total rainfall matches well with the area-

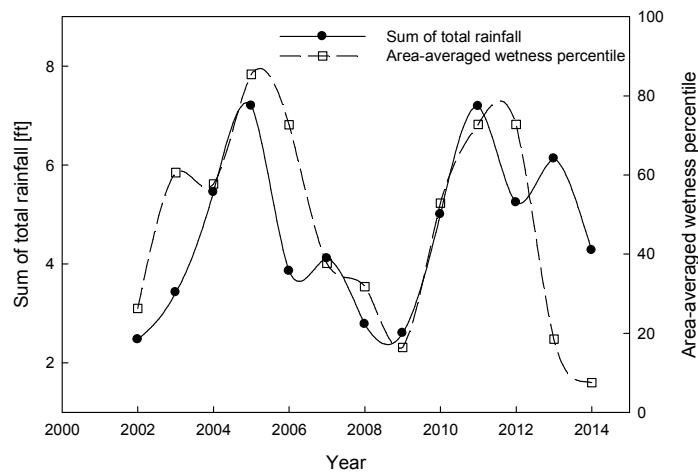averaged wetness percentile. In this region, the effect of total rainfall on wetness

percentile is apparently shown.

134
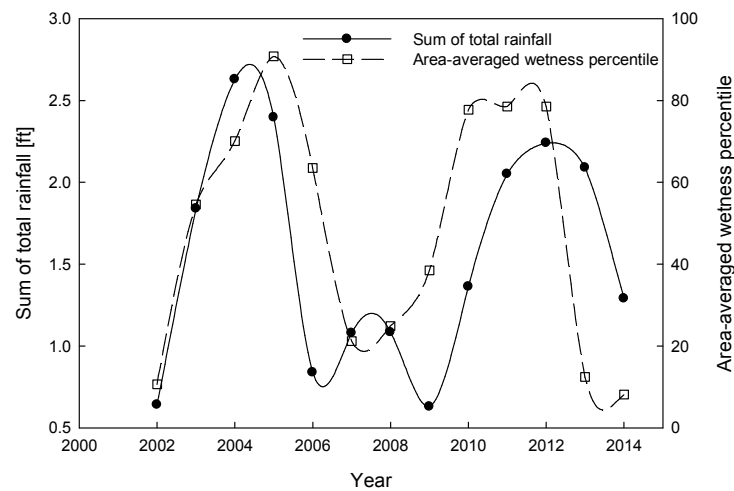
Figure 5.31. Comparison of the area sum of groundwater elevation and the area-averaged wetness percentile in Las Vegas, NV

Table 5.6 shows the results of analyses about the trends in wells in the southwestern states using a categorized 10-year period bucket. A decreasing trend grows increasingly prominent over time. Only two time buckets, the ranges from 1985–1994 and 1995–2004, show that the ratio of decreasing groundwater elevation in wells also decreased similarly throughout the southwestern US. In Fig. 5.32, Arizona exhibits a noticeable rise in the trend of decreasing well resources, based on an initial value of approximately 10 % in the first year range from 1942 to 1949 and a final value of 54.97 % in the latter year range. The trends observed for Nevada and California are very similar to that of Arizona. In California, recent drought has impacted the decreasing trend severely. Meanwhile, Utah exhibits drastic fluctuations in the overall decreasing trend, with peak values in 1975– 1984.

135
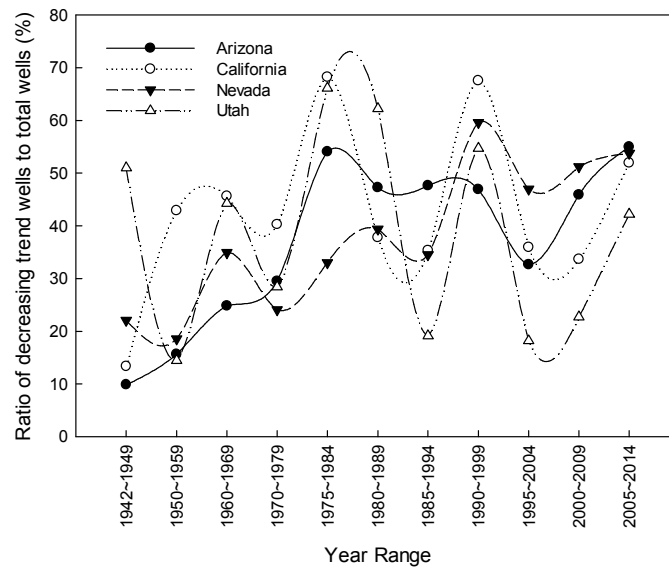
Figure 5.32. Trend analysis of the decreasing groundwater elevation wells in the southwestern US

Table 5.6. Results of Analyses in Trends of Wells in the Southwestern US

| State | Year Range | Decreasing | Ratio (%) | Increasing | Ratio (%) | Total No. of Wells |
|---|---|---|---|---|---|---|
| California | 1942–1949 | 70 | 13.36 | 454 | 86.64 | 524 |
| | 1950–1959 | 553 | 42.87 | 737 | 57.13 | 1290 |
| | 1960–1969 | 701 | 45.61 | 836 | 54.39 | 1537 |
| | 1970–1979 | 709 | 40.24 | 1053 | 59.76 | 1762 |
| | 1975–1984 | 1344 | 68.22 | 626 | 31.78 | 1970 |
| | 1980–1989 | 624 | 37.77 | 1028 | 62.23 | 1652 |
| | 1985–1994 | 528 | 35.32 | 967 | 64.68 | 1495 |
| | 1990–1999 | 1160 | 67.52 | 558 | 32.48 | 1718 |
| | 1995–2004 | 665 | 35.93 | 1186 | 64.07 | 1851 |
| | 2000–2009 | 681 | 33.66 | 1342 | 66.34 | 2023 |
| | 2005–2014 | 1355 | 51.92 | 1255 | 48.08 | 2610 |
| Arizona | 1942–1949 | 48 | 9.86 | 439 | 90.14 | 487 |
| | 1950–1959 | 200 | 15.63 | 1080 | 84.38 | 1280 |
| | 1960–1969 | 358 | 24.81 | 1085 | 75.19 | 1443 |
| | 1970–1979 | 331 | 29.50 | 791 | 70.50 | 1122 |
| | 1975–1984 | 647 | 54.05 | 550 | 45.95 | 1197 |
| | 1980–1989 | 764 | 47.25 | 853 | 52.75 | 1617 |
| | 1985–1994 | 822 | 47.60 | 905 | 52.40 | 1727 |
| | 1990–1999 | 849 | 46.91 | 961 | 53.09 | 1810 |
| | 1995–2004 | 640 | 32.65 | 1320 | 67.35 | 1960 |
| | 2000–2009 | 1000 | 45.89 | 1179 | 54.11 | 2179 |
| | 2005–2014 | 1278 | 54.97 | 1047 | 45.03 | 2325 |
| Nevada | 1942–1949 | 19 | 22.09 | 67 | 77.91 | 86 |
| | 1950–1959 | 28 | 18.54 | 123 | 81.46 | 151 |
| | 1960–1969 | 125 | 34.92 | 233 | 65.08 | 358 |
| | 1970–1979 | 215 | 24.08 | 678 | 75.92 | 893 |
| | 1975–1984 | 321 | 33.02 | 651 | 66.98 | 972 |
| | 1980–1989 | 316 | 39.35 | 487 | 60.65 | 803 |
| | 1985–1994 | 295 | 34.50 | 560 | 65.50 | 855 |
| | 1990–1999 | 662 | 59.59 | 449 | 40.41 | 1111 |
| | 1995–2004 | 406 | 46.94 | 459 | 53.06 | 865 |
| | 2000–2009 | 489 | 51.20 | 466 | 48.80 | 955 |
| | 2005–2014 | 694 | 53.76 | 597 | 46.24 | 1291 |

136

| | | | | | |
|---|---|---|---|---|---|
| | 1942–1949 | 185 | 50.96 | 178 | 49.04 | 363 |
| | 1950–1959 | 75 | 14.48 | 443 | 85.52 | 518 |
| | 1960–1969 | 441 | 44.23 | 556 | 55.77 | 997 |
| | 1970–1979 | 315 | 28.40 | 794 | 71.60 | 1109 |
| | 1975–1984 | 739 | 66.10 | 379 | 33.90 | 1118 |
| Utah | 1980–1989 | 712 | 62.24 | 432 | 37.76 | 1144 |
| | 1985–1994 | 221 | 19.15 | 933 | 80.85 | 1154 |
| | 1990–1999 | 614 | 54.67 | 509 | 45.33 | 1123 |
| | 1995–2004 | 195 | 18.19 | 877 | 81.81 | 1072 |
| | 2000–2009 | 235 | 22.71 | 800 | 77.29 | 1035 |
| | 2005–2014 | 425 | 42.16 | 583 | 57.84 | 1008 |

We found that trend in ratio of decreasing trend wells in Arizona shows very similar trend in rate of groundwater depletion in the US over 10-year periods in Fig. 5.33. Annual rates of total groundwater depletion in the US through 1940 were less than 4 km$^3$/year, but after mid 1940s, increased significantly (Konikow 2013). Its peak occurred during the last period. This pattern could be found in our trend in ratio of decreasing trend wells in Arizona. The volume of groundwater depletion over 1900-2008 period by the Alluvial Basin within which Arizona lies is 102 km$^3$ out of total 992.2 km$^3$ in the US, ranked fourth after the High Plains Aquifer (340.9 km$^3$), the Mississippi embayment aquifer (182 km$^3$) and the Central Valley Basin (144.8km$^3$) (Konikow 2013).

The greatest annual rates of groundwater depletion occurred during 2001 to 2002 and average annual rates of groundwater depletion increased substantially after 2000 (Konikow 2013). This can explain why the ratio of decreasing trend wells increased after 2000 in all four states.
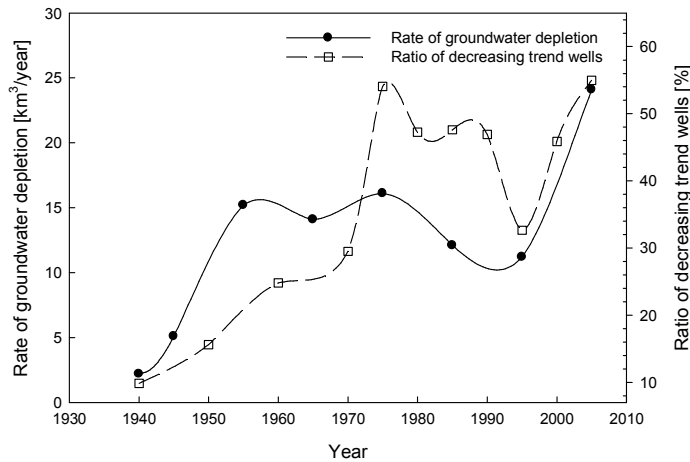
Figure 5.33. Comparison of trends in ratio of decreasing trend wells in Arizona and ratio of groundwater depletion in the US

Finally, a catalog of groundwater contour using data by the CS method over the period from 1942 to 2014 is shown below in Figs. 5.34-43. This catalog shows the general trends of groundwater elevation on a yearly basis. This contour shows topological groundwater elevation in the southwestern US. Differences from land elevation were made because the regions, in which human beings could not live such as high altitude region in Sierra Nevada Mountains, do not have any measurement. Therefore, the boundaries between California and Nevada did not show gradual but sharp contour level change from 0 to 4000.

While investigating Arizona groundwater elevation change from 1940s to 1990s, we discovered that the low contour levels had been expanding along with areas in the AMAs up to mid 1980s, after then, those was reduced significantly.

138
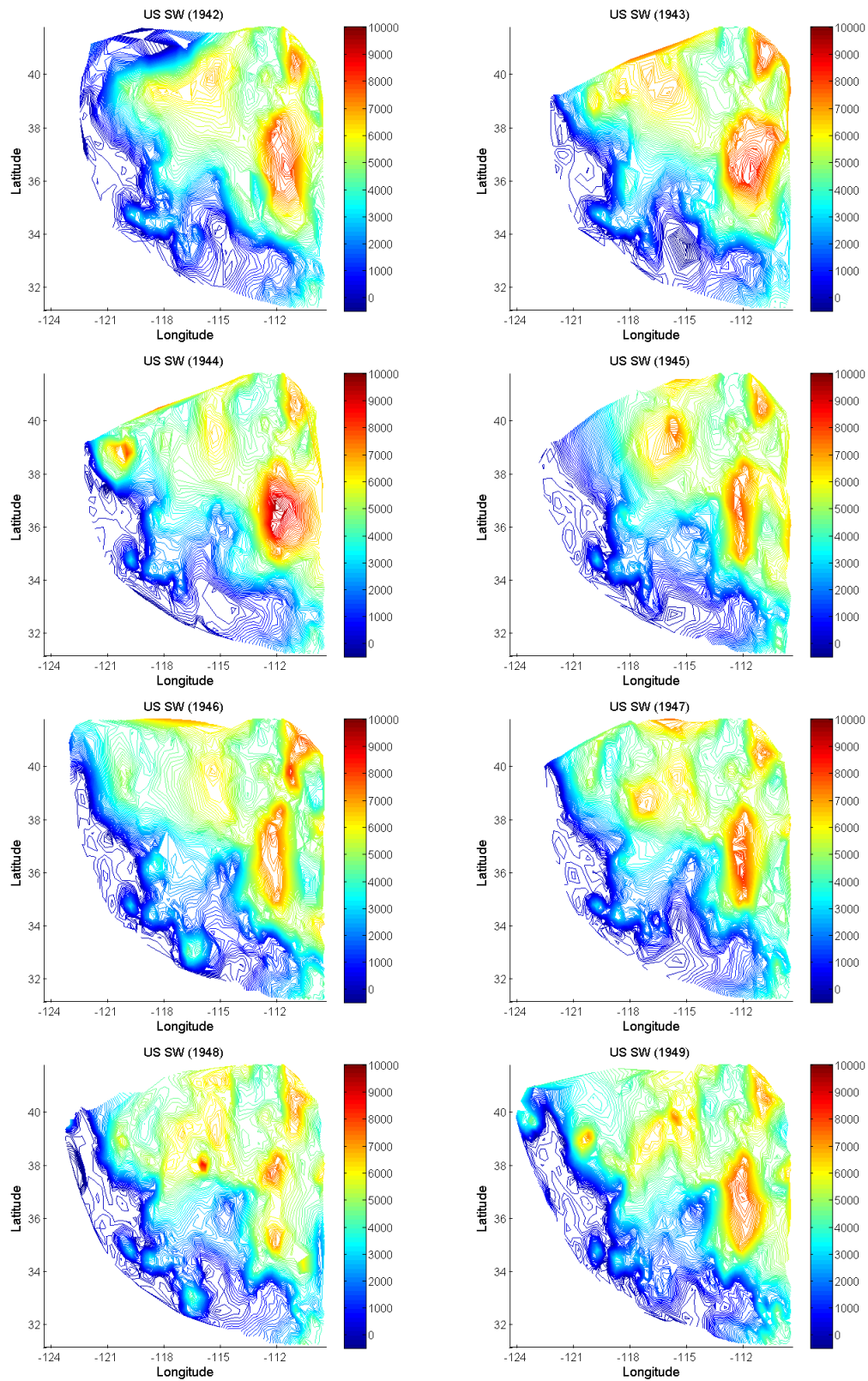
Figure 5.34. Compressed sensing groundwater network data from 1942 to 1949
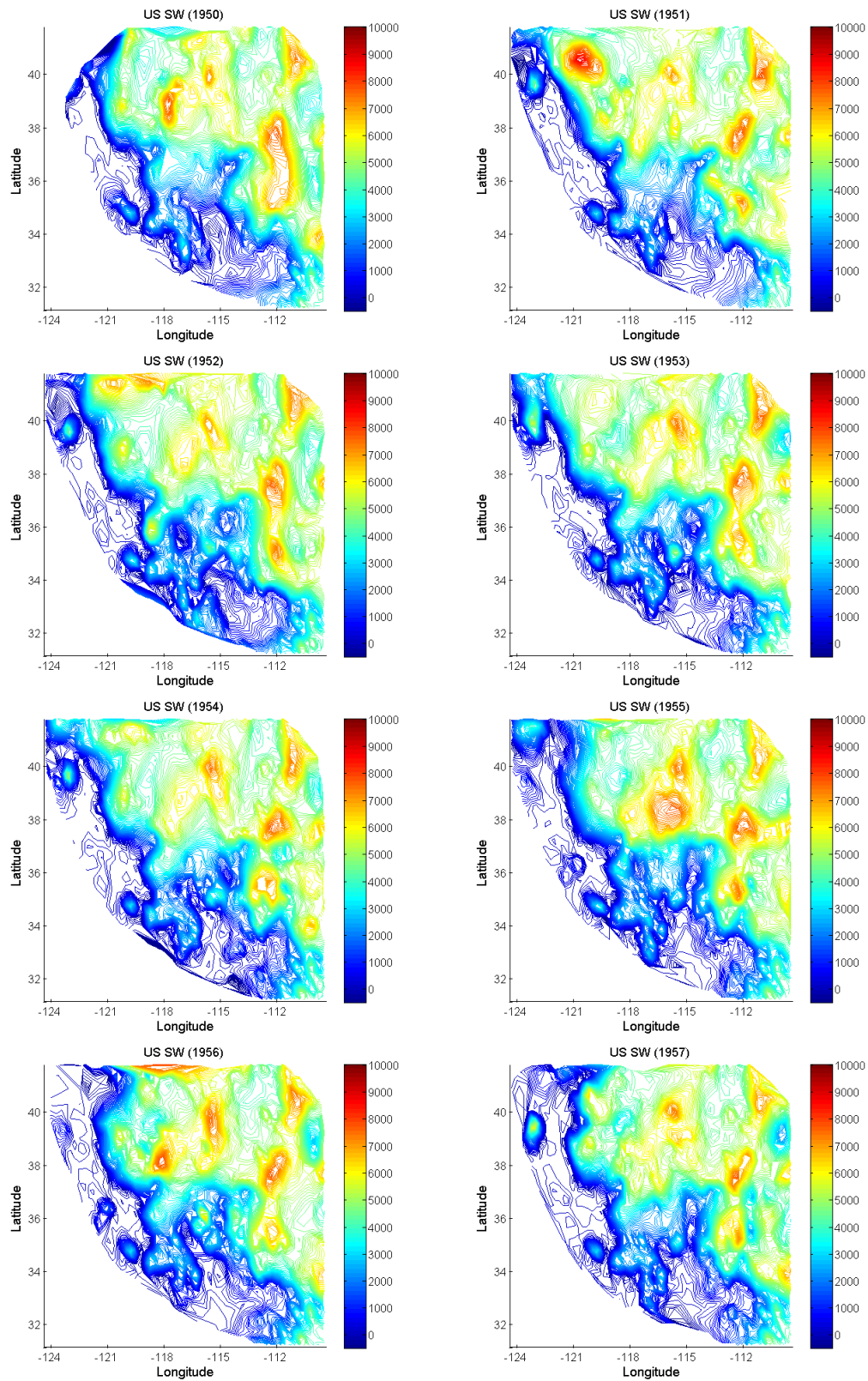
Figure 5.35. Compressed sensing groundwater network data from 1950 to 1957
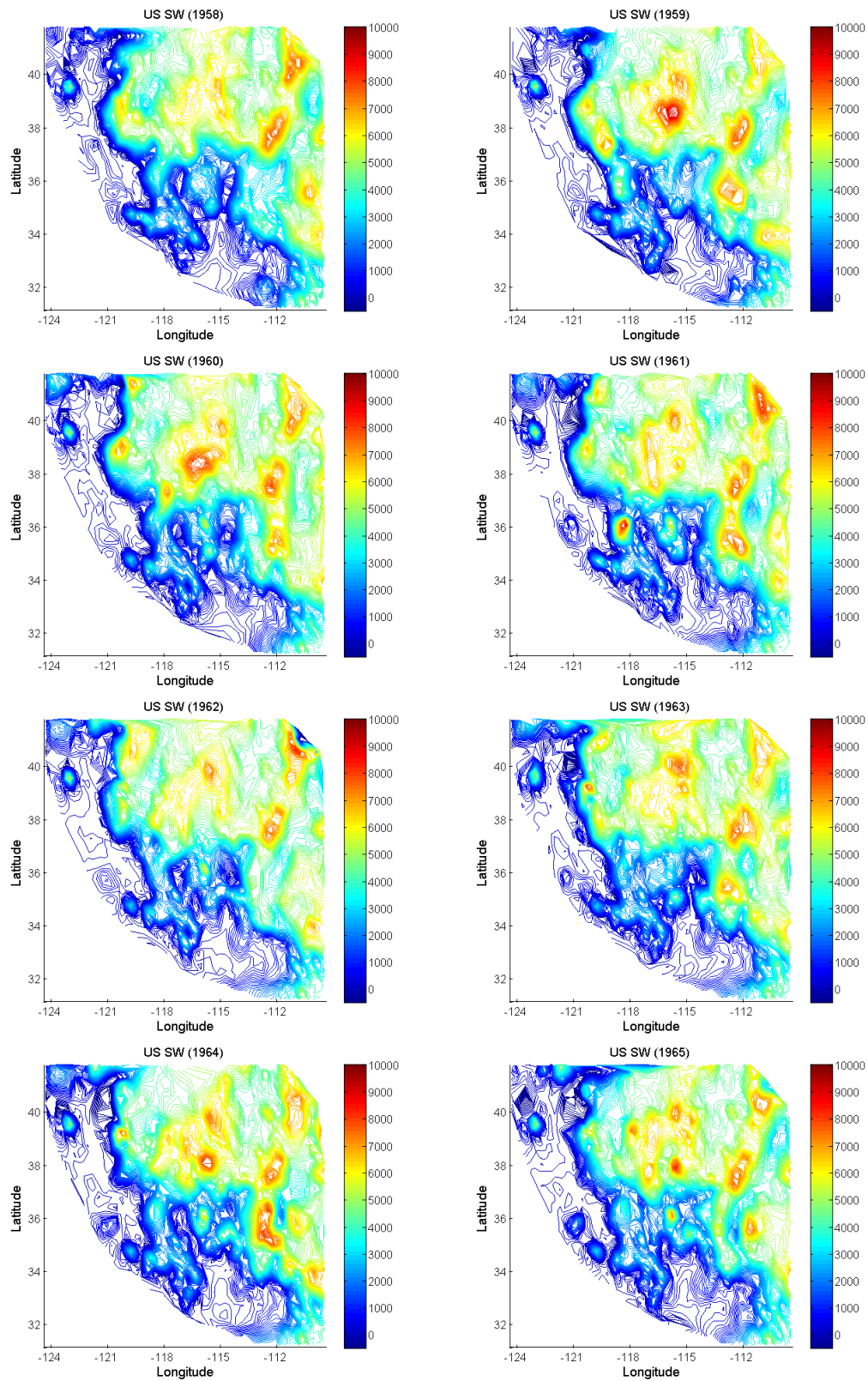
Figure 5.36. Compressed sensing groundwater network data from 1958 to 1965
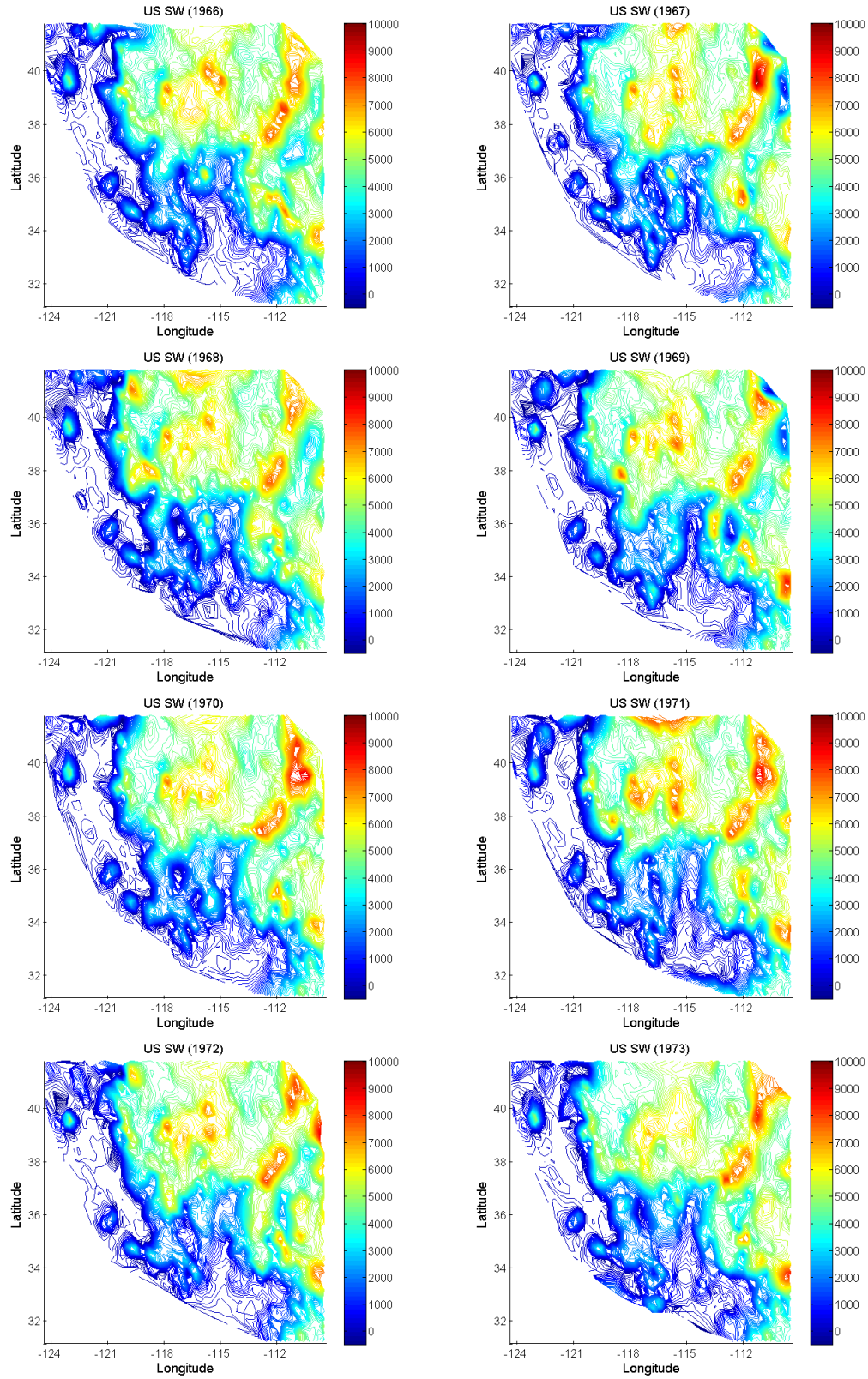
Figure 5.37. Compressed sensing groundwater network data from 1966 to 1973
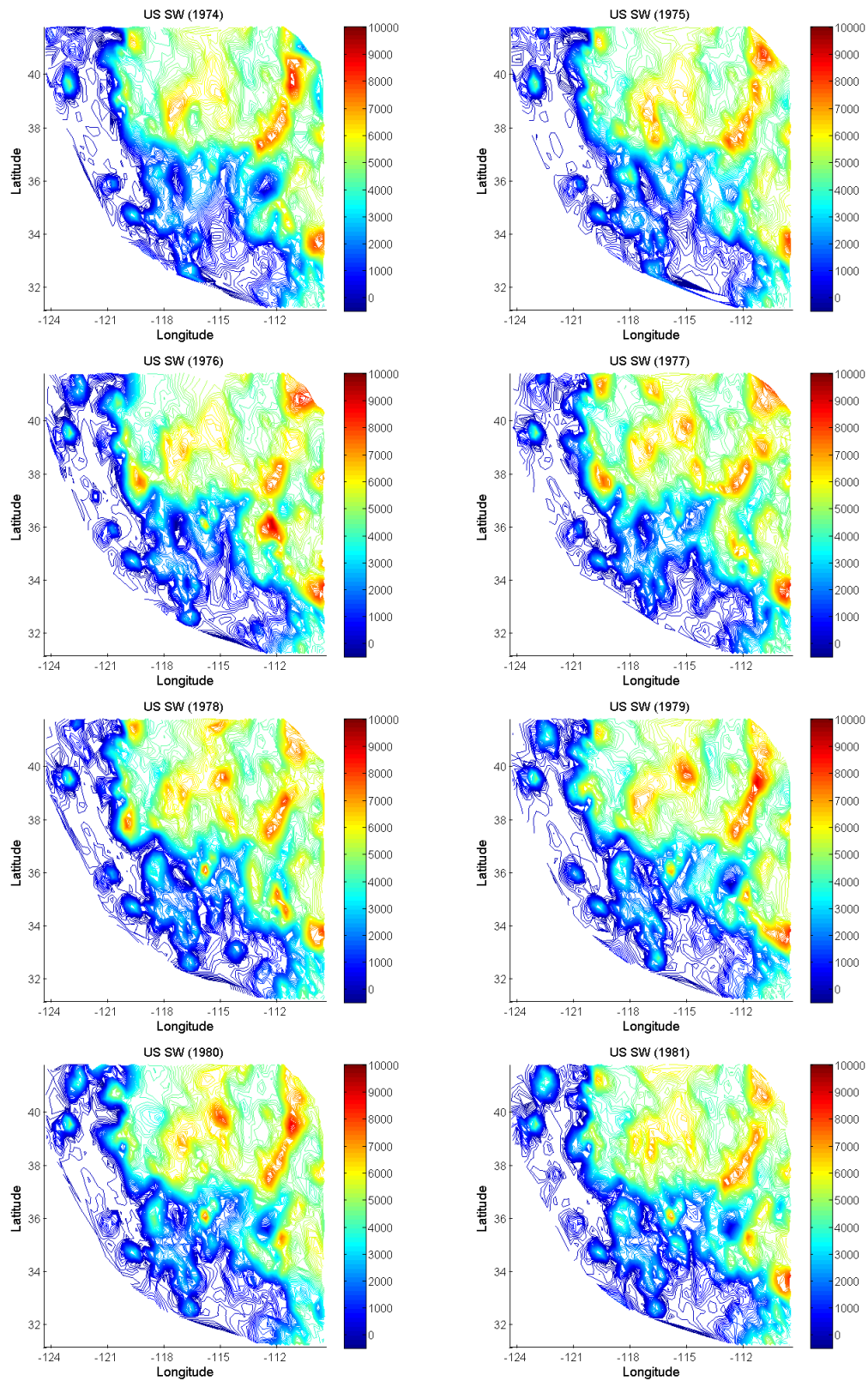
Figure 5.38. Compressed sensing groundwater network data from 1974 to 1981

143
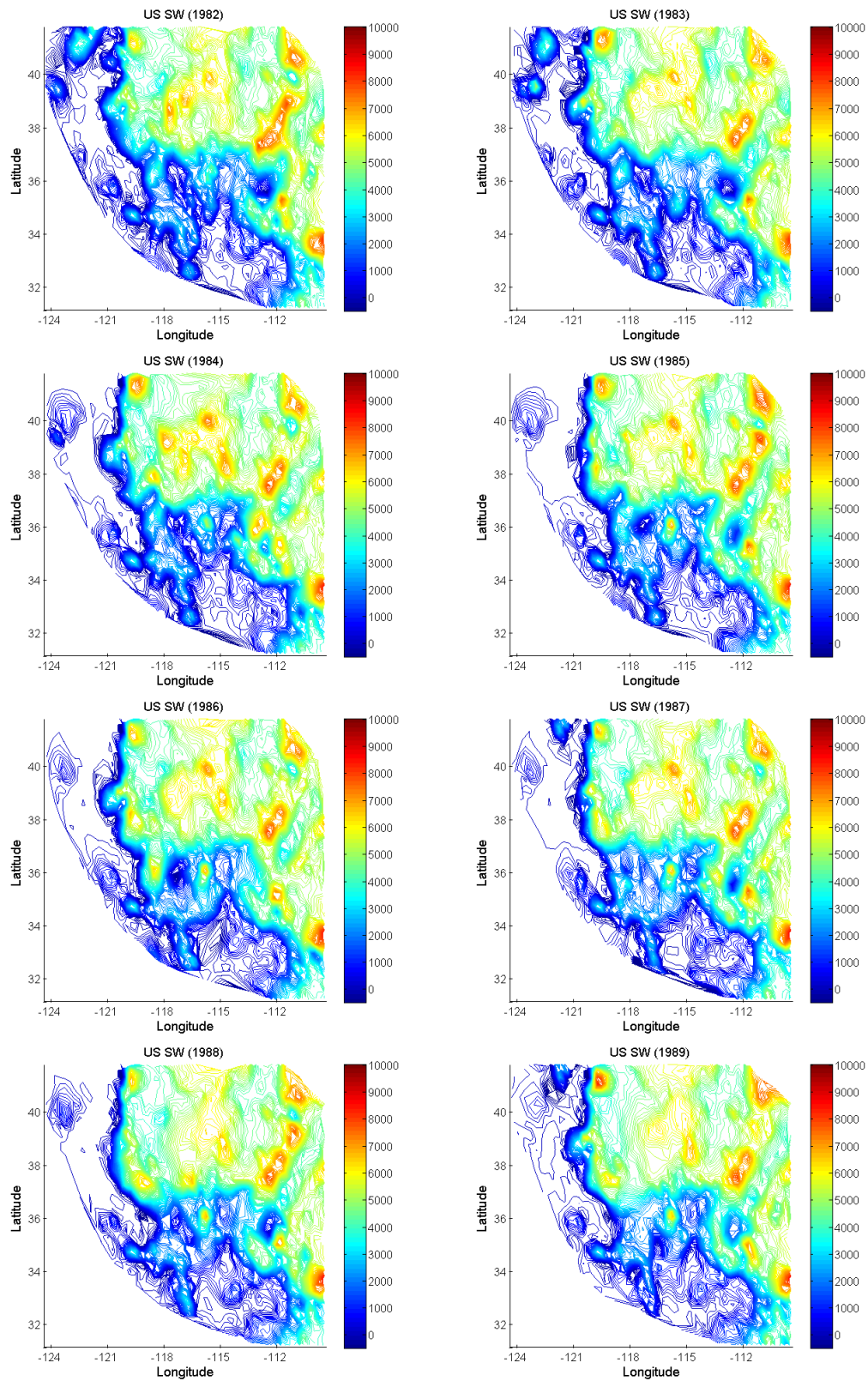
Figure 5.39. Compressed sensing groundwater network data from 1982 to 1989
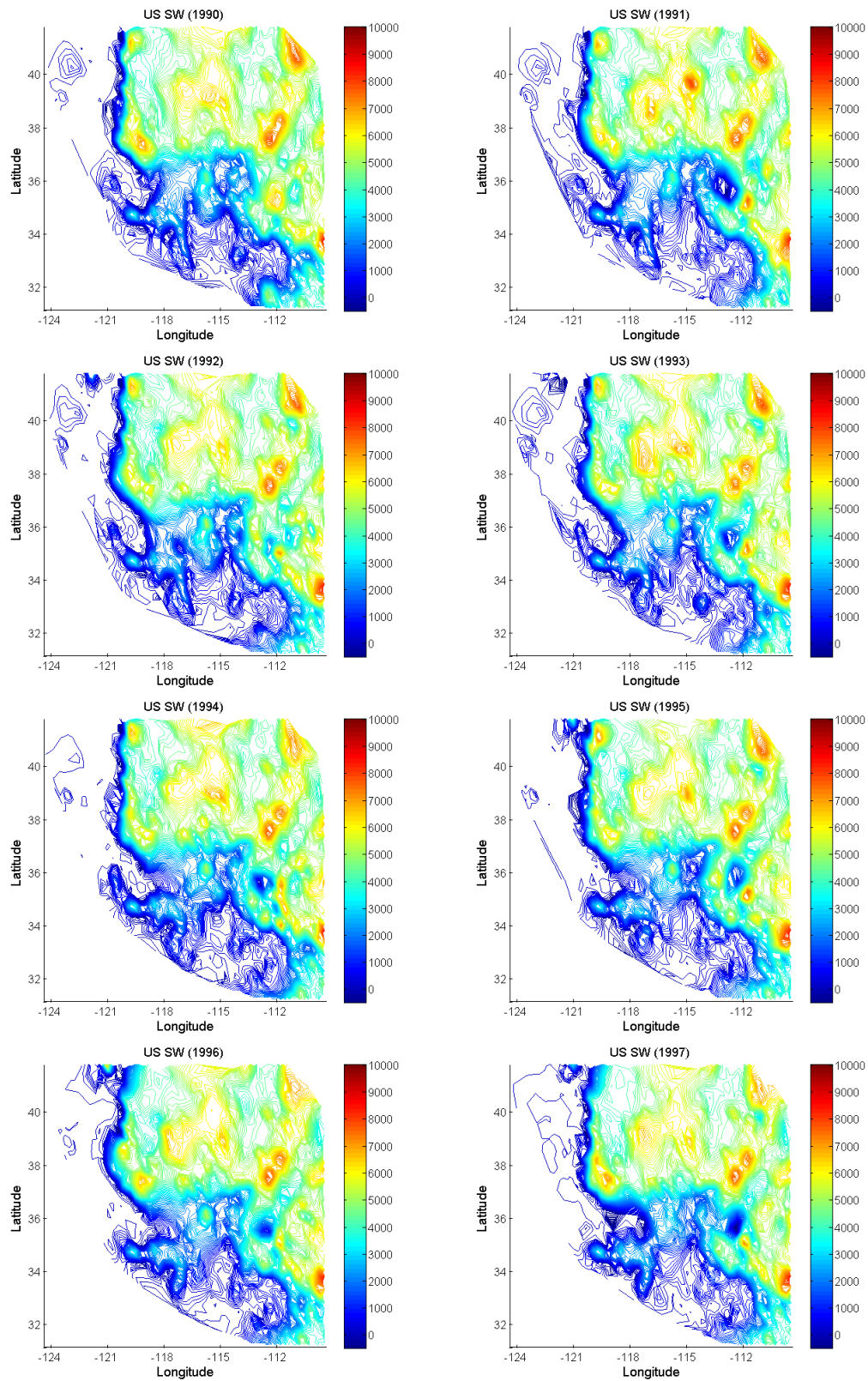
Figure 5.40. Compressed sensing groundwater network data from 1990 to 1997
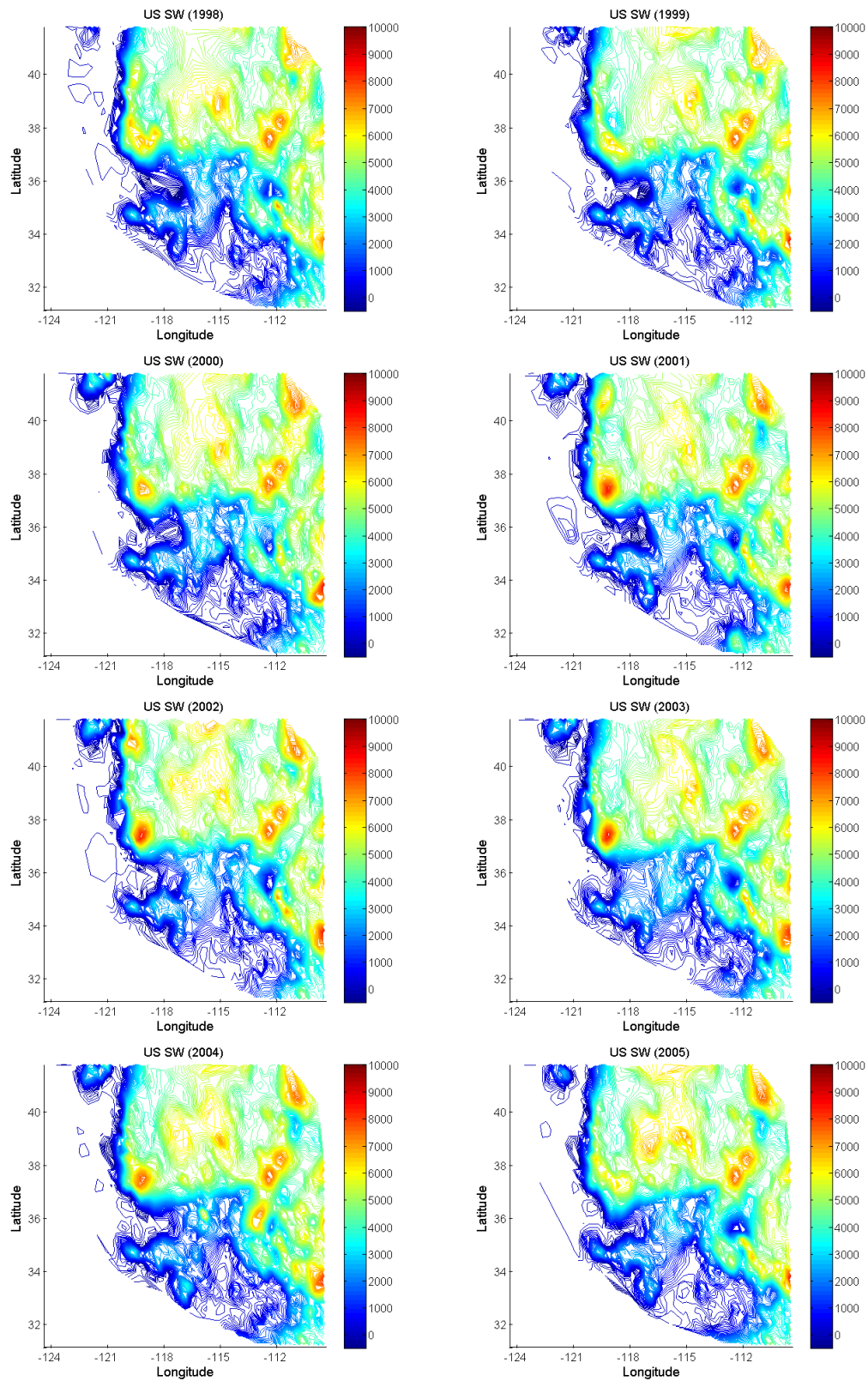
Figure 5.41. Compressed sensing groundwater network data from 1998 to 2005

146
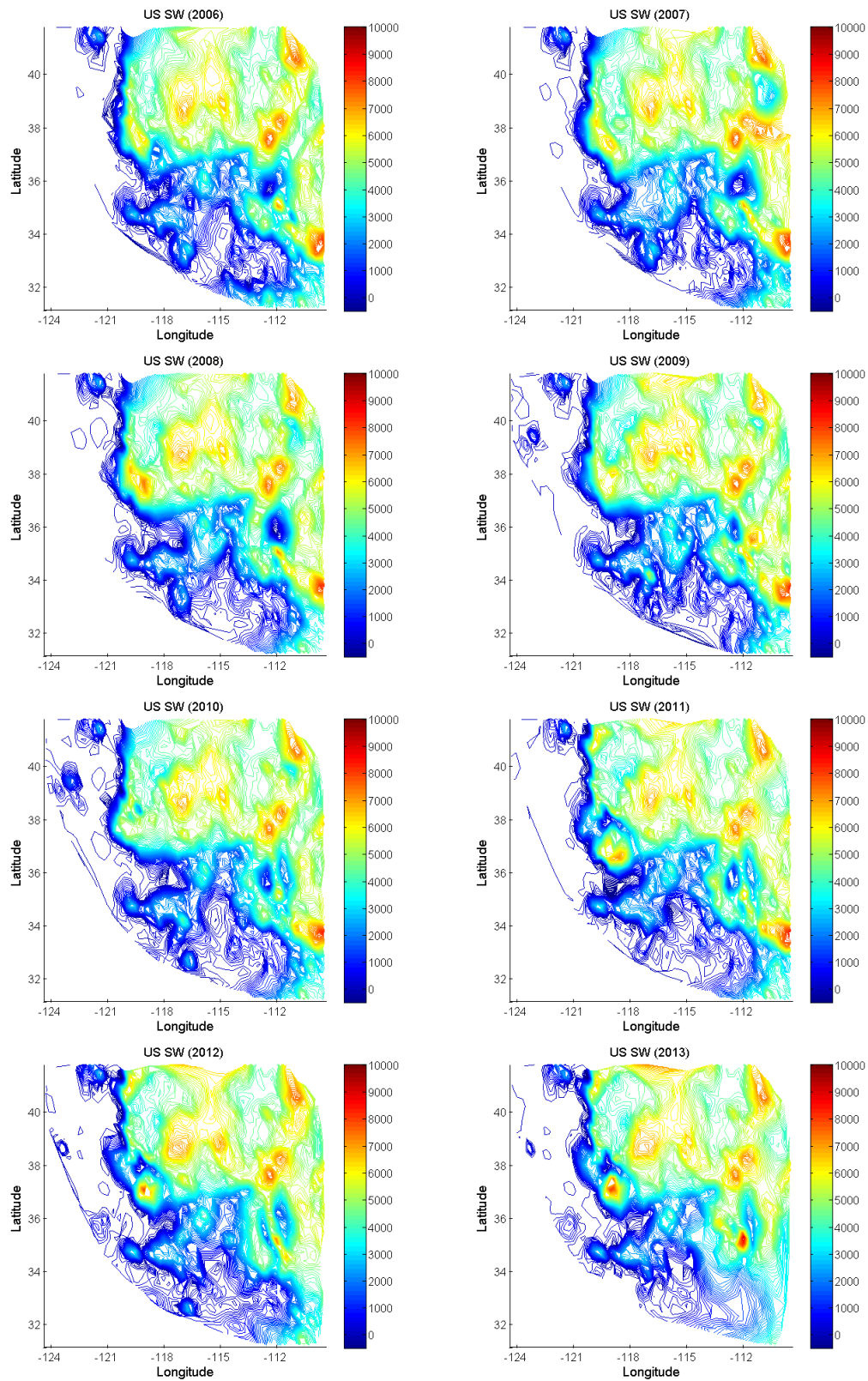
Figure 5.42. Compressed sensing groundwater network data from 2006 to 2013
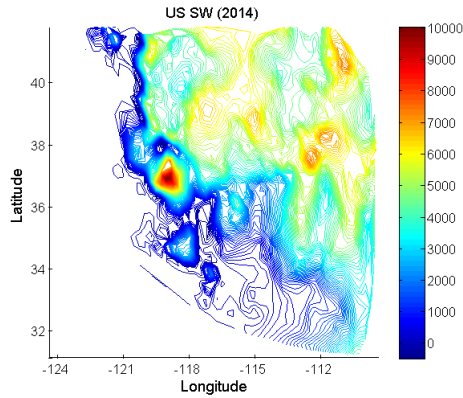
Figure 5.43. Compressed sensing groundwater network data, 2014

## 4.  Limitations

Although the groundwater network data have been constructed, the geological area, which guarantees the accuracy of reconstructed results, should be considered. For example, metropolitan Phoenix resides upon the Phoenix basin. The Phoenix basin is very flat and has not shown any severe change in groundwater elevation. This type of geological area is very suitable for our research. In contrast to observations recorded for the Phoenix basin, the Bulge of Sedona is not a good area of research for the suggested methods because the elevation changes are significant within a narrow region because this region is a valley.

The integrity of historical well data is another point of concern. In the data pre-processing phase, any unverified data were removed to the best of our ability. Because only a very small portion of the well data is maintained as a verified source in the USGS, and access to this network requires authority, certain limitations are inherent in the comprehensive construction of groundwater level network data. Even though ADWR maintains the registered wells either periodically or continuously, the real-time data from

148

these wells have not been provided to the public. As a result, we can only construct the data provided at the time of query on our side. The utilization efficacy of groundwater level data can be enhanced if the access limit is unlocked. For example, in the 1940s, full measurements were not established; hence the missing areas are shown in Fig. 5.34. Since USGS, CDWR, UDWR, ADWR, and NDWR have not provided full measurement data to the public; certain areas in the contour map show a different shape. For another example, contours after1990 in certain California regions did not appear because those areas had experienced difficulty of reconstruction by CS.

## 5. Conclusion

In this chapter, using the estimated groundwater level by CS, trends in groundwater elevation from 1942 to 2014 were investigated. By help of the estimated groundwater elevation via our suggested method, some areas in which do not have any measurement could be analyzed. In trend analysis based on cities, most of the cities in the southwestern US showed a decreasing trend. Even though over 62% of Arizona cities showed a decreasing trend, groundwater management plans such as GMA and CAP have been taking effective actions to sustain groundwater elevation at a proper level. California have had hard time due to severe drought so that groundwater depletion could be noticeably recognized in the groundwater budget. Temperature rise, lean snow pack on the Sierra Nevada Mountains, little rainfall and greedy groundwater withdrawals exacerbated drastic drop of groundwater elevation in the agricultural area, especially, the Central Valley Basin.

Nevada Department of Water Resources has noticed the need for groundwater management through the long-term observations of groundwater elevation over many areas since 1970. In Las Vegas, constantly artificial recharge has been conducted so that its groundwater elevation shows the increasing trend. Utah Department of Water Resources noticed the continuous decrease of groundwater elevation in the Beryl-Enterprise area and currently groundwater management act has been planned and undertook necessary steps. Still the Beryl-Enterprise area shows the continual decrease in groundwater elevation level, however, after the management act takes effect, we could assure that groundwater elevation at least levels off and/or increases based on our investigations in the Groundwater Management Act from Phoenix in Arizona and Las Vegas in Nevada.

In general, we found not only the similar pattern between the area sum of groundwater elevation and the area-averaged groundwater percentile, but also found the close relationship between the area sum of total rainfall and the area-averaged wetness percentile. In California, trend in the area sum of the groundwater elevation similarly matched with that in the area sum of groundwater budget. After separation of areas into two distinct regions such as the Sierra Nevada Mountains and the Central Valley Basins, the simple quantity can be obtained. It is from adding the area sum of accumulated snow in the Sierra Nevada Mountains and the area sum of total rainfall in the Central Valley Basins. It gives the indication of severe drought and probable groundwater depletion when its sum goes below 35 feet. Trend shows the drastic drop of groundwater elevation, groundwater budget, groundwater percentile, wetness percentile, accumulated snow, snow melt, and total rainfall in the Central Valley Basins. Average temperature in the the

150

Sierra Nevada Mountains goes up little by little. In other areas, we could find very similar trend of the general properties in the second analysis mentioned on top of this paragraph.

In trend analysis based on 10 year period, Arizona, California, and Nevada started at the low ratio of decreasing trend wells but, after mid-1940s, trend in ratio of decreasing wells significantly increased. Except Arizona, three other states showed high fluctuation over the period. In spited of fluctuations, all four states showed the decreasing trend in groundwater elevation similarly. In two time buckets over 1985-1994 and 1995-2004, trend decreased but, again trend increased in all four states. Similar pattern between trend in rate of groundwater depletion in the US and trend in ratio of decreasing trend well in Arizona was found. Both trends explained current situations in the same way.

We tried to show the entire coverage of groundwater contour map in the southwestern US. As a result, a catalog of groundwater contour over the entire period was shown by help of the estimated groundwater level via CS. In the catalog, declines of groundwater elevation along with Active Management Areas were noticed during 1940 to 1980. After 1985, level-offs and gains of groundwater elevation could be shown due to effective groundwater management as mentioned above.

Again, the suggested method can be very useful because it reduces the required number of total measurements by at least 42%. It is also an effective method for visualizing discretely measured, sparse data. If the size of the sampled data falls within certain ranges, which are governed by the CS properties, our method can be effectively used to estimate the groundwater level in the southwestern US.

The correct mechanisms why groundwater elevation in wells changes in time in various regions are beyond our knowledge. Limiting groundwater data access to the

public as well as restricted regional development of groundwater near human habitats made this analysis difficult. Nonetheless, declines in groundwater availability have been confirmed like other researchers found and through visualization, the area that needs an immediate attention can be located and found.

References

1. Anderson, T.W., Freethey, G.W., and Tucci, P. 1992. Geohydrology and water resources of alluvial basins in south-central Arizona and parts of adjacent states. *U.S. Geological Survey Professional Paper 1406-B*.

2. Anderson, T.W. 1995. Summary of the southwest Alluvial Basins, Regional Aquifer-System Analysis, south-central Arizona and parts of adjacent states. *U.S. Geological Survey Professional Paper 1406-A*.

3. Belcher, W.R., D'Agnese, F.A., and O'Brien, G.M. 2010. Introduction, in Belcher, W.R., and Sweetkind, D.S., eds., Death Valley regional groundwater flow system, Nevada and California-Hydrogeologic framework and transient groundwater flow model. *U.S. Geological Survey Professional Paper 1711*.

4. Bertoldi, G.L., Johnston, R.H., and Evenson, K.D. 1991. Ground water in the Central Valley, California-A summary report. *U.S. Geological Survey Professional Paper 1401-A*.

5. Clarke, R. and King, J. 2004. *The atlas of water :mapping the world's most critical resource*. London:Earthscan Publications, Ltd.

6. Famiglietti, J.S. 2014. The global groundwater crisis. *Nature Climate Change* 4, 945-948.

8. Galloway, D.L., Jones, D.R., and Ingebritsen, S.E. 1999, Land subsidence in the United States. *U.S. Geological Survey Circular 1182*.

9. Gleick, P.H. 1993. *Water in crisis: A guide to the world's fresh water resources*. Oxford:Oxford University Press.

10. Johnson, M., Cole, E., and Brothers, K. 1997. Artificial recharge in the Las Vegas Valley: An Operational history. Presented at *the 8ᵗʰBiennial symposium on the Artificial Recharge of Groundwater*, in *Tempe, AZ June 2-4*.

11. Kaplan, K. 2014. Satellite images reveal shocking groundwater loss in California. http://www.latimes.com/science/sciencenow/la-sci-sn-california-drought-groundwater-satellite-20141002-story.html

12. Konikow, L. 2013. Groundwater depletion in the United States (1900−2008). *U.S. Geological Survey Scientific Investigations Report 2013−5079.*

13. Mower, R.W. 1982. Hydrology of the Beryl-Enterprise area, Escalante Desert, Utah, with emphasis on ground water. *Utah Department of Natural Resources Technical Publication No. 73.*

14. Plume, R.W. 1989. Ground-water conditions in Las Vegas Valley, Clark County, Nevada-Part I, Hydrogeologic framework. *U.S. Geological Survey Water-Supply Paper 2320-A.*

15. Slaugh, B.A. 2002. Escalante Valley, Milford area: in Ground-water conditions in Utah, spring 2002. *Utah Division of Water Resources Cooperative Investigations Report No. 43.*

16. Styler, M.R. and Jones, K.L. 2012. Beryl Enterprise Groundwater Management Plan. *Utah Department of Natural Resources.*

17. U.S. Geological Service. 2014. *Estimated use of water in the United States in 2010.* USGS Circular 1405.

18. Williamson, A.K., Prudic, D.E., and Swain, L.A. 1989. Ground-water flow in the Central Valley, California. *U.S. Geological Survey Professional Paper 1401-D.*

19. Wood, D.B. 2000. Water use and associated effects on ground-water levels, Las Vegas Valley and vicinity, Clark County, Nevada, 1980–95. *Nevada Division of Water Resources*, *Water-Resources Information Report 35.*

**CHAPTER 6**

**CONCLUSIONS AND FUTURE RESEARCH**


In our first section, in which the basic principles of fluid mechanics and heat transfer were applied, along with a detailed presentation of the flow patterns and temperature distributions provided by computational simulations, significant improvements under both high- and low-temperature conditions can be achieved. In most cases, these achievements can be obtained with relatively simple, implementable modifications.

In our second work, we have considered an appropriate form for the viscous dissipation term in the integral form of the conservation equation, and we examined the effects of momentum terms on the computed drop size. The SMD calculated in this manner agrees well with the experimental data, which included measurements of both the drop velocities and sizes. The revised treatment of liquid momentum also leads to highly stable calculations for a wide range of density ratios. The injection parameters, such as the spray cone angle and the atomization length, are directly input into the system of equations. Thus, this approach can incorporate various injection parameters into the computations and can be used for further considerations of the drop and velocity distributions under a wide range of spray geometry and injection conditions.

In the last section, groundwater level estimation was investigated using compressed sensing. To satisfy a general property of compressed sensing, a random measurement matrix was used. The groundwater network was constructed, and finally l-1 optimization algorithm was run under objective function with constraints. The groundwater network data results from 1942 to 2014 exhibited a trend of fluctuating groundwater levels in the

southwestern US. Arizona, Nevada, California, and Utah showed an overall decreasing groundwater level trend. The suggested method can be used to estimate the groundwater level. By comparing the original data with the reconstructed data and employing various validation methods, we show the validity of our reconstruction of the estimated groundwater level and demonstrate a possible approach for groundwater management.

We found not only the similar pattern between the area sum of groundwater elevation and the area-averaged groundwater percentile, but also found the close relationship between the area sum of total rainfall and the area-averaged wetness percentile. In California, trend in the area sum of the groundwater elevation similarly matched with that in the area sum of groundwater budget. After separation of areas into two distinct regions such as the Sierra Nevada Mountains and the Central Valley Basins, the simple quantity can be obtained. It is from adding the area sum of accumulated snow in the Sierra Nevada Mountains and the area sum of total rainfall in the Central Valley Basins. It gives the indication of severe drought and probable groundwater depletion when its sum goes below 35 feet. In Arizona, Nevada and Utah, we could find very similar trend between the area sum of groundwater elevation and the area-averaged groundwater percentile as well as the close relationship between the area sum of total rainfall and the area-averaged wetness percentile.

The suggested method can be very useful in certain applications because it reduces the total amount of measurements required by at least 42%. It is also an effective method for visualizing discretely measured sparse data. If the size of the sampled data falls within certain ranges, our method can be effectively used for groundwater level estimations in the southwestern US.

For future research, by combining the elevation data within the geographical region under study with the geographical information (for example, combining the basin and sub-basin with the aquifer information), the accuracy of the results can be enhanced. If unlimited access were granted to the public for the provided data and real-time measurements could be combined with the suggested method, meaningful groundwater network data could be generated on a real-time basis. Another necessary technical advancement for compressed sensing is the construction of a measurement matrix, which remains an important task for groundwater level estimation. Such a matrix would likely be very region-specific; however, the matrix would increase the incoherence property so that the total amount of measured sparse data can be reduced by at least a factor of 2.

When a data network is established with a specially devised analog sensing device, more effective reconstructions can be obtained for other sites, even though the groundwater level within a certain area may not be evenly distributed due to the heavy use of groundwater and the fact that various groundwater flow velocities in different regions are induced by the respective soil characteristics.

REFERENCES

1. Ahmadi, M. and Sellens, R.W. 1993. Simplified maximum entropy based drop size distribution. *Atomization and Sprays*, 3 (3): 291-310.

2. Anderson, T.W., Freethey, G.W., and Tucci, P. 1992. Geohydrology and water resources of alluvial basins in south-central Arizona and parts of adjacent states. *U.S. Geological Survey Professional Paper 1406-B*.

3. Anderson, T.W. 1995. Summary of the southwest Alluvial Basins, Regional Aquifer-System Analysis, south-central Arizona and parts of adjacent states. *U.S. Geological Survey Professional Paper 1406-A*.

4. Atlas, R.M. and Lucchesi, R. 2000. File specificatioin for GEOS-DAS gridded output. *DAO-1001*, Ver. 4.3, 41.

5. Babinsky, E. and Sojka, P.E. 2002. Modeling drop size distributions. *Progress in Energy and Combustion Science*, 28 (4): 303-329.

6. Baraniuk, R.G. 2007. Compressive sensing. *IEEE Signal Processing Magazine*, 24 (4): 118-121.

7. Belcher, W.R., D'Agnese, F.A., and O'Brien, G.M. 2010. Introduction, in Belcher, W.R., and Sweetkind, D.S., eds., Death Valley regional groundwater flow system, Nevada and California-Hydrogeologic framework and transient groundwater flow model. *U.S. Geological Survey Professional Paper 1711*.

8. Bertoldi, G.L., Johnston, R.H., and Evenson, K.D. 1991. Ground water in the Central Valley, California-A summary report. *U.S. Geological Survey Professional Paper 1401-A*.

9. Boyd, S. and Vandenberghe, L. 2004. *Convex optimization*. Cambridge:Cambridge University Press.

10. Brassel, K.E. and Reif, D. 2010. A procedure to generate Thiessen polygons. *Geographical Analysis*, 11 (3): 289-303.

11. Candes, E.J., Romberg, J., and Tao, T. 2006. Robust uncertainty principles: exact signal reconstruction from highly incomplete frequency information. *IEEE Transactions on Information Theory*. 52 (2): 489-509.

12. Chami, N. and Zoughaib, A. 2010. Modeling natural convection in a pitched thermosyphon system in building roofs and experimental validation using particle image velocimetry. *Energy and Buildings*, 42 (8): 209-216.

13. Cheng, C.-H. and Hung, K.-S. 2005. Experimental and numerical study of three-dimensional flow field in minienvironment. *Energy and Buildings*, 37 (6): 579-586.

14. Clark, J.A. 2001. *Energy simulation in building design.* London: Butterworth-Heinemann.

15. Clarke, R. and King, J. 2004. *The atlas of water :mapping the world's most critical resource*. London:Earthscan Publications, Ltd.

16. Cohn, S.E., Da Silva, A. , Guo, J. Sienkiewicz, M., and Lamich, D. 2003. Assessing the effects of data selection with the DAO physical-space statistical analysis system. *Monthly Weather Review*, 126 (11): 2913-2926.

17. Cousin, J., Yoon, S.J., and Dumouchel, C. 1996. Coupling of classical linear theory and maximum entropy formalism for prediction of drop size distribution in sprays. *Atomization and Sprays,* 6 (5): 601-622.

18. Cosgrove, B.A. and coauthours 2003. Real-time and retrospective forcing in the north American land data assimilation system project, *Journal of Geophysical Resources*, 108 (D22): 8842-8853.

19. Cunningham, W. Direct conversation, March 15, 2013.

20. DeVore, R.A. 2007. Deterministic constructions of compressed sensing matrices. *Journal of Complexity*, 23 (4-6): 918-925.

21. Divekar, A. and Ersoy, O. 2009. Image fusion by compressive sensing. *The 17th International Conference on Geoinformatics*, in *Fairfax, VA*. Aug. 12-14.  2 (1): 1-6.

22. Donoho, D.L. 2006. Compressed sensing. *IEEE Transactions on Information Theory.* 52 (4): 1289-1306.

23. Duarte, M.F. and Eldar, Y.C. 2011. Structured compressed sensing: from theory to applications. *IEEE Transactions on Signal Processing.* 59 (9): 4503-4085.

24. Dumouchel, C. 2007. A new formulation of the maximum entropy formalism to model liquid spray drop-size distribution. *Particle and Particle Systems Characterization*, 23 (6): 468-479.

25. Dumouchel, C. 2009. The maximum entropy formalism and the prediction of liquid spray drop-size distribution. *Entropy*, 11 (4): 713-747.

26. Dumouchel, C. and Boyaval, S. 1999. Use of the maximum entropy formalism to determine drop size distribution characteristics. *Particle and Particle Systems Characterization*, 16 (4): 177-184.

27. Elad, M. 2010. *Sparse and Redundant Representations.* New York:Springer.

28. Elad, M., Starck, J.-L., Querre, P., and Donoho, D.L. 2005. Simultaneous cartoon and texture image inpainting using morphological component analysis (MCA). *Applied and Computational Harmonic Analysis*, 19 (3): 340-358.

29. Eldar, Y.C. and Kutyniok, G. 2012. *Compressed Sensing: Theory and Applications.* Cambridge:Cambridge University Press.

30. Famiglietti, J.S. 2014. The global groundwater crisis. *Nature Climate Change* 4, 945-948.

31. FLUENT. 2006. *Fluent 6.3 user's guide*. Lebanon: Fluent Incorporation.

32. Galloway, D.L., Jones, D.R., and Ingebritsen, S.E. 1999, Land subsidence in the United States. *U.S. Geological Survey Circular 1182*.

33. Gan, G. 1995. Evaluation of room air distribution systems using computational fluid dynamics. *Energy and Buildings*, 23 (2): 83-93.

34. Gleick, P.H. 1993. *Water in crisis: A guide to the world's fresh water resources.* Oxford:Oxford University Press.

35. Gosselin, J.R. and Chen, Q. 2008. A computational method for calculating heat transfer and airflow through a dual-airflow window. *Energy and Buildings*, 40 (4): 452-458.

36. Hackett, O.M., 1963. *Ground-water levels in the United States 1956-1960 southwestern states*. Geological Survey Water-Supply Paper 1770.

37. Hamill, T. M., R. P. d'Entremont, and J. T. Bunting, 1992. A description of the Air Force real-time nephanalysis model. *Weather and Forecasting*, 7 (2): 288-306.

38. Han, Dazhong and J. Wahr, 1995. The viscoelastic relaxation of a realistically stratified earth, and a further analysis of post-glacial rebound, *Geophysical Journal International*, 120 (2): 287-311.

39. Hansen, M.C., DeFries, R.S. Townshend, J.R.G., and Sohlberg, R., 2000. Global land cover classification at 1km spatial resolution using a classification tree approach. *International Journal of Remote. Sensing*, 21 (6-7): 1331-1364.

40. Herrmann, M. 2010. A parallel Eulerian interface tracking_Lagrangian point particle multi-scale coupling procedure. *Journal of Computational Physics*, 229 (3): 745-759.

41. Herrmann, M. 2010. Detailed numerical simulations of the primary atomization of a turbulent liquid jet in crossflow. *Journal of Engineering for Gas Turbines and Power in ASME Transaction*, 132 (6): 061506. 1-10.

42. Herrmann, M., Gorokhovski, M. 2009. A large eddy simulation subgrid model for turbulent phase interface dynamics. *The 11th Triennial Conference on Liquid Atomization and Spray Systems*, in Vail, CO. Paper No. ICLASS2009-205.

43. Huffman, G. J., R. F. Adler, E. F. Stocker, D. T. Bolvin, and E. J. Nelkin, 2003. Analysis of TRMM 3-hourly multi-satellite precipitation estimates computed in both real and post-real time. In *Proceedings of 12$^{th}$ Conference on Satellite Meteorology and Oceanography, Long Beach, CA, February 8-13*, P4.11.

44. Idso, S., 1981. A set of equations for the full spectrum and 8- and 14-micron and 10.5- to 12.5 thermal radiation from cloudless skies. *Water Resources Research*, 17 (2): 295-304.

45. Johnson, M., Cole, E., and Brothers, K. 1997. Artificial recharge in the Las Vegas Valley: An Operational history. Presented at *the 8$^{th}$Biennial symposium on the Artificial Recharge of Groundwater*, in *Tempe, AZ June 2-4.*

46. Kaplan, K. 2014. Satellite images reveal shocking groundwater loss in California. http://www.latimes.com/science/sciencenow/la-sci-sn-california-drought-groundwater-satellite-20141002-story.html

47. Konikow, L. 2013. Groundwater depletion in the United States (1900−2008). *U.S. Geological Survey Scientific Investigations Report 2013−5079.*

48. Kuznik, F., Rusaouën, G., Hohotă, R. 2006. Experimental and numerical study of a mechanically ventilated enclosure with thermal effects. *Energy and Buildings*, 38 (8): 931-938.

49. Klinker, E., F. Rabier, G. Kelly, and J. F. Mahfouf, 2000. The ECMWF operational implementation of four dimensional variational assimilation. Part III: Experimental results and diagnostics with operational configuration. *Quarterly Journal of the Royal Meteorological Society*, 126 (564): 1191-1215.

50. Kopp, T. J., and R. B. Kiess, 1996. The Air Force Global Weather Central cloud analysis model. In *proceedings of 15$^{th}$ Conference on Weather Analysis and Forecasting,* in *Norfolk, VA, August 19-23*, 1220-1222.

51. Lamb,H. 1945. *Hydrodynamics.* New York: Dover Publication.

52. Lin, G.F. and Chen, L.H. 2004. A spatial interpolation method based on radial basis function networks incorporating a semivariogram model. *Journal of Hydrology.* 288 (3-4): 288-298.

53. Lin, Y. and Zmeureaunu, R. 2008. Computer model of the air and thermal phenomena inside a large dome. *Energy and Buildings*, 40 (7): 1287-1296.

54. Lee, T.-W. and Mitrovic, A. 1996. Liquid core structure of pressure-atomized sprays via laser tomographic imaging. *Atomization and Sprays,* 6 (1): 111-126.

55. Lee, T.-W. and Robinson, D. 2011. Calculation of the drop size distribution and velocities from the integral form of the conservation equations. *Combustion Science and Technology,* 183 (3): 271-284.

56. Li, X., Chin, L.P., Tankin, R.S., Jackson, T., Stutrud, J., and Switzer, G. 1991. Comparison between experiments and predictions based on maximum entropy for sprays from a pressure atomizer. *Combustion and Flame*, 86 (1-2): 73-89.

57. Li, X., Tankin, R.S., Sztal, B., and Most, J.-M. 1988. Derivation of droplet size distribution in sprays by using information theory. *Combustion Science and Technology,* 60 (4-6): 345-357.

58. Mahrt, L. and Ek, M. 1984. The influence of atmospheric stability on potential evaporation. *Journal of Applied Meteorology,* 23 (2): 222-234.

59. Mahrt, L. and Pan, H. 1984.A two-layer model of soil hydrology. *Boundary Layer Meteorology,* 29: 1-20.

60. Mower, R.W. 1982. Hydrology of the Beryl-Enterprise area, Escalante Desert, Utah, with emphasis on ground water. *Utah Department of Natural Resources Technical Publication No. 73.*

61. Mugele, R. and Evans, H.D. 1951. Droplet size distribution in sprays. *Industrial and Engineering Chemistry,* 43 (6): 1317-1324.

62. Ng, K.C., Kadirgama, K., and Ng, E.Y.K. 2008. Response surface models for CFD predictions of air diffusion performance index in a displacement ventilated office. *Energy and Buildings*, 40 (5): 774-781.

63. Olea, R.A. 1974. Optimal contour mapping using universal Kriging. *Journal of Geophysical Research.* 79 (5): 695-702.

64. Ottle, C., and D. Vidalmadjar, 1992. Estimation of land surface temperature with NOAA9 data. *Remote Sensing of Environment*, 40 (1): 27-41.

65. Pfaendtner, J., S. Bloom, D. Lamich, M. Seablom, M. Sienkiewicz, J. Stobie, and A. da Silva, 1995. Documentation of the Goddard Earth Observing System (GEOS) Data Assimilation System-Version 1. *NASA Technical Memorandum 104606,* 4: 1-44.

66. Plume, R.W. 1989. Ground-water conditions in Las Vegas Valley, Clark County, Nevada-Part I, Hydrogeologic framework. *U.S. Geological Survey Water-Supply Paper 2320-A.*

67. Ren, Z and Stewart, J. 2003. Simulating air flow and temperature distribution inside buildings using a modified version of COMIS with sub-zonal divisions. *Energy and Buildings*, 35 (3): 257-271.

68. Reynolds, C. A., T. J. Jackson, and W. J. Rawls, 2000. Estimating soil water-holding capacities by linking the Food and Agriculture Organization Soil map of the world with global pedon databases and continuous pedotransfer functions. *Water Resources Research*, 36 (12): 3653-3662.

69. Ritz, R.D. 1987. Modeling atomization processes in high-pressure vaporizing sprays. *Atomisation and Spray Technology,* 3 (4): 309-337.

70. Rodell, M., P. R. Houser, U. Jambor, J. Gottschalck, C.-J. Meng,K. Arsenault, N. DiGirolamo, and D. Hall, 2002. Use of MODIS-derived snow fields in the Global Land Data Assimilation System. Presented at *Mississippi River Climate and Hydrology Conference*, in *New Orleans, LA, May 15*, 118.

71. Rodell, M., Chen, J., Kato, H., Famiglietti, J.S., Nigro, J., and Wilson, C.R. 2006. Estimating groundwater storage changes in the Mississippi river basin (USA) using GRACE. *Hydrogeology Journal,* 15 (1): 159-166.

72. Rodell, M., Houser, P.R., Jambor, U., Gottschalck, J., Mitchell, K., Meng, C-J., Arsenault, K., Cosgrove, B., Radakovich, J., Bosilovich, M., Entin, J.K., Walker, J.P., Lohmann, D. and Toll, D. 2004. The global land data assimilation system. *American Meteorological Society,* 85 (3): 381-394.

73. Rothe, P.H. and Blcok, J.A. 1977. Aerodynamic behavior of liquid sprays. *International Journal of Multiphase Flow,* 3 (3): 263-272.

74. Ruff, G.A., Bernal, L.P., and Faeth, G.M. 1991. Structure of the near-injector region of non-evaporating pressure-atomized sprays. *Journal of Propulsion*, 7 (2): 221-230.

75. Schaake, J.C., Koren, V.I., Duan, Q-Y., Mitchell, K. and Chen, F. 1996. Simple water balance model for estimating runoff at different spatial and temporal scales. . *Journal of Geophysical Research.* 101 (D3): 7461-7475.

76. Sellens, R.W. and Brzustowski, T.A. 1986. A simplified prediction of droplet velocity distributions in a spray. *Combustion and Flame,* 65 (3): 273-279.

77. Shapiro, R., 1987: A simple model for the calculation of the flux of direct and diffuse solar radiation through the atmosphere. Air Force Geophysics Laboratory, *AFGL-TR-87-0200*, Hanscom AFB, MA, 40.

78. Sinha, S.L., Arora, R.C., and Roy, S. 2000. Numerical simulation of two-dimensional room air flow with and without buoyancy. *Energy and Buildings*, 32 (1): 121-129.

79. Sirignano, W.A. and Mehring, C. 2000. Review of theory of distortion and disintegration of liquid streams. *Progress in Energy and Combustion Science,* 26 (4): 609-655.

80. Slaugh, B.A. 2002. Escalante Valley, Milford area: in Ground-water conditions in Utah, spring 2002. *Utah Division of Water Resources Cooperative Investigations Report No. 43.*

81. Sovani, S.D., Sojka, P.E., and Sivathanu, Y.R. 2002. Prediction of drop size distributions from first principles: joint PDF effects. *Atomization and Sprays*, 10 (6): 213-222.

82. Stojnic, M. 2010. $l_2/l_1$-optimization in block-sparse compressed sensing and its strong thresholds. *IEEE Transactions on Selected Topics in Signal Processing.* 4 (2): 350-357.

83. Styler, M.R. and Jones, K.L. 2012. Beryl Enterprise Groundwater Management Plan. *Utah Department of Natural Resources.*

84. Swenson, S., and Wahr, J. 2002. Estimated effects of the vertical structure of atmospheric mass on the time-variable geoid. *Journal of Geophysical Research*, 107 (B9): ETG4.1-11.

85. Takhar, D., Laska, J.N., Wakin, M.B., Duarte, M.F., Baron, D., Sarvotham, S., Kelly, K.F., and Baraniuk, R.G. 2006. A new compressive sensing imaging camera architecture using optical-domain compression. In *Proceedings of Computational Imaging IV at Society of Photo-Optical Instrumentation Engineers Electronic Imaging*, in *San Jose, CA, January 15*, 6065 (67001): 43-52.

86. Turk, F. J., G. Rohaly, J. D. Hawkins, E. A. Smith, A. Grose, F. S. Marzano, A. Mugnai, and V. Levizzani, 2000. Analysis and assimilation of rainfall from blended SSM/I, TRMM and geostationary satellite data. In Proceedings of *10th Conference on Satellite Meteorology and Oceanography*, in *Long Beach, CA, January 10*, 66-69.

87. Tillman, F. D. and Leake, S. A. 2010. Trends in groundwater levels in wells in the active management areas of Arizona, USA. *Hydrogeology Journal*, 18 (6): 1515-1524.

88. Todd, D.K. and Mays, L.W. 2005. *Groundwater hydrology 3rd ed*. Hoboken:John Wiley and Sons, Inc.

89. U.S. Geological Service. 2009. *Estimated use of water in the United States in 2005*. USGS Circular 1344.

90. U.S. Geological Service. 2014. *Estimated use of water in the United States in 2010.* USGS Circular 1405.

91. United States Global Change Research Program. 2009. *Global climate change impact in the United States: Chapter on Energy Supply and Use.* New York: Cambridge University Press.

92. van der Geld, C.W.M and Vermeer, H. 1994. Prediction of drop size distributions in sprays using the maximum entropy formalism: the effect of satellite formation. *International Journal of Multiphase Flow,* 20 (2): 363-381.

93. Verdin, K. L. and Jenson, S. K. 1996. Development of continental scale digital elevation models and extraction of hydrographic features. In *Proceedings of 3rd International Conference and Workshop on Integrating GIS and Environmental Modeling*, in *Santa Fe, NM*, *January 21*, Session 8.2.

94. Vinogradov, Y. B. 1988. Mathematical modeling of river runoff processes. *Gidrometeoizdat*, St. Petersburg, Russia.

95. Watson, D.F., and Philip, G.M. 1985. A refinement of inverse distance weighted interpolation. *Geo-Processing. Journal of Hydrology.* 2 (4): 315-327.

96. Williamson, A.K., Prudic, D.E., and Swain, L.A. 1989. Ground-water flow in the Central Valley, California. *U.S. Geological Survey Professional Paper 1401-D.*

97. Wood, D.B. 2000. Water use and associated effects on ground-water levels, Las Vegas Valley and vicinity, Clark County, Nevada, 1980–95. *Nevada Division of Water Resources*, *Water-Resources Information Report 35.*

98. Yin, W., Osher, S., Goldfarb, D. and Darbon, J. 2008. Bregman iterative algorithms for l1-minimization with applications to compressed sensing. *Journal of Imaging Science in Society for Industrial and Applied Mathematics*, 1 (1): 143-168.

APPENDIX A

LINEAR PRORAMMING

The standard-form linear program is

$$\min <c_0, x> \quad subject\ to\ A_0 x = b \tag{1}$$

$f_i(x) \leq 0$ where the search vector $x \in \mathbb{R}^N$, $b \in \mathbb{R}^K$, $A_0$ is a $K \times N$ matrix, and each of the

$f_i, i = 1, 2, \dots, m$ is a linear functional $f_i(x) = <c_0, x> + d_i$. For some $c_i \in \mathbb{R}^N$, $d_i \in \mathbb{R}$.

At the optimal point $x^*$, there will exist dual vectors $\epsilon^* \in \mathbb{R}^K$, $\lambda^* \in \mathbb{R}^m$, $\lambda^* \geq 0$ such that

the Karush-Kuhn-Tucker conditions (equations (2)~(5)) are satisfied.

$$c_0 + A_0^T \epsilon^* + \sum_i \lambda_i^* c_i = \mathbf{0}\ b \tag{2}$$

$$\lambda_i^* f_i(x^*) = 0, for\ i = 1, 2, \dots, m \tag{3}$$

$$A_0 x^* = b \tag{4}$$

$$f_i(x^*) \leq 0, for\ i = 1, 2, \dots, m \tag{5}$$

The primal dual algorithm finds the optimal $x^*$ along with optimal dual vectors $\epsilon^*$ and $\lambda^*$

by solving the system of nonlinear equations. The solution procedure is the classical

Newton method. At an interior point $(x^k, \epsilon^k, \lambda^k)$ which satisfies $f_i(x^k) < 0$ and $\lambda^k \geq 0$,

the system is linearized and solved. However, the step to new point $(x^{k+1}, \epsilon^{k+1}, \lambda^{k+1})$

must be modified so that it remains in the interior of the hyper polytopes. In practice, we

relax the complementary slackness condition $\lambda_i^k f_i(x^k) = 0$ to $\lambda_i^k f_i(x^k) = -1/\tau^k$ where

we judiciously increase the parameter $\tau^k$ as we progress through the Newton iterations.

This biases the solution of the linearized equations towards the interior, allowing a

smooth, well-defined central path from an interior point to the solution on the boundary.

The primal, dual, and central residuals quantify how close a point $(x, \epsilon, \lambda)$ is to a satisfying (KKT) with relaxed complementary slackness condition in place of the slackness condition.

$$r_{dual} = c_0 + A_0^T \epsilon^k + \sum_i \lambda_i^k c_i \tag{6}$$

$$r_{central} = -\Lambda f - \left(-1/_{\tau^k}\right) \mathbf{1} \tag{7}$$

$$r_{primal} = A_0 x - b \tag{8}$$

where $\Lambda$ is a diagonal matrix with $(\Lambda)_{ii} = \lambda_i$, and $f = \left(f_1(x), \dots, f_m(x)\right)^T$.

From a point $(x, \epsilon, \lambda)$, we want to find a step $(\Delta x, \Delta \epsilon, \Delta \lambda)$ such that $r_\tau(x + \Delta x, \epsilon + \Delta \epsilon, \lambda + \Delta \lambda) = 0$. Linearizing $r_\tau(x + \Delta x, \epsilon + \Delta \epsilon, \lambda + \Delta \lambda) = 0$ with the Taylor expansion around $(x, \epsilon, \lambda)$,

$$r_\tau(x + \Delta x, \epsilon + \Delta \epsilon, \lambda + \Delta \lambda) \approx r_\tau(x, \epsilon, \lambda) + J_{r_\tau}(x, \epsilon, \lambda) \begin{pmatrix} \Delta x \\ \Delta \epsilon \\ \Delta \lambda \end{pmatrix}, \text{ where } J_{r_\tau}(x, \epsilon, \lambda) \text{ is the}$$

Jacobian of $r_\tau$, we have the system

$$\begin{pmatrix} \mathbf{0} & A_0^T & C^T \\ -\Lambda C & \mathbf{0} & -F \\ A_0 & \mathbf{0} & \mathbf{0} \end{pmatrix} \begin{pmatrix} \Delta x \\ \Delta \epsilon \\ \Delta \lambda \end{pmatrix} = - \begin{pmatrix} c_0 + A_0^T \epsilon + \sum_i \lambda_i c_i \\ -\Lambda f - (-1/_\tau) \mathbf{1} \\ A_0 x - b \end{pmatrix}$$

where $m \times N$ matrix C has the $c_i^T$ as rows, and F is diagonal with $(F)_{ii} = f_i(x)$. We can eliminate $\Delta \lambda$ using $\Delta \lambda = -\Lambda F^{-1} C \Delta x - \lambda - \left(-1/_\tau\right) f^{-1}$. Leaving us with the core system

$$\begin{pmatrix} -C^T F^{-1} \Lambda C & A_0^T \\ A_0 & \mathbf{0} \end{pmatrix} \begin{pmatrix} \Delta x \\ \Delta \epsilon \end{pmatrix} = \begin{pmatrix} -c_0 - A_0^T \epsilon + (1/_\tau) C^T f^{-1} \\ b - A_0 x \end{pmatrix}$$

With the $(\Delta x, \Delta \epsilon, \Delta \lambda)$ we have a step direction. To choose the step length $0 < s \leq 1$, we ask that it satisfy two criteria:

1. $x + s\Delta x$ and $\lambda + s\Delta \lambda$ are in the interior, for example, $f_i(x + s\Delta x) < 0, \lambda_i > 0 \; for \; all \; i$.

2. The norm of the residuals has decreased sufficiently:

$$\|r_\tau(x + \Delta x, \epsilon + \Delta \epsilon, \lambda + \Delta \lambda)\|_2 \leq (1 - \alpha s) \cdot \|r_\tau(x, \epsilon, \lambda)\|_2$$

where $\alpha$ is a user-specified parameter. In all of our implementations, we have set $\alpha = 0.01$.

Since the $f_i$ are linear functionals, item 1 is easily addressed. We choose the maximum step size that just keeps us in the interior. Let $H_f^+ = \{i: \langle c_i, \Delta z \rangle > 0\}, H_\lambda^- = \{i: \Delta \lambda < 0\}$,

and set $s_{max} = 0.99 \cdot \min \left\{ 1, \left\{ {-f_i(x)}/{\langle c_i, \Delta z \rangle}, i \in H_f^+ \right\}, \left\{ {-\lambda_i}/{\Delta \lambda_i}, i \in H_\lambda^- \right\} \right\}$. Then

starting with $s = s_{max}$, we check if item 2 above is satisfied. If not, we set $s' = \beta \cdot s$ and try again. $\beta = 1/2$ is set in our implementations.

When $r_{dual}$ and $r_{primal}$ are small, the surrogate duality gap $\eta = -f^T \lambda$ is an approximation to how close a certain $(x, \epsilon, \lambda)$ is to being optimal. The primal-dual algorithm repeats the Newton iterations described above until $\eta$ has decreased below a given tolerance. This is excerpted from l1-magic notes (Candes and Romberg 2005).

APPENDIX B

MATLAB PSEUDO-CODE FOR L1-MINIMIZATION

The objective function is minimization of $\langle c_0, x \rangle$ subject to $A_0 x = b$ and $f(x) < 0$ where

$x \in \mathbb{R}^N$, $b \in \mathbb{R}^K$, dimension of $A_0 = K \times N$, and $f_i(x)_{i \in (1,\dots,m)} = \langle c_i, x \rangle_{c_i \in \mathbb{R}^N} + d_{i_{d_i \in \mathbb{R}^N}}$

Given that x which satisfies $f_1(x) < 0, \dots, f_m(x) < 0$, $\lambda > 0$, $\mu > 1$, $\varepsilon_{feasible} > 0$, and

$\varepsilon > 0$.

Set $f_{u_1,i} = x_i - u_i$ and $f_{u_2,i} = -x_i - u_i$ with corresponding dual variables $\lambda_{u_1,i}, \lambda_{u_2,i}$.

Repeat

1. Determine t. Set $t = \mu m / \hat{\eta}$.

2. Calculate primal-dual search direction $\Delta y_{primal-dual}$.

3. Line search and update.

    A. Determine step length $s > 0$.

    B. Set $y = y + s \Delta y_{primal-dual}$.

Until $\|r_{primal}\|_2 \leq \varepsilon_{feasible}$, $\|r_{dual}\|_2 \leq \varepsilon_{feasible}$, and $\hat{\eta} \leq \varepsilon$. This is excerpted from l1-magic notes (Candes and Romberg 2005).

APPENDIX C

CITY NAMES USED IN THE TREND ANALYSIS

| No. | City | State | No. | City | State |
|---|---|---|---|---|---|
| 1* | Davis MAFB | AZ | 31* | Bicycle Lake | CA |
| 2* | Deer Valley | AZ | 32 | Big Bear Apt | CA |
| 3* | Douglas | AZ | 33 | Bishop | CA |
| 4* | Falcon Fld | AZ | 34 | Blue Canyon | CA |
| 5 | Flagstaff | AZ | 35 | Blythe | CA |
| 6* | Fort Huachuca | AZ | 36 | Burbank | CA |
| 7* | Gila Bend | AZ | 37* | Camp Pendleton | CA |
| 8* | Good year | AZ | 38 | Campo | CA |
| 9 | Grand Canyon | AZ | 39 | Carlsbad | CA |
| 10 | Kingman | AZ | 40* | Castle AFB | CA |
| 11* | Luke | AZ | 41 | Chico | CA |
| 12 | Page | AZ | 42* | China Lake | CA |
| 13* | Payson | AZ | 43 | Chino | CA |
| 14* | Phoenix | AZ | 44* | Chowchilla | CA |
| 15 | Prescott | AZ | 45* | Coalinga | CA |
| 16* | Safford Awrs | AZ | 46* | Concord | CA |
| 17* | Scottsdale | AZ | 47* | Daggett | CA |
| 18 | ShowLow | AZ | 48* | Edwards AFB | CA |
| 19 | ShowLow a | AZ | 49 | El Centro | CA |
| 20* | Tucson | AZ | 50* | El Monte | CA |
| 21* | Williams AFB | AZ | 51 | El Toro | CA |
| 22* | Winslow | AZ | 52 | Fort Hunter | CA |
| 23 | Yuma | AZ | 53 | Fort Ord | CA |
| 24* | Yuma Mcas | AZ | 54* | Fowler | CA |
| 25 | Yuma Proving Ground | AZ | 55 | Fresno | CA |
| 26 | Alameda NAS | CA | 56* | Fresno | CA |
| 27 | Alturas | CA | 57* | Fullerton | CA |
| 28 | Bakersfield | CA | 58* | George AFB | CA |
| 29* | Beale AFB | CA | 59* | Hawthorne | CA |
| 30* | Beaumont | CA | 60 | Hayward | CA |

Letter in red and asterisk (*) next to number indicates the selected city.

| No. | City | State | No. | City | State |
|---|---|---|---|---|---|
| 61* | Huron | CA | 91 | Palm Springs | CA |
| 62 | Imperial | CA | 92* | Palmdale | CA |
| 63 | Imperial Beach | CA | 93 | Palo Alto | CA |
| 64* | Kerman | CA | 94 | Paso Robles | CA |
| 65 | La Verne | CA | 95 | Point Mugu | CA |
| 66* | Lake Tahoe | CA | 96 | Pt Arguello | CA |
| 67* | Lancaster | CA | 97 | Pt Piedras | CA |
| 68* | Lemoore NAS | CA | 98 | Pt Piedras a | CA |

| No. | City | State | No. | City | State |
|---|---|---|---|---|---|
| 69 | Livermore | CA | 99 | RedBluff | CA |
| 70 | Los Angeles | CA | 100 | Redding | CA |
| 71* | Los Banos | CA | 101* | Sacramento | CA |
| 72* | Mammoth Lakes | CA | 102* | Sacramento a | CA |
| 73 | March AFB | CA | 103 | Salinas | CA |
| 74 | Marysville | CA | 104 | San Carlos | CA |
| 75 | Mcclellan | CA | 105* | San Clemente | CA |
| 76* | Merced | CA | 106* | San Diego | CA |
| 77 | Miramar NAS | CA | 107* | San Diego a | CA |
| 78 | Modesto | CA | 108 | San Francisco | CA |
| 79 | Moffet NAS | CA | 109 | San Jose | CA |
| 80* | Mojave | CA | 110 | San Jose Rei | CA |
| 81 | Monterey | CA | 111 | San Luis Obispo | CA |
| 82 | Mount Shasta | CA | 112* | San Mateo | CA |
| 83 | Mount Wilson | CA | 113 | San Miguel | CA |
| 84* | Napa | CA | 114 | San Nicholas | CA |
| 85 | Needles | CA | 115 | Sandburg | CA |
| 86 | North Island | CA | 116 | Santa Ana | CA |
| 87* | Norton AFB | CA | 117* | Santa Barbara | CA |
| 88 | Oakland | CA | 118* | Santa Maria | CA |
| 89 | Ontario Int. Airport | CA | 119 | Santa Monica | CA |
| 90* | Oxnard | CA | 120 | Siskiyou | CA |

Letter in red and asterisk (*) next to number indicates the selected city.

| No. | City | State | No. | City | State |
|---|---|---|---|---|---|
| 121* | Stockton | CA | 150* | Saint George | UT |
| 122 | Superior Val | CA | 151* | Salt Lake City | UT |
| 123 | Susanville | CA | 152* | Tooele | UT |
| 124 | Thermal | CA | 153* | Beryl | UT |
| 125 | Torrance | CA | 154 | Wendover | UT |
| 126* | Travis AFB | CA | 155* | Austin | NV |
| 127 | TruckeeTahoe | CA | 156* | Austin a | NV |
| 128* | Turlock | CA | 157* | Battle Mtn | NV |
| 129* | Tustin Mcas | CA | 158* | Caliente | NV |
| 130* | Twentynine Palm | CA | 159 | Elko | NV |
| 131 | Van Nuys | CA | 160* | Ely Yelland | NV |
| 132 | Vandenberg | CA | 161* | Eureka | CA |
| 133 | Visalia | CA | 162* | Fallon NAS | NV |
| 134 | Blanding | UT | 163* | Hawthorne | CA |
| 135 | Bullfrog Mar | UT | 164* | Indian Spring Rn | NV |
| 136* | Cedar City | UT | 165* | Indian Spring Rn a | NV |
| 137* | Delta | UT | 166* | Las Vegas | NV |

| | | | | | | |
|---|---|---|---|---|---|---|
| 138 | Dugway Proving Ground | UT | | 167 | Lovelock | NV |
| 139 | Eagle Range | UT | | 168* | Mercury | NV |
| 140 | Green River | UT | | 169* | Nellis AFB | NV |
| 141* | Hanksville | UT | | 170* | Reno | NV |
| 142* | Hill AFB | UT | | 171 | Tonopah | NV |
| 143* | Logan | UT | | 172 | Wildhorse | NV |
| 144 | Milford | UT | | 173* | Winnemucca | NV |
| 145 | Moab | UT | | 174 | Yucca Flat | NV |
| 146* | Ogden | UT | | | | |
| 147 | Price Carbon | UT | | | | |
| 148* | Provo | UT | | | | |
| 149 | Roosevelt | UT | | | | |

Letter in red and asterisk (*) next to number indicates the selected city.

BIOGRAPHICAL SKETCH

Joon Young Lee (June) got a Ph.D degree in mechanical engineering and his M.S.E degree in industrial engineering from Arizona State University. He graduated from Yonsei University with M.S. and B.S degrees in computer and industrial engineering and industrial system engineering. He is a member of ASME, SPIE, INFORMS, Tau Beta Pi and Phi Kappa Phi. Over the course of his studies at ASU, he taught undergraduate mechanical engineering classes and has given occasional lectures and helped to develop lectures, experimental demonstrations, and presentations. June has been involved in a number of research projects. He has been working on research in the area of optimization and engineering methods for complex thermal-fluid processes. His long-term research interests in optimization and engineering methods provide a strong foundation on which to bring up multi-disciplinary research in mechanical and industrial engineering. He seeks an academic/industrial position where he can work with highly motivated individuals in a diverse environment that focuses on preparing for challenges in engineering and positive impacts on society. He hopes to share his passion with engineering students, providing them with not only skills and knowledge but also a desire to learn.